Measuring and modelling of the wind on the scale of tall wind turbines

Floors, Rogier Ralph

Publication date:
2013

Document Version
Publisher's PDF, also known as Version of record

Measuring and modelling of the wind on the scale of tall wind turbines

Rogier Floors
DTU Wind Energy PhD-0034(EN)
November 2013

DTU Wind Energy
Department of Wind Energy

Author: Rogier Floors
Title: Measuring and modelling of the wind on the scale of tall wind turbines
Division: Department of Wind Energy

DTU PhD-0034(EN)
September 2013

Abstract:

The air flow in the lower atmosphere on the spatial scale of the modern wind turbines is studied. Because wind turbines are nowadays often taller than 100 m, the validity of current analytical and numerical atmospheric models has to be evaluated and more knowledge about the structure of the atmospheric boundary layer at those heights has to be acquired. A new long-range wind lidar was placed next to well-instrumented meteorological masts in the west of Denmark and in northern Germany and measured the wind speed and direction up to 2000 m and was compared with wind-speed measurements from the meteorological masts.

The Høvsøre site is characterized by a transition from the flow over sea, which has a low surface roughness, to flow over land, which has a much higher surface roughness. The internal boundary layer that forms after this transition, was characterized by both the upstream and the downstream stability. Modelling the mean climatological wind speed with a 3-layer interpolation scheme gave good results, both in neutral conditions and when including other stability conditions. The constants in the model were slightly adjusted based on comparison with other studies and a numerical model.

A mesoscale numerical model was used to simulate the flow at Høvsøre for four weeks during autumn 2010. The wind profile did not have enough vertical shear in the lower part of the PBL and had a negative bias higher up in the boundary layer. In the grid points after the shoreline the wind speed near the surface and the friction velocity had a bias, which were related to the change in surface roughness. A higher-order boundary-layer scheme represented the wind profile of the westerly flow over sea better, while a first-order scheme modelled the flow from the east with low-level jets better. The wind profile shape and the negative wind speed bias at larger heights were not improved when a different synoptic forcing and a different vertical resolution were used in the model.

The effect of baroclinity was explored for the two sites. The surface geostrophic wind, the gradient wind and the thermal wind were derived from simulations with a mesoscale model. In both locations the thermal wind up to 970 m was approximately Gaussianly distributed with a standard deviation of three m s^{-1} and the thermal wind vector varied seasonally due to temperature differences between sea and land. The wind veer was particularly sensitive to baroclinity. The variation of the resistance law constants in neutral, baroclinic conditions was approximately the same as in experiments that where assumed to be barotropic; part of the variation was explained by baroclinity showing the importance of including this effect when studying boundary-layer winds.

The thesis is submitted to the Danish Technical University in partial fulfillment of the requirements for the PhD degree.

ISBN 978-87-92896-76-6

Sponsorship:
Danish Research Agency
Strategic Research Council
(Sagsnr. 2104-08-0025)
"Tall wind" project

Pages: 110
References: 120
Figures: 31
Tables: 10

Wind Energy Department
Technical University of Denmark
P.O.Box 49
DK-4000 Roskilde
Denmark
Telephone +45 46774005
bibl@dtu.dk
Fax +45 46774013
www.dtu.dk

CONTENTS

Acknowledgements 8

1 Introduction 9

2 Theory 12
2.1 The planetary boundary layer 12
2.1.1 The flow in the PBL 12
2.1.2 Turbulent momentum flux 13
2.1.3 Geostrophic wind 14
2.1.4 Buoyancy 14
2.2 The surface layer 15
2.3 Mesoscale modelling 16

3 Measurements and data processing. 18
3.1 Wind lidar 18
3.2 Meteorological mast 19

4 Comparison of the instruments 22

5 Analysis of diabatic flow modification in the internal boundary layer . . 26
5.1 Abstract 26
5.2 Introduction 26
5.3 Theory 27
5.3.1 Internal boundary layer 27
5.3.2 Wind profile 29
5.4 Methodology 31
5.4.1 Horns Rev 31
5.4.2 Høvsøre 33
5.5 Results 35
5.5.1 Stability analysis 35
5.5.2 Wind profiles 35
5.5.3 Heat and momentum flux profiles 37
5.5.4 Modelling the wind profile in the IBL 38
5.6 Discussion 42

5.7 Conclusion . . . 42

6 The wind profile in the coastal boundary layer . . . 44
6.1 Introduction . . . 44
6.2 Theory . . . 46
6.2.1 Parametrizations in the WRF model . . . 46
6.2.2 Mesoscale modelling of the PBL . . . 49
6.3 Methodology . . . 50
6.3.1 Measurements . . . 50
6.3.2 Model simulations . . . 54
6.4 Results . . . 55
6.4.1 Synoptic overview . . . 55
6.4.2 Wind profiles and surface-layer fluxes . . . 56
6.4.3 Internal boundary layer . . . 61
6.4.4 Stability . . . 63
6.4.5 Forcing . . . 64
6.5 Discussion . . . 66
6.6 Summary and Conclusions . . . 67

7 The effect of baroclinicity on the wind in the planetary boundary layer . 69
7.1 Introduction . . . 69
7.2 Theory . . . 71
7.3 Methodology . . . 73
7.3.1 Measurements . . . 73
7.3.2 Estimation of the atmospheric forcing . . . 78
7.4 Results . . . 80
7.4.1 A climatology of baroclinicity . . . 80
7.4.2 Estimations of the geostrophic wind . . . 83
7.4.3 Integral PBL measures . . . 85
7.5 Conclusions . . . 89

8 Summary and outlook . . . 92
8.1 Summary . . . 92
8.2 Outlook and future perspectives . . . 93
8.3 Implications for wind energy . . . 96

Dissemination . . . 97

Appendices . . .

A Despiking of the sonic anemometer data . . . 100

B Bug in YSU PBL scheme 102

C Derivation of the geostrophic drag law 103

Bibliography 105

DANSK RESUMÉ

I denne rapport undersøges luftstrømmen i den nederste del af atmosfæren – op til højder i størrelsesordnen af moderne vindmøller. Fordi vindmøller i dag ofte er højere end 100 m, undersøges gyldigheden af nuværende analytiske og numeriske atmosfæriske modeller med henblok på at erhevrve mere viden om strukturen af det atmosfæriske grænselag. En ny langtrækkende vind-LIDAR placeret nær instrumenterede meteorologiske master i det vestlige Danmark og i Nordtyskland målte vind-hastighed og -retning i højder op til 2000 m, og disse målinger sammenlignes med vindhastighedsmålinger fra meteorologiske master.

Placeringen ved Høvsøre er kendetegnet ved at være tæt på havet, som har en lav overfladeruhed, og landjorden, som har en meget højere overfladeruhed. Det interne grænselag, der dannes efter ved overgangen fra hav til land, påvirkes af både opstrøms og nedstrøms atmosfærisk stabilitet. Modellering af den klimatologiske vindhastighed ved hjælp af en 3-lags interpolation gav gode resultater, både under neutrale forhold og under andre stabilitetsforhold. Konstanterne i modellen blev ændret baseret på sammenligning med andre studier og en numerisk model.

En numerisk mesoskala model blev brugt til at simulere vinden ved Høvsøre i fire uger i løbet af efteråret 2010. Den vertikale gradient af vindprofilen i den nederste del af grænselaget var for lav, og vindhastighed var generelt for lav højere oppe i grænselaget. Vindhastigheden nær overfladen samt friktionshastigheden havde umiddelbart efter kystlinjen en forskel der kan relateret til ændringen i overfladeruhed. Et højereordens grænselagsskema gav bedre resultater med hensyn til vindprofilen, når vinden kom fra vest over havet, mens et første-ordens grænselagsskema gav bedre resultater når vinden var fra øst med dannelse af ”low-level jets”. Vindprofilens form og den generelle underestimering af vindhastigheden i større højder blev ikke forbedret ved brug af en anden synoptisk forcing og en højere vertikal opløsning i modellen.

Effekten af den horizontale temperaturgradient (baroklinicitet) blev undersøgt for de to lokaliteter. Den geostrofiske vind ved overfladen, gradient-vinden og den termiske vind blev beregnet ved hjælp af simuleringer med en mesoskala model. Ved begge lokaliteter var den termiske vind op til 970 m's højde tilnærmelsesvis Gaussisk fordelt med en standardafvigelse på tre m s^{-1} og den termiske vind-vektor varierede sæsonmæssigt grundet temperaturforskelle mellem hav og land. Vindretningens ændring med højden viste sig at være meget følsom over for baroklinicitet. Variationen af værdien af konstanterne i den geostrofiske "draglaw" under neutrale og barokline forhold var næsten den samme som i undersøgelser hvor det var antaget at forholdene var barotrope;

en del af variationen kan forklares ved at forholdene rent faktisk ikke var barotrope men barokline, hvilket viser vigtigheden af at inddrage denne effekt i studier af vinden i det atmosfæriske grænselag.

ACKNOWLEDGEMENTS

Staying in Denmark for the last three years has been a great experience, both personally and professionally. I would like to thank my former office mates Nikola and Jesper for sharing the office during the start of my PhD and in particular my most long-lasting office mate Patrick who helped me to not forget my Dutch and with whom I had many interesting discussions. There is a great group of friends that I met during these three years: thanks to Carlo, Fabrizio, Juan and Leonardo for all our great hiking and climbing trips, thanks to Philipp for providing me with a wake on the biking commute and thanks to Mari, Cristian, Thijs, Federica, Paul and Maria for the good times I was able spend with you. Particularly I thank my family for their support and the freedom you gave me to leave the Netherlands.

Alfredo has been a great help throughout my PhD. The manuscripts marked with red ink were first a nightmare for me, but in the end turned out to be very helpful and you always provided me with new ideas. Also Ekaterina and Claire and all other members of the meteorology department have been helpful in many ways.

Most of all I would like to thank Sven-Erik: your vast knowledge about meteorology and your ability to sketch the broad outlines for my whole project were very helpful. I also greatly appreciate that I was able to visit the University Centre of Svalbard and the Finnish Meteorological Institute and I am grateful to all people that I met there, but in particular to Marina and Irene.

1

INTRODUCTION

The importance of the wind in our daily lives can be appreciated when we feel its force on man-made structures during a storm, drive against it on a bike or use it to generate energy with wind turbines. But predicting the wind at any height in the planetary boundary layer (PBL) is challenging, because the wind is notoriously unpredictable due to turbulence and its poorly understood interactions with other components in the earth's system.

The last few years an increasing amount of energy worldwide is generated by wind turbines. Newly built turbines have blades that reach up to nearly 200 m height and thus are exposed to a wide range of atmospheric scales. The cover figure of this thesis shows the large amount of scales relevant for describing the atmospheric flow for a wind turbine, ranging from leaves of grass of a few centimeters to the large-scale flow related to high- and low pressure systems. Therefore, detailed knowledge of the behaviour of the flow at all these scales is required for the planning of wind farms and accurate predictions of the wind speed.

Because the equations describing the turbulent flow cannot be solved analytically, a significant part of the understanding of the PBL is based on physical theories, field experiments and since the rise of computers also numerical modelling. The Monin-Obukhov similarity theory (MOST) and the description of the flux-profile relationships in the Kansas experiment is such an example of combining theory and observations (Businger et al., 1971). As a result of these advances, the stability-corrected logarithmic wind profile has been successfully used to describe the wind profile in the surface layer for wind energy applications (Troen and Petersen, 1989). However, the logarithmic wind profile is only valid in the surface layer, so new improvements to describe the change of wind with height are required (Gryning et al., 2007a; Peña et al., 2009a).

Also numerical modelling of the wind in the PBL has seen many improvements over the last decades, partially because of the increase in computing power. For example, mesoscale numerical weather prediction (NWP) models in which boundary-layer turbulence is parameterized are able to realistically predict many features of the PBL (Shin and Hong, 2011; Steeneveld et al., 2011). These PBL parameterizations are nowadays used for horizontal grid sizes that approach the size of the PBL but do not resolve turbulence (Wyngaard, 2004; Gibbs et al., 2011). Still, mesoscale models are increasingly used for downscaling wind information from global weather prediction models to finer scales.

A problem for improving the models, is that there are few measurements available

for validation higher up in the PBL. Therefore, verification studies are often focused on the representation of standard near-surface variables like 2 m temperature or 10 m wind speed. Despite the progress in atmospheric measuring techniques, even today it is still a challenge to measure the wind up to several hundreds of meters height. The usage of meteorological masts equipped with cup and sonic anemometers to measure the atmospheric flow is common below 100 m, but taller meteorological masts are rare because they are expensive and cumbersome to construct and maintain.

Luckily the wind lidar industry has gone through a series of rapid technological developments last years, helped by the improvements of fiber optics in the phone and internet industry. A wind lidar is an active remote sensing instrument that responds to the atmospheric backscatter from an emitted laser pulse by naturally occurring aerosols to reconstruct the line of sight wind speed at a given height. Wind lidars can be used to measure the wind speed in the whole PBL with a high precision on a continuous basis at relatively low costs. Peña (2009) used wind lidars to study the wind profile up to 300 m, but the long-range wind lidars can now measure up to 2000 m and cover therefore most of the PBL.

This thesis aims to utilize this improved measuring technique and combine it with traditional mast measurements, to identify which models can be used and which physical processes have to be understood to predict the wind at the scales of modern wind turbines. For this, wind speed and turbulence measurements from a mast at a site near the coast of western Denmark (Høvsøre), a mast offshore at the west coast of Denmark (Horns Rev) and a mast in northern Germany (Hamburg) will be used. These measurements will be complemented with the wind measurements from a long-range wind lidar that was operating for one year next to the masts at Høvsøre and Hamburg.

The first chapter of this thesis is the introduction, which provides a basic background to understand the results. A general overview of the physical processes that play a role in the PBL is given and the theory on which the analytical and numerical models are based is presented (Chapter 2). Then, the operation of the sonic anemometers, cup anemometers and the wind lidar is described in Chapter 3. Some results from a intercomparison between the instruments are presented in Chapter 4, to evaluate the accuracy of the wind lidar against the cup and sonic anemometers.

The results section of this thesis consists of the three papers, which are enclosed as three independent chapters. In Chapter 5 an analytical model of the flow after a smooth-to-rough surface roughness change from sea to land is validated using measurements from the 160 m high meteorological mast at Høvsøre. The site is located 2 km from shoreline and therefore well suited to explore the effects of the internal boundary layer (IBL) on the logarithmic wind profile at larger scales. Furthermore, the effect of local and upstream stability on the structure of the IBL will be analyzed.

In Chapter 6 a mesoscale model is used to simulate the flow at Høvsøre for a 4 week period. The sensitivity to surface roughness change, the choice of the PBL scheme, the vertical model resolution and the forcing are analyzed. This is done for both the easterly

and the westerly sector, to assess the difference between marine and rural upstream conditions.

In Chapter 7 we study the effect of baroclinity on the relation between geostrophic wind and the wind near the surface. Baroclinity is one of the large scale parameters that is poorly studied, because measurements of horizontal temperature gradients are scarce. Therefore mesoscale model output is used to obtain large-scale pressure and temperature gradients and estimate the effect of these parameters on the measured wind profile up to 950 m. The effect of baroclinity on the resistance law constants in the neutral PBL is analyzed.

In Chapter 8 a summary of the results from this thesis is provided. Also the implications for the wind energy industry are discussed and some ideas for future research are given.

2

THEORY

Atmospheric flow can be described by the Navier-Stokes equations, but because of its large Reynolds number the flow is generally turbulent and therefore statistical methods are used to describe the flow. The Reynolds-averaged Navier-Stokes equations are such a statistical approach to describe mean properties of the turbulent flow and are introduced in section 2.1. The surface-layer is an important part of the PBL where special laws can be applied which will be discussed in Section 2.2. In Section 2.3 the set of equations that is numerically solved to describe the atmospheric flow with a mesoscale model is briefly discussed.

2.1 The planetary boundary layer

The PBL is the layer of the atmosphere that is directly influenced by interaction with the earth's surface. By definition the PBL is characterized by continuous turbulence, which is responsible for the transport of heat, moisture and momentum. The Reynolds-averaged Navier-Stokes equations are presented in 2.1.1 and in the following sections the different terms of these equations are discussed. Section 2.1.3 describes the Coriolis force and the pressure-gradient force, which together determine the flow above the PBL. In Section 2.1.2 we discuss the role of the turbulent momentum flux and in Section 2.1.4 we discuss the influence of the buoyancy term.

2.1.1 The flow in the PBL

To help to describe turbulence it is common to use Reynolds decomposition. On a regular x,y,z grid the atmospheric flow can then be split in a mean U,V,W and a turbulent part u',v',w'. In the PBL, the molecular diffusion can be neglected except very near the surface and therefore the mean momentum equations can be written, using the Einstein summation notation, as,

$$\frac{\partial U_i}{\partial t} + U_j \frac{\partial U_i}{\partial x_j} = \underbrace{-\frac{\partial}{\partial x_j}\overline{u_i' u_j'}}_{\text{A}} \underbrace{-\frac{1}{\rho}\frac{\partial P}{\partial x_i}}_{\text{B}} \underbrace{-2\varepsilon_{ijk}\Omega_j U_k}_{\text{C}} + \underbrace{\frac{g}{T_0}\Theta_v \delta_{3i}}_{\text{D}} \tag{2.1}$$

where ρ_0 is the background air density, P is the atmospheric pressure, ε is the Levi-Civita symbol, Ω is the angular speed of the rotation of the earth, g/T_0 is the buoyancy

parameter, Θ is the mean potential temperature deviation from its background state and the horizontal bar denotes an average. Throughout this thesis the subscript v denotes a virtual heat flux or temperature. The virtual potential temperature is defined as $\theta_v = \theta(1+0.61q)$, where θ is the potential temperature and q the specific humidity. The virtual temperature represents the temperature of dry air having the same pressure and density as moist air with temperature θ. The left hand side of Eq. 2.1 expresses the effect of local and advective accelerations in the atmosphere and terms A–D will be discussed in the following sections.

Eq. 2.1 has no exact solution and therefore many atmospheric scientists use a conceptual view of turbulence in the PBL. One of the views that will be used throughout this thesis, is to think of turbulence as chaotically moving eddies of different sizes that interact with each other. The largest eddies extract energy from the mean flow and break up into smaller eddies. The transfer of kinetic energy to smaller and smaller scales continues until the eddies break up into a size approaching the Kolmogorov scale ($\sim$ 1 mm) and then the eddies are dissipated to heat by molecular viscocity.

2.1.2 Turbulent momentum flux

In Eq. 2.1, term A represents the divergence of the turbulent momentum fluxes (also called Reynolds stresses). It appears because of the Reynolds averaging and it expresses the effect of turbulence on the mean flow. Because the molecular diffusivity is very small compared to the effect of turbulent mixing, the relevant velocity scale in the PBL is the friction velocity, $u_* \equiv \sqrt{\tau/\rho} = (\overline{u'w'}^2 + \overline{v'w'}^2)^{1/4}$. There are more unknowns than equations in Reynolds-averaged flow and so higher moments have to be expressed in terms of lower ones, a so-called closure assumption.

A popular closure assumption is the first-order closure, which expresses the turbulent momentum flux by diagnostically prescribing the eddy diffusivity for momentum, K_m. This eddy diffusivity can be thought of as analogue to molecular diffusivity but instead it is carried by the turbulent eddies. A first-order closure is often used in large-scale weather models because of its low computational costs. K_m can for example be described using the mixing-length concept (Prandtl, 1925). It expresses K_m as the function of a length scale l and the mean wind speed gradient,

$$K_m = l^2 \frac{\mathrm{d}U_z}{\mathrm{d}z}, \tag{2.2}$$

where $U_z = \sqrt{U^2+V^2}$ on a height z. The mixing-length can be interpreted as the distance which an eddy has to move up or down before it is mixed with its environment. Another popular closure assumption is the 1.5-order closure, which assumes that K_m can be found by using the prognostic turbulent kinetic energy equation and a certain length scale l. Both the first-order and 1.5-order closure are further discussed in Section 6.2.1.

2.1.3 Geostrophic wind

Above the PBL height (h) there is generally no turbulence and therefore a balance exists between the pressure gradient force (Eq. 2.1, term B) and the Coriolis force (Eq. 2.1, term C) only. The flow is in so-called geostrophic balance and is parallel to the isobars. Assuming horizontally homogeneous, stationairy, neutral flow where the mean vertical velocity is zero, Eq. 2.1 can be simplified to,

$$\frac{\partial}{\partial z}\overline{u'w'} = f(V - V_g), \tag{2.3}$$

$$\frac{\partial}{\partial z}\overline{v'w'} = f(U_g - U), \tag{2.4}$$

where $U_g = -(1/f\rho_0)\partial P/\partial x$ and $V_g = (1/f\rho_0)\partial P/\partial y$ are the geostrophic wind speed components and $f = 2\Omega\sin\phi$ is the Coriolis parameter for a certain latitude ϕ. The geostrophic wind can vary with height when the pressure gradients vary with height. This happens when there are horizontal density differences in the atmosphere that cause baroclinity. This is further discussed in Chapter 7.

From Eqs. 2.3 and 2.4 one can obtain the geostrophic drag law by using dimensional analysis and similarity theory (Blackadar and Tennekes, 1968). The derivation of the geostrophic drag law is given in Appendix C. Although similarity theory can be very useful in the PBL, the geostrophic drag law proved to be difficult to verify experimentally because many parameters vary simultaneously when measuring in the PBL (Hess and Garratt, 2002a). Therefore, some of the processes that are important for the geostrophic drag law can most easily be studied by doing idealized large-eddy simulations (Zilitinkevich and Esau, 2005).

2.1.4 Buoyancy

The buoyancy term (Eq. 2.1 term D) is important in boundary-layer meteorology, since it completely changes the structure of the PBL. When the potential temperature is increasing with height, the buoyancy term is negative. Therefore, the movement of an eddy that has a certain positive vertical velocity is damped by the buoyancy force. It will have the tendency to stay close to its original vertical position and therefore this atmospheric state is known as stably stratified. When the vertical potential temperature gradient is negative, an eddy that moves upward will end up in an environment where it is warmer then its environment and so its motion is amplified by the buoyancy force. Finally, there is the neutrally stratified PBL, which has low deviations of potential temperature and therefore the turbulence is mainly generated by vertical wind shear.

The stratification of the PBL over land is primarily determined by the energy balance of the surface, while over sea it is mainly determined by the temperature differences between the sea water and the air masses that are advected over it. During the morning

of a sunny day over land, the energy balance becomes positive because there is more short-wave radiation coming in than long-wave radiation is going out. This surplus of energy is then transmitted to the atmosphere through turbulent mixing or by conduction into the soil. During night, the situation is the opposite and the surface extracts energy from the atmosphere and is warmed from below from deeper soil layers. The contrast between stratification over land and over sea and the impact of stratification on the wind profile are further discussed in Chapter 5.

The stable boundary layer is shallow (∼50–500 m) because turbulence is suppressed by the negative buoyancy effects. Stable boundary layer are often classified into weakly stable and very stable: in weakly stable conditions there is still continuous mechanical production of turbulence due to a stronger wind, but in a strongly stable boundary layer the conditions are calm and turbulence can be intermittent (Mahrt, 1999). Low-level jets can form in the layer above the stable boundary layer that was well-mixed during the daytime. There the flow accelerates because the vertical turbulent flux divergence decreases (Eq. 7.1 and 7.2) and the wind vector starts to oscillate around the geostrophic wind vector (Blackadar, 1957). Low-level jets can be very important for wind-energy applications and can have super-geostrophic wind speeds (Storm et al., 2009).

The unstable boundary layer is much deeper compared to the stable boundary layer (∼1000–3000 m). The eddy diffusivity in the unstable PBL is high and the mean velocity gradients in the middle of the unstable PBL are usually small. Because the unstable boundary layer is capped by an inversion layer, it can entrain air with a higher potential temperature from the free atmosphere in the entrainment zone. Because the turbulent eddies cause the instantaneous PBL height to vary substantially, the entrainment zone measured over a longer time interval can be several ten to hundreds of meters thick. In the entrainment zone the potential temperature increases strongly with height and the wind speed components relax to their geostrophic values.

2.2 The surface layer

In the surface layer, approximately the lower 10% of the PBL, MOST has helped to structure the description of turbulence and the wind profile. Obukhov (1971) used the assumption that under stationary, homogeneous conditions, the friction velocity, the heat flux, the buoyancy parameter and the height above the surface govern the flow in the surface layer and derived a length scale, which now carries his name. MOST states that under the assumptions of stationarity and homogeneity dimensionless groups of mean vertical gradients and turbulent statistics in the surface-layer are a function of the stability parameter z/L, where L is the Obukhov length,

$$L = -\frac{{u_{*0}}^3}{\kappa(g/T_0)\overline{w'\Theta'_v}_0}, \tag{2.5}$$

where κ is the von Kármán constant, $\overline{w'\theta'_{v0}}$ is the virtual kinematic heat-flux and the subscripts 0 denotes a surface-layer value. In the surface layer the effect of the Coriolis force can be neglected and therefore the wind does not turn with height. The mixing-length concept from Prandtl (1925) can again be used to predict the change of U_z with height,

$$u_* = l\frac{\mathrm{d}U_z}{\mathrm{d}z}. \tag{2.6}$$

When it is assumed that the mixing-length in the surface layer is limited by the distance to the surface, we can substitute $l = z$. In addition it is a convention to use κ to scale this expression in near-surface turbulence, which value is debated but ≈ 0.4 (Högström, 1988). The result is an expression for the dimensionless wind shear which should according to MOST be a universal function of z/L,

$$\frac{\kappa z}{u_*}\frac{\mathrm{d}U_z}{\mathrm{d}z} = \phi_m\left(\frac{z}{L}\right) \tag{2.7}$$

Integrating Eq. 2.7 from the characteristic height of the surface elements, the so-called roughness length z_0, to z gives the logarithmic wind profile,

$$U_z = \frac{u_{*0}}{\kappa}\left[\ln\left(\frac{z}{z_0}\right) - \psi_m\left(\frac{z}{L}\right)\right], \tag{2.8}$$

ψ_m is the diabatic correction to the wind profile and is the integrated form of the experimental function ϕ_m. In stable conditions ϕ_m is approximately linear and is easily integrated, but for unstable conditions some more complicated forms have been proposed (Paulson, 1970).

2.3 Mesoscale modelling

Mesoscale models are extensively used to simulate the atmospheric flow on horizontal scales of ∼1–10 km (Shin and Hong, 2011; Gibbs et al., 2011; Steeneveld et al., 2011). Also in the wind energy industry they are frequently employed, for example for the production of wind atlases, which describe the climatological wind conditions over a large area, such as Finland (Tammelin et al., 2013).

A mesoscale model numerically integrates Eq. 2.1 forward in time together with expressions for the conservation of mass and moisture, the first law of thermodynamics and the equation of state. Because of the chaotic behaviour of the atmosphere small errors in the initial conditions can quickly grow into very different large-scale atmospheric scenarios. Consequently correct initial conditions and boundary conditions are essential for a mesoscale model and usually they are provided by the output from large-scale NWP models, such as the Global Forecast System (GFS) from the National Oceanic and Atmospheric Administration (NOAA) and the model from the European Centre of Medium

Range Weather forecasting (ECMWF) or by numerical re-analysis of large amounts of observational data from the past.

When mesoscale models are used for hind casts for a longer period of time ($\sim$10 days) it is important that the model does not drift from the large-scale representation of the flow. Therefore a technique is often employed to nudge some atmospheric variables with a relaxation term towards the large-scale data. The mesoscale model is used with this option in the long-term simulations in Chapter 7 and in Gryning et al. (2013b). It was shown that this approach better represents the Weibull-distribution of wind speeds when compared with observations (Gryning et al., 2013a).

Because it is often numerically too expensive to run a mesoscale model on a horizontal grid size finer than $\sim$ 1 km and because a mesoscale model does not resolve turbulence, many processes that occur at smaller scales are parametrized in different schemes. In Chapter 6 and 7 the Advanced Research WRF model (hereafter the WRF model) is used, which is a mesoscale model with a variety of physical parametrizations that is designed for research and operational applications. The most relevant parametrization schemes from a wind energy perspective are the PBL scheme, the surface-layer scheme and the land-surface scheme. They all have a large impact on the shape of the wind profile in the PBL (Zhang and Zheng, 2004; Shin and Hong, 2011; Xie et al., 2012). The land-surface scheme is responsible for partitioning the incoming radiation into sensible and latent heat fluxes and representing other physical processes that occur at the surface, such as snow melting, run off and the ground heat flux (Chen and Dudhia, 2001).

The PBL scheme parameterizes the vertical component of term A in Eq. 2.1. As previously discussed there are several closure assumptions and a first-order and 1.5-order closure are implemented in the WRF model, the Yonsei University scheme (YSU) and the Mellor-Yamada Nakanishi Niino (MYNN) scheme (Section 6.2.1), respectively. Finally, the surface-layer scheme is responsible for calculating the exchange coefficients between the land surface and the first model level. Usually a bulk formulation of MOST is used (Section 6.2.1).

3

MEASUREMENTS AND DATA PROCESSING.

A large amount of data from various instruments was available from three sites: a rural-coastal site in the west of Denmark, an offshore site near the west coast of Denmark and a suburban site in Hamburg. In the next section the data processing of the instruments is discussed and accumulated insights on the behaviour of the instruments are presented.

3.1 Wind lidar

Recently, the development of remote sensing techniques to measure the wind speed in the atmosphere has accelerated because of the interest from the wind energy community. Currently there are mainly continuous wave wind lidars and pulsed wind lidars on the market. Comparisons of both technologies show that the pulsed wind lidar is slightly more accurate and that the agreement between a pulsed lidar mean wind speed with that of a cup anemometer is generally within 0.05 m s^{-1} (Sathe et al., 2011). A long-range pulsed Doppler lidar, the windcube WLS70 from the company Leosphere, is used here.

For this thesis no technical changes were made to the instrument, but for clarity the principle of a pulsed wind lidar is briefly outlined. A comprehensive technical discussion on pulsed lidars is given in Cariou and Boquet (2013). In the WLS70, a pulsed laser delivers cyclic pulses of energy (10 μJ) with a wave length of 1.54 μm. The duration of these pulses determines the vertical resolution of the instrument, whereas the travel time from the laser to the target and back is used to discriminate between so-called range gates at different heights.

The laser signal is backscattered off naturally occurring aerosols that are present in almost any ambient flow. The frequency of the return signal is compared with the original signal to estimate the Doppler shift. The backscatter signal from each range gate from many pulses is fast-Fourier transformed to obtain averaged spectra and the peak of these averaged spectra can be related to the Doppler shift and therefore to the velocity along the line of sight (the so-called radial velocity).

To obtain a three dimensional wind vector from the radial velocities, the laser is reflected by a rotating prism at four different positions separated by 90° around the zenith. The angle between the laser beam and the zenith is 15° and the time to accumulate pulses in each position is approximately eight seconds. For reconstruction of the wind vector, it is assumed that the wind field is spatially homogeneous in the area that is covered by the four beams. In addition, both horizontal and vertical wind shear decrease the signal-to-noise ratio and cause a bias if the shear is non-linear.

Table 3.1: Summary of the periods when the lidars were operating. The azimuthal angle shows the rotation of the device versus the geographical north.

Wind lidar	Period [UTC]	Azimuth angle [°]
Hamburg		
Windcube WLS70 Unit 7	2011-04-04 02:00:00–2011-06-02 09:50:00	0
	2011-11-25 12:50:00–2012-03-24 23:50:00	307
Windcube WLS70 Unit 6	2011-06-14 14:10:00–2011-08-02 23:00:00	356
	2011-08-02 23:00:00–2011-11-24 11:50:00	14
Hovsore		
Windcube WLS70 Unit 7	2010-04-23 20:10:00–2011-04-04 23:50:00	50

An overview of the measuring period of the wind lidars at different locations is given in Table 3.1. The wind lidar unit 7 was sent to Leosphere for reparation, because there were problems with the cooling of the instrument. Until the original unit 7 was repaired, another instrument of the same type (unit 6) was used in Hamburg.

3.2 Meteorological mast

Both at the Høvsøre site and at the Hamburg site there are well instrumented tall masts of 160 and 250 m high, respectively. At Horns Rev a smaller mast of 62 m high is available. We elaborate here only on the data processing, since the details of the sites can be found in the methodology sections of Chapter 5, 6 and 7. The data processing is slightly different for each chapter because of the incremented insights that were gathered during the writing of this thesis. These insights are briefly described below.

To obtain the momentum flux and heat flux, the fluctuating component of some atmospheric variable has to be separated from the mean flow using Reynolds decomposition (Eq. 2.1, term A). This can be achieved by assuming that the horizontal bar in Eq. 2.1 is a time average. The Reynolds stresses can then be found by measuring at a high frequency with a sonic anemometer using the eddy-covariance technique. A sonic anemometer measures the time of flight of sonic pulses between pairs of transducers to reconstruct the velocity components. The sonic temperature can be obtained because the speed of sound is dependent on the temperature (Schotanus et al., 1983). A fluctuating part can be retrieved by linearly detrending the recorded high-frequency time series. It is common to align the coordinate system with the mean flow, because then it is easier to make the data comparable to analytical theories. For this, a coordinate transformation is required. The different approaches available for doing such a rotation are described in detail in Wilczak et al. (2001).

In chapter 5 the measurements were processed by using a double rotation. This double rotation first rotates the coordinate system such that the mean lateral wind speed $\overline{v} = 0$ and then it rotates the newly obtained wind components such that the mean vertical

wind speed $\overline{w} = 0$. This approach is commonly used, but Wilczak et al. (2001) argues that it is preferable to use a planar-fit method.

The planar-fit method uses the assumption that $\overline{w}$ over many sonic anemometer runs is zero, but allows $\overline{w} \neq 0$ for the individual runs. The double rotation method can introduce sampling errors in $\overline{w}$ to show up as errors in the tilt angle which can cause errors in the longitudinal component of the stress. The tilt angle in the planar-fit method is calculated by fitting a plane through all the mean wind components measured in that period. The resulting tilt angles are then used to rotate all individual runs in the direction of the mean streamlines. In this thesis a period of one month is chosen to calculate the rotation matrix. Another important advantage of this method is that it also corrects for a possible tilt-error in the y-z plane, which can give a better estimation of the lateral stress.

Figure 3.1 shows ϕ_m versus z/L processed with the double-rotation method and the planar-fit method. ϕ_m was calculated using the turbulent variables measured at 10 m at Høvsøre and the gradient of the wind speed from cup anemometers at 2 and 10 m. It is common to fit a polynomial in $\ln(z)$ to the wind speeds at several heights (Högström, 1988) to estimate the vertical velocity gradient, but this was not done here because the IBL has a large influence on the wind speeds at larger heights, thereby giving a poor fit to a logarithmic profile (Chapter 5). However, it should be noted that the turbulent variables are not measured within the height interval over which the wind speed gradient was measured and that the wind at 2 m is more sensitive to local effects. The data are binned into z/L classes and the mean and standard deviation in each bin are shown, where bins with less than 20 points have been excluded.

It is seen that in particular for negative z/L the planar-fit method has a lower standard deviation which might suggest that the turbulent variables are better estimated in these conditions. This is consistent with the expected impact of the sampling error in $\overline{w}$, which is largest in unstable conditions. However, it should be noted that Fig. 3.1 is sensitive to self-correlation, since u_* appears on both axes.

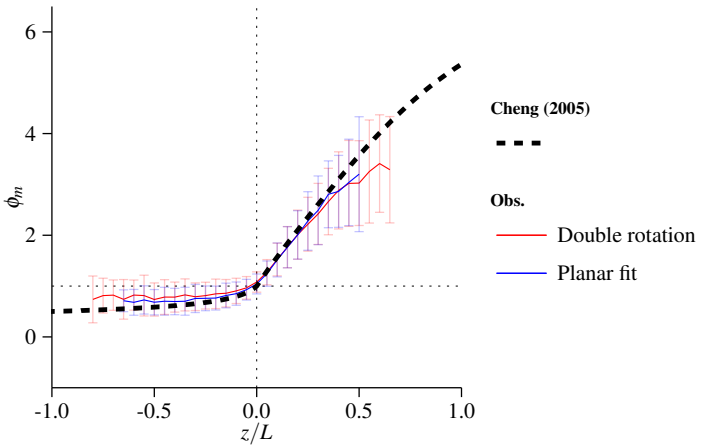

Figure 3.1: Comparison of the dimensionless wind shear versus z/L using the double-rotation method (red line) and the planar-fit method (blue line) using 10-minute mean measurements from April 2010 until April 2011 at Høvsøre. The error bars denote the standard deviation in each bin. Only bins with more than 50 10-minute mean intervals are shown.

4

COMPARISON OF THE INSTRUMENTS

Because the long-range lidar is a novel instrument there is limited experience with estimating the wind speed throughout the PBL. Therefore an extensive validation of its performance compared to cup and sonic anemometers was performed for both Høvsøre and Hamburg. The meteorological mast at Høvsøre has cup- and sonic anemometers mounted at 100 m, which is the same as the height of the first range gate of the wind lidar. Figure 4.1 shows a scatter plot of the ten-minute mean wind speed measured by the cup anemometer compared to that from the wind lidar at 100 m for the whole period that the wind lidar was at Høvsøre (Table 3.1). The observations are separated according to three ranges of the carrier-to-noise (CNR) ratio.

In all three ranges, there is a good agreement between the wind speed from the wind lidar (U_l) and the cup anemometer (U_c). The squared Pearson correlation coefficient $R^2 = (\mathrm{cov}(U_c, U_l)/\sigma_{U_c}\sigma_{U_l})^2$ was 0.88, 0.99 and 1.00 for the three ranges of CNR ratio from low to high, respectively. Thus observations from the wind lidar with a CNR> -22 agree well with those from the cup anemometer. Although emperical, this limit is used in Chapter 6 and 7, in Gryning et al. (2013a,b) and in Peña et al. (2013) to discern good quality and less good quality data.

For the Hamburg site ten-minute mean wind speeds from the wind lidars, unit 6 and unit 7, are shown for the whole period in Hamburg in figure 4.2. Although unit 6 showed on average a slightly worse CNR ratio and consequently more scatter, there was no reason to adjust the threshold value of CNR> -22 as can be seen in Fig. 4.2. Generally there is slightly more scatter between the sonic anemometer and the wind lidar compared to Høvsøre. This is related to the following aspects:

- The wind lidar was placed ~ 170 m to the north-east of a TV tower, so there can be spatial differences in the flow.
- The TV-tower in Hamburg is several meters wide and can therefore cause flow distortion.

During the measurement campaign at Høvsøre it was observed that the lidar wind speed at 250 m was sometimes several meters per second lower than expected from interpolation from the neighbouring height. The same problem was observed for the Windcube unit 6 in Hamburg, but for a height of 150 m. Both problems are likely caused because the signal output at those heights was influenced by a parasite frequency from the local oscillator on the laser signal. Despite this problem, the mean wind speed

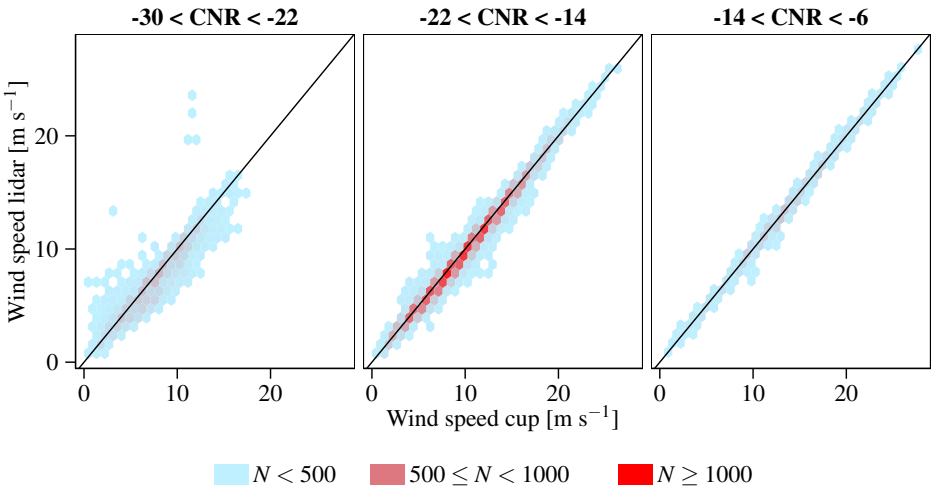

Figure 4.1: The binned wind speed observations from the wind lidar compared to the observations from the cup anemometer at 100 m at Høvsøre. The colour denotes the amount of observations N in a bin.

at other heights agrees very well with the mast measurements and therefore provide a good basis for analyzing the wind profile up to several hundreds meters height.

Furthermore it should be noted that differences between lidar and mast measurements are not necessarily caused by errors in the wind speed obtained from the wind lidar. Since the wind lidar is a non-intrusive instrument, it can be used to estimate flow-distortion effects from the masts. In figure 4.3 (left) the mean wind speed from the cup anemometer U_c divided by the wind speed from the wind lidar U_l at 100 m at Høvsøre is plotted as a function of the wind direction.

The wind speed ratio at 100 m $U_c/U_l > 1$ for northerly flow: this is because the meteorological mast can be in the wake of the wind turbines located to the north, while the lidar measures over a larger horizontal area and is therefore partly outside the wake and measures a higher wind speed than the cup anemometer. The sector between 330° – 30° is therefore not used. An opposite effect can be observed for wind directions around 120° and around 330°, where $U_c/U_l > 1$. This could be due to flow distortion effects of the meteorological mast: a lower wind speed in one of the beam positions can give a incorrect reconstruction of the wind vector from the radial wind speeds. The westerly sector and easterly sector which are used in Chapter 5, 6 and 7 are indicated in the figure. Generally, $U_c/U_l < 1.05$ in those sectors.

In Hamburg (Fig. 4.3, right), the ratio U_s/U_l is more variable as can be seen from the

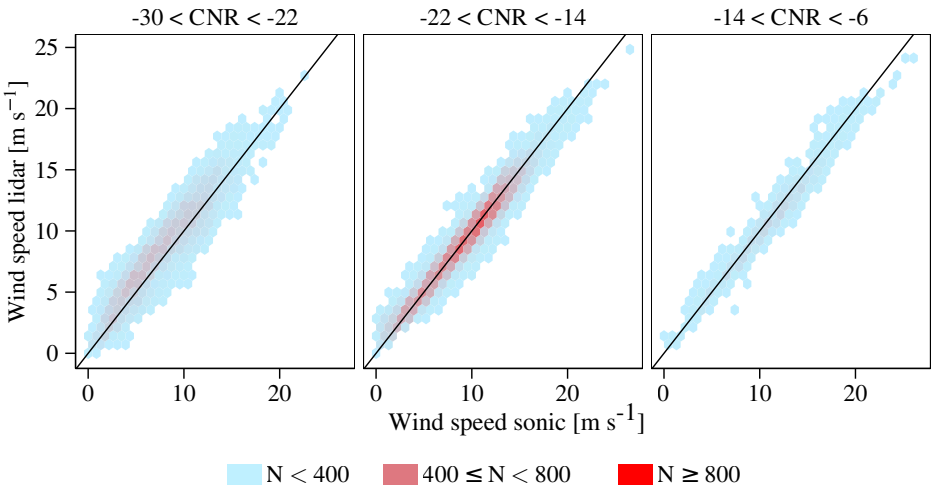

Figure 4.2: The binned wind speed observations from the wind lidar compared to the observations from the sonic anemometer at 250 m at Hamburg. The colour denotes the amount of observations N in a bin.

larger standard deviations for all wind direction bins compared to Høvsøre. The effect of the flow distortion from the television tower on which the instruments are mounted, is most pronounced when the flow is from the North and therefore the sector between 320°–40° is not used in Chapter 7. Unfortunately the effect of the tower is significant for other sectors as well. Still, generally $0.9 < U_s/U_l < 1.1$ for each wind direction bin in the free sector.

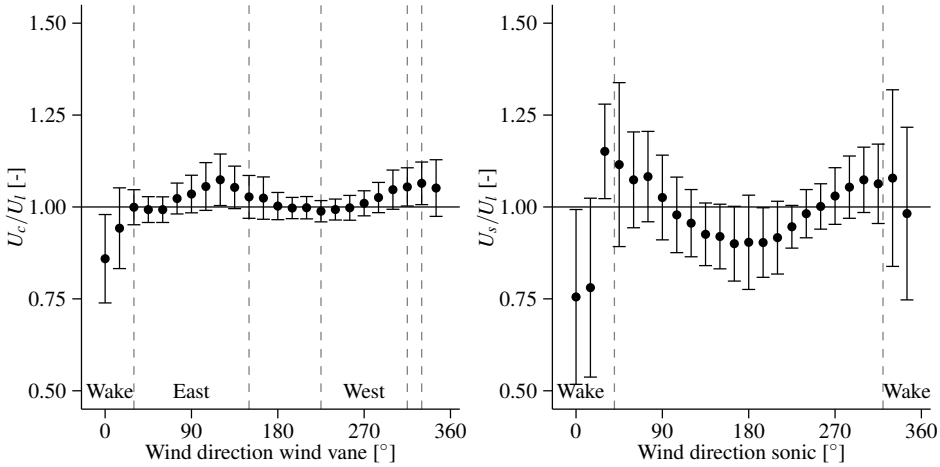

Figure 4.3: The left panel shows the wind speed from the cup anemometer U_c divided by the wind speed from the wind lidar U_l versus the wind direction measured by the wind vane at 100 m at Høvsøre. The right panel shows the wind speed from the sonic anemometer U_c divided by the wind speed from the wind lidar U_l versus the wind direction measured by the sonic anemometer at 250 m at Hamburg. The wind direction is grouped into 15° bins and the median and standard deviation of each bin are shown.

5

ANALYSIS OF DIABATIC FLOW MODIFICATION IN THE INTERNAL BOUNDARY LAYER

5.1 Abstract

Measurements at two meteorological masts in Denmark, Horns Rev in the sea and Høvsøre near the coastline on land, are used to analyze the behaviour of the flow after a smooth-to-rough change in surface conditions. The study shows that the wind profile within the internal boundary layer is controlled by a combination of both downstream and upstream stability and surface roughness conditions. A model based on a diffusion analogy is able to predict the internal boundary layer height well. Modeling the neutral and long-term wind profile with a 3 layer linear interpolation scheme gives good results at Høvsøre. Based on a comparison with a numerical model and the measurements, the constants in the interpolation scheme are slightly adjusted, which yields an improvement for the description of the wind profile in the internal boundary layer.

5.2 Introduction

Predicting the wind speed is important in many areas, including weather forecasting, marine technology and wind energy. On land wind turbines are often installed near the shore, because of favourable wind conditions and grid interconnection facility. For the assessment of wind resources, knowledge on the change of wind speed with height (wind profile) near the shoreline is therefore essential.

The shoreline is associated with considerable changes in surface properties and the occurrence of mesoscale interacting processes, which influence the wind profile. Examples are the formation of sea breezes (Coelingh, 1998), the influence of wave heights and fetch (Lange et al., 2004; Sjöblom and Smedman, 2003) and the formation of an internal boundary layer (IBL) (Rao et al., 1974; Melas and Kambezidis, 1992; Gryning and Batchvarova, 1996).

This chapter has been published as Floors, R., Gryning, S.-E., Peña, A., and Batchvarova, E. (2011b). Analysis of diabatic flow modification in the internal boundary layer. *Meteorol. Zeitschrift*, 20(6):649–659

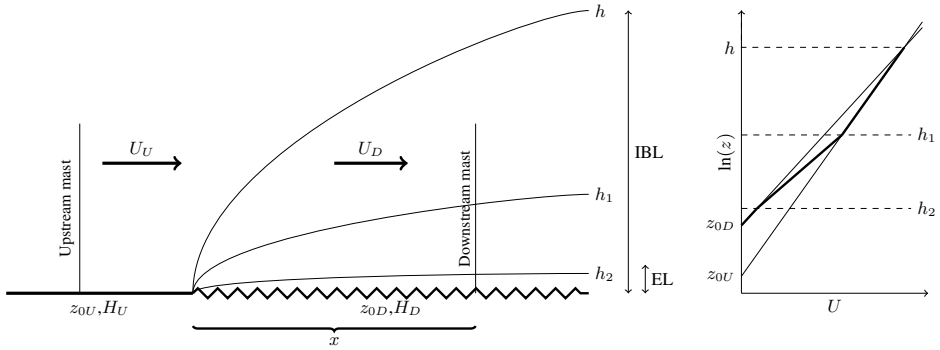

Figure 5.1: Structure of the IBL for a smooth-to-rough transition with measuring masts indicated (left figure). The upstream and downstream wind profile (thin lines) and from the model of Troen and Petersen (1989) (thick line) for a smooth to rough transition (right figure).

There is a considerable body of literature on IBL formation (e.g. Peterson, 1969; Rao et al., 1974; Sempreviva et al., 1990), but studies based on measurements from tall meteorological masts extending above the IBL located downstream from the shoreline are few. Furthermore, the number of available sites that have observations of both upstream and downstream wind profiles is limited (Bergström et al., 1988; Beljaars et al., 1990).

With the development of offshore wind farms, a number of new marine measuring sites has become available. Together with the increased height of meteorological masts, this has provided new possibilities to study the structure of the coastal IBL. In the present study, wind profiles and stability observations at a measuring mast located about 15 km offshore and those of a tall meteorological mast located 1.8 km from the shoreline over land are used to study the IBL structure.

5.3 Theory

5.3.1 Internal boundary layer

In a homogeneous flow, the wind profile depends on the roughness length z_0, the stress τ and the buoyancy flux H. When the flow crosses a step change in roughness (at $x = 0$), a new boundary layer will develop that depends on both upstream and downstream values of z_0, τ and H (see figure 5.1). From now on, the subscripts 0, U, D denote surface, upstream and downstream values, respectively. This layer grows with downwind distance x and is called an internal boundary layer.

The height of the IBL h is not well defined, because there is no sharp border or kink

in terms of friction velocity u_* or wind speed U_z profiles. Shir (1972) argued that h is very different for stress and velocity; when u_* was found to vary up to a height h, the velocity profiles only showed deviations up to the height $h_1 \approx 0.5h$ (see figure 5.1).

In numerical studies (Shir, 1972; Rao et al., 1974) h is defined as the height where the downstream values reach some percentage of the upstream values of the momentum flux. The equilibrium layer (EL) is defined as the zone where τ_D is larger than 90% of its surface value ($\tau_D > 0.90\tau_{0D}$) and its height is called h_2. According to this definition, approximately the lower 10% of the IBL is in equilibrium with the new surface, in analogy with the depth of the surface layer in the planetary boundary layer (PBL). It has been difficult to compare the results of numerical models with observations, because of the lack of measurements from masts that cover the entire IBL.

The accuracy of measurements is often not sufficient to determine where downstream profiles have changed to some percentage of the upstream profiles. The lack of a clear definition for h easily leads to confusion when interpreting different studies (Savelyev and Taylor, 2005). Some studies estimate the height of the IBL where the wind profile has a kink (Bergström et al., 1988; Sempreviva et al., 1990); this height is called h_1 here. In most cases it is easy to determine such a kink, but sometimes it is impossible (Bergström et al., 1988) and the definition of a kink is anyway rather subjective.

Under convective conditions, it is also possible to determine the height of the IBL from the jump in the potential temperature (Θ) profile (Garratt, 1990), often referred to as thermal internal boundary layer (TIBL). This forms the basis of slab models (e.g. Gryning and Batchvarova, 1996).

The contribution of mechanical and convective turbulence to the growth of the TIBL is studied in Gryning and Batchvarova (1990). For a shallow TIBL, the mechanical turbulence is the most important source for its growth. For positive heat flux, the contribution of convective turbulence increases as the layer grows. Gryning and Batchvarova (1990) estimated that the growth of the TIBL is controlled by convective turbulence when $h > -1.4L$, where L is the Obukhov length.

A common approach in determining h in the neutral PBL was proposed by Miyake (1965) and adopted by many authors (see all references in Savelyev and Taylor, 2005). It uses an analogy with the atmospheric dispersion of a passive contaminant. The growth of h with time t is assumed to be proportional to the standard deviation of vertical wind speed σ_w, i.e.

$$\frac{dh}{dt} \propto \sigma_w. \tag{5.1}$$

The growth of an IBL with time is given by

$$\frac{dh}{dt} = \frac{\partial h}{\partial t} + \frac{\partial h}{\partial x}\frac{dx}{dt}. \tag{5.2}$$

Assuming steady state, $\partial h/\partial t = 0$, and $dx/dt = U_z$ gives

$$dh/dt = U_z \partial h/\partial x. \tag{5.3}$$

U_z can be estimated by the logarithmic wind profile. Substituting equation 5.3 into 5.1 and assuming that u_* is proportional to σ_w gives an expression that can be integrated with respect to x and h. When we assume $h = 0$ when $x = 0$, integration gives

$$\frac{h}{z_0}\left[\ln\left(\frac{h}{z_0}\right) - 1\right] + 1 = \frac{C\kappa x}{z_0}, \tag{5.4}$$

where $z_0 = \max(z_{0D}, z_{0U})$, C a constant and κ the von Kármán constant (≈ 0.4).

Different versions of equation 5.4 are summarized in Savelyev and Taylor (2005). For the constant C, many values have been proposed: in the derivation from Miyake (1965), Panofsky (1973) and Troen and Petersen (1989) the values are 1.73, 1.5 and 2.25, respectively. Savelyev and Taylor (2001) uses $z_0 = z_{0U}$ and $C = 1.25(1 + 0.1\ln(z_{0D}/z_{0U}))$. From now on we will use the subscript MI, PA, TP and SA to denote the value of C for the respective authors.

Equation 5.4 is only valid for neutral conditions, where growth is controlled by mechanical turbulence through the so called spin-up term (Gryning and Batchvarova, 1990). This is the case for the first hundreds of meters after the surface change. After that, the growth of the IBL is also controlled by stability, friction velocity and the potential temperature gradient above the IBL (Gryning and Batchvarova, 1990). Józsa et al. (2006) compared a numerical model with the diffusion analogy for neutral stratification and stated that it can be used for fetches up to several kilometers, in agreement with the measurements of Källstrand and Smedman (1997).

5.3.2 Wind profile

Homogeneous conditions

In the surface layer, the lowest part of the boundary layer, the fluxes of momentum and heat are assumed to be constant with height. Therefore, the friction velocity and heat flux observed close to the ground are used to predict the conditions in the whole surface layer.

In non-neutral conditions the wind profile is obtained with help of the flux-profile relationships (Businger et al., 1971; Dyer, 1974) and reads as

$$U_z = \frac{u_{*0}}{\kappa}\left[\ln\left(\frac{z}{z_0}\right) - \psi_m\right], \tag{5.5}$$

where u_{*0} is the friction velocity in the atmospheric surface layer and z the height above the surface. ψ_m is the diabatic correction to the wind profile and is a function of z/L (Beljaars and Holtslag, 1991). Holtslag and De Bruin (1988) showed that the traditional ψ_m-forms did not give satisfactory results in very stable conditions, because the surface layer is very shallow.

L can be obtained from direct measurements of the fluxes (eddy covariance method) as:

$$L = -\frac{{u_*}^3}{\kappa(g/T)\overline{w'\Theta'_v}}, \tag{5.6}$$

where Θ_v is the virtual potential temperature, $\overline{w'\Theta'_{v0}}$ is the vertical kinematic flux of Θ_v, g the gravitational acceleration and T the temperature.

Internal boundary layer profiles

Peterson (1969) used the basic equations for two-dimensional, incompressible, inviscid turbulent flow for neutral stratification to model the wind profile in the IBL. Assuming τ to be proportional to the turbulent kinetic energy (TKE), he provided a theoretical prediction of U_z and u_* profiles in the neutral IBL. It turned out that for a smooth to rough transition, the non-dimensional wind shear $\phi_m = (\kappa z/u_*)(\partial U_z/\partial z)$, being 1 near the surface and at the top of the IBL, showed a maximum. In other words, the wind profile has an inflection point in the middle of the IBL (figure 5.1). The inflection point is located halfway between h_1 and h_2. This was confirmed with observations (Bradley, 1968; Sempreviva et al., 1990). The height of this inflection point is dependent on the magnitude of the roughness change; the larger the change in z_0, the higher the inflection point.

Troen and Petersen (1989) distinguished three layers in the IBL (figure 5.1). At the lowest layer ($z < h_2$) the wind is in equilibrium with the new surface, at the top ($z > h_1$) there is a layer following the upstream wind profile and in between there is a transition between these two layers. This idea is applied in the Wind Atlas Analysis and Application Program (WAsP) (Troen and Petersen, 1989), where the behaviour of the wind profile around the inflection point is a linear interpolation between the upstream and downstream wind profile:

$$U_z = \begin{cases} U_U \frac{\ln(z/z_{0U})}{\ln(c_1 h/z_{0U})} & z \geq c_1 h \\ U_D + (U_U - U_D)\frac{\ln(z/c_2 h)}{\ln(c_1/c_2)} & c_2 h \leq z \leq c_1 h \\ U_D \frac{\ln(z/z_{0D})}{\ln(c_2 h/z_{0D})} & z \leq c_2 h \end{cases} \tag{5.7}$$

where

$$U_U = (u_{*0U}/\kappa)\ln(c_1 h/z_{0U}) \tag{5.8}$$

and

$$U_D = (u_{*0D}/\kappa)\ln(c_2 h/z_{0D}). \tag{5.9}$$

Sempreviva et al. (1990) found $c_1 = 0.3$ and $c_2 = 0.09$ from observations near the North Sea coast of Denmark. Equation 5.7 shows that the IBL wind profile is dependent on h.

The advantage of this model is that with a specific definition of h, u_{*0U} can be estimated from z_{0U}, z_{0D} and u_{*0D} by matching the wind profiles at h_{TP} (figure 5.1):

$$\frac{u_{*0D}}{u_{*0U}} = \frac{\ln(h/z_{0U})}{\ln(h/z_{0D})}. \tag{5.10}$$

This issue is discussed in section 5.5.4.

5.4 Methodology

This study only uses data from westerly wind directions, where $225^\circ < \theta < 315^\circ$. The wind direction θ is measured at 43 m (Horns Rev) and 60 m (Høvsøre). Low and very high wind speeds ($U_z > 25$ and $U_z < 4$ m/s) are removed from the data because they represent conditions where Monin-Obukhov similarity theory (MOST) is often not applicable in the surface layer or EL. The data are classified in 7 different stability regimes according to table 5.1.

5.4.1 Horns Rev

The offshore observations are taken at a meteorological mast, west of Jutland (Denmark) and northwest of the offshore wind farm Horns Rev (figure 5.2). Observations are available from January 2001 till March 2007.

At Horns Rev, L is determined from a bulk method due to lack of turbulence measurements. Using temperature and wind speed differences, a bulk Richardson number (Ri_b) is derived,

$$\mathrm{Ri}_b = \frac{gz(\Theta_{v1} - \Theta_{v2})}{T_z {U_z}^2}, \tag{5.11}$$

with T the temperature, z the measuring height and Θ_{v1} and Θ_{v2} the virtual potential temperatures at 13 m and at the sea surface, respectively. The temperature and humidity are measured at 13 m and U_z is measured at 15 m by a Risø cup anemometer, located at a boom facing the west (255°). The temperature measurements are accurate up to $\pm 0.354^\circ$C and the wind measurements up to ± 0.076 ms^{-1}. The uncertainty of the humidity sensor is not significant for deriving Ri_b. A discussion about the uncertainty in deriving the stability from Ri_b is given in Sathe et al. (2011). Peña et al. (2008) showed that values of the sea surface temperature (SST) observed by satellites correspond well with the measured values of 4 m below mean sea level used here. It is assumed that the humidity at the sea surface is 100%. The sensors gave some unrealistic values for very large and small values of T and dew point temperatures T_d. Therefore data with $T < -5^\circ$C, $T_d < -5^\circ$C, $T > 30^\circ$C and $T_d > 30^\circ$C are removed. The relation between z/L and Ri_b is:

$$\frac{z}{L} = C_1 \mathrm{Ri}_b, \tag{5.12}$$

Table 5.1: The 7 stability classes according to Obukhov Length

Nr.	Stability class name	Obukhov length interval [m]
1	Very unstable (vu)	$-50 \geq L \geq -100$
2	Unstable (u)	$-100 \geq L \geq -200$
3	Near unstable/neutral (nu)	$-200 \geq L \geq -500$
4	Neutral (n)	$\lvert L \rvert \geq 500$
5	Near stable/neutral (ns)	$200 \geq L \geq 500$
6	Stable (s)	$50 \geq L \geq 200$
7	Very stable (vs)	$10 \geq L \geq 50$

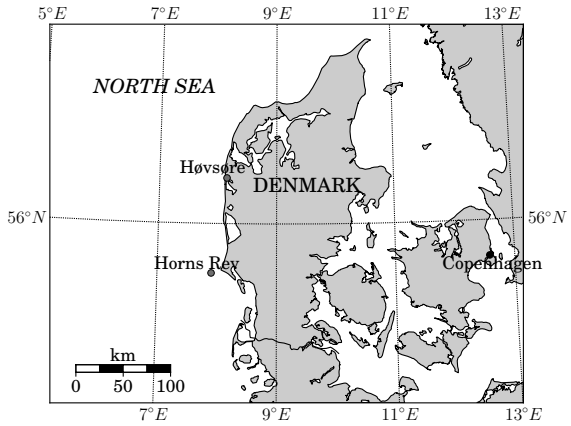

Figure 5.2: Overview of the study area with the Horns Rev wind farm and the Høvsøre measuring site.

for unstable conditions and

$$\frac{z}{L} = \frac{C_2 \mathrm{Ri}_b}{1 - C_3 \mathrm{Ri}_b}, \tag{5.13}$$

for stable conditions ($\mathrm{Ri}_b < {C_3}^{-1}$). Fairall et al. (2003) suggested $C_1 = C_2 \approx 10$ and $C_3 \approx 5$. u_{*U} is calculated by using the wind profile (equation 5.5). Over the sea, z_0 is normally parametrized as a function of u_{*0} so it is possible to find u_{*0} by numerically solving equation 5.5 using for example Charnocks' relation (Charnock, 1955) for z_0:

$$z_0 = \alpha_c \frac{u_{*0}^2}{g}, \tag{5.14}$$

where $\alpha_c \approx 0.012$ at Horns Rev (Peña et al., 2008).

Table 5.2: Filtering of the data.

Filter	Høvsøre	Horns rev
$225 < \theta < 315$	48793 (100%)	47391 (100%)
$4 < U_z < 25$	40328 (82.6%)	41513 (87.6%)
$-5 < T < 30$	-	32339 (68.2%)
Merged	18169 (37.2%)	18169 (38.3%)

5.4.2 Høvsøre

The National Test Station of Wind Turbines is located at Høvsøre, 170 km north of Horns Rev (figure 5.2), about 1.8 km east of the shoreline (figure 5.1). The terrain around Høvsøre is very flat and homogeneous. It mainly consists of grass, crops and a few shrubs. There is one meteorological mast of 116.5 m height and a light mast of 160 m height. At the meteorological mast the wind speed is measured with Risø cup anemometers at heights of 10, 40, 60, 80, 100, 116.5 m. The wind direction is measured with wind vanes at 10, 60 and 100 m. To extend the height range, observations at 160 m at the light tower are also used.

Both the light mast and the meteorological mast are equipped with METEK Scientific USA-1 sonic anemometers. These are available at 10, 20, 40, 60, 80, 100 and 160 m. The sampling frequency of the sonic measurements is 20 Hz. u_* is computed as $u_* = \sqrt{-\overline{u'w'}^2}$, where u and w are the wind speed components aligned and perpendicular to the mean wind direction, respectively, the primes represent fluctuations in the linearly detrended time series and the overbar a 10 minute average. The data are available from February 2004 till now. To relate the stability estimations of the two sites, the two data sets are merged for each time step, resulting in 18169 10 minute mean wind profiles (see table 5.2).

Filtering of wind speed and wind direction is performed in the same fashion as with the Horns Rev data. For filtering the low and high wind speeds the cup anemometer at 10 m was used (table 5.2). At Høvsøre, the data are influenced by the characteristics of the surrounding land. By taking a narrower upwind sector the average distance that winds have to travel from the shoreline to the mast is reduced. In case of northwesterly winds ($\theta = 315^\circ$) this distance is about 2.5 km, whereas for $\theta = 270^\circ$ it is 1.8 km. A narrower sector is not chosen, because the amount of available data is highly reduced.

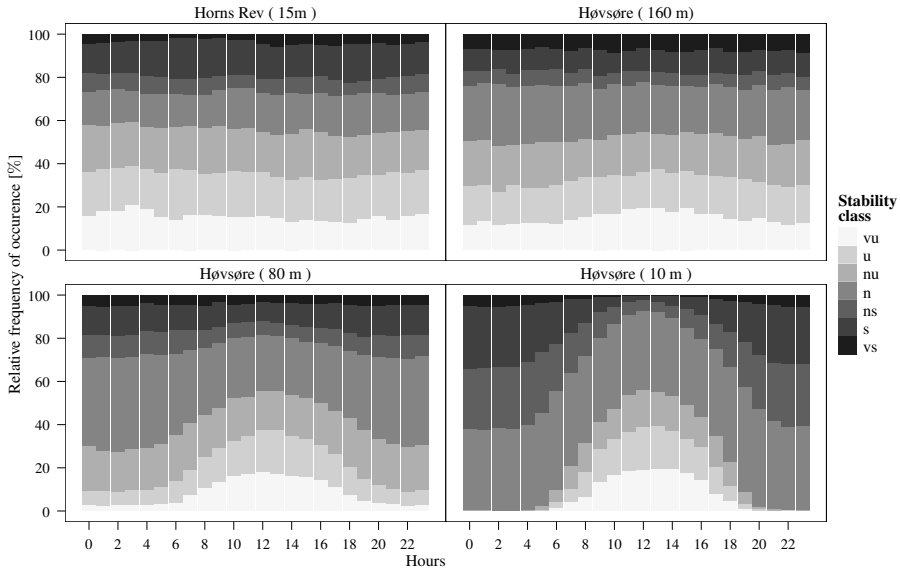

Figure 5.3: Relative frequency of occurrence of stability classes per hour at Høvsøre (2004–2009) and Horns Rev (2002–2006).

5.5 Results

5.5.1 Stability analysis

A forcing of the stability over sea is the difference between the SST and the temperature of the air layer on top of it. The stability is dependent on synoptic scale features, where winds from the northwest tend to be more unstable than winds from the southwest (Sathe et al., 2011). Because the sea has a slow response to irradiation, its diurnal variability in stability is small. On the contrary, on land the stability largely changes along the day with a peak in unstable conditions around noon.

The behaviour of the stability in and above the IBL can be observed in figure 5.3. The stability at Høvsøre is derived from equation 5.6 using the measured fluxes from the sonic anemometer at each height and classified in the categories from table 5.1, whereas for Horns Rev equation 5.12 is used to obtain L. At Horns Rev (top left), the diurnal cycle is absent and the distribution over all stability classes is more or less constant during the whole day. This is not the case for Høvsøre at 10 m: a maximum in unstable cases is present around noon, whereas stable conditions are observed more frequently during the night. Higher up at Høvsøre, the pattern gradually becomes closer to that of Horns Rev.

Another difference arises from the amount of neutral stability cases at both locations, that can be also observed in figure 5.3. At Horns Rev and at greater heights at Høvsøre, the amount of neutral cases is much lower than near the surface in the IBL. This can be related to the lower shear stress above open ocean. The mechanical generated turbulence is larger close to the land surface because of its high roughness, whereas it is low at the smoother ocean. The relative contribution of heat fluxes is therefore more important in the marine boundary layer.

5.5.2 Wind profiles

From the above results it is clear that the stability at Høvsøre depends on height for westerly winds. This affects the wind profile as well. Based on surface layer theory, u_* and L in equation 5.5 are constant with height, an invalid assumption for westerly winds at Høvsøre. To study this issue, the observed dimensionless wind profiles at Høvsøre are compared to the theoretical profiles (equation 5.5), using the stability corrections proposed by Beljaars and Holtslag (1991) for stable and unstable conditions. In figure 5.4a, the theoretical and observed dimensionless wind profiles for the northeasterly sector (30° – 90°) are plotted. This sector is flat and homogeneous (Gryning et al., 2007a) so we expect a profile that is in equilibrium with the surface, which justifies surface layer scaling. The values of u_* and L at 10 m are used in equation 5.5, because they are representative for surface layer scaling at Høvsøre (Gryning et al., 2007b).

The theoretical profiles for homogeneous conditions correspond well with the observations, except for very stable conditions. For the easterly sectors, the nocturnal

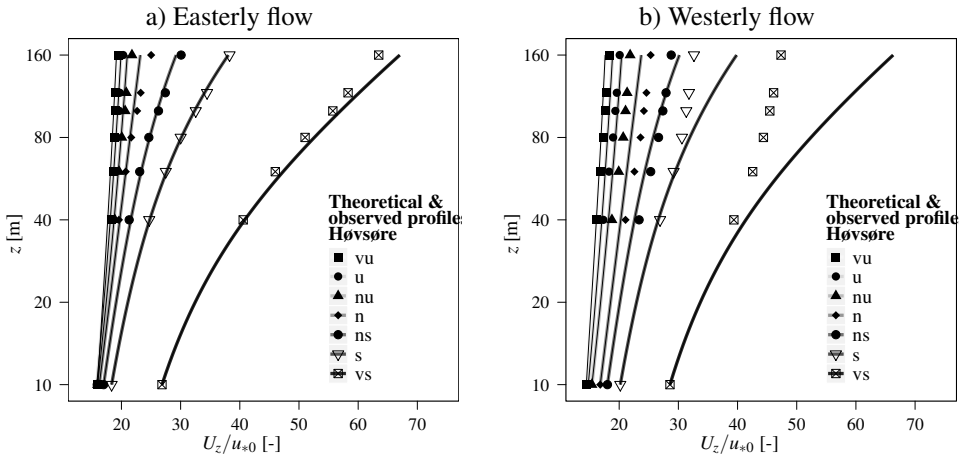

Figure 5.4: Observed (markers) and theoretical (Beljaars and Holtslag, 1991) (solid lines) dimensionless wind profiles for Høvsøre for $30^\circ \leq \theta \leq 90^\circ$ (left) and for $225^\circ \leq \theta \leq 315^\circ$ (right).

low-level jet influences the higher observations in very stable conditions. At 160 m measurements are beyond the surface layer and other length scales, such as the height of the PBL, have to be taken into account (Gryning et al., 2007a).

Figure 5.4b is similar as figure 5.4a, but for westerly winds. Especially in the stable classes there are considerable differences between the measurements and the predicted profiles, caused by the non-constant stress and stability throughout the IBL. The dimensionless wind speed (U_z/u_{*0}) is therefore over predicted higher up. This effect is more pronounced when the IBL is more stable, because it results in a lower IBL height. An alternative for surface layer scaling would be local scaling of L and u_* (Nieuwstadt, 1984). However, this is not practical for predicting wind profiles, because local values are not often available.

Figure 5.4b shows the profiles for a smooth to rough transition and the kink in the wind profile (figure 5.1). The region with relatively high wind shear between h_1 and h_2 in figure 5.1, can be observed in figure 5.4b from approximately 40–80 m. Above 80 m the profiles are steeper, corresponding with u_{*U}.

The upstream stability is an important forcing for the wind profiles above the IBL. To elucidate this, the upstream stability at Horns Rev is determined and the dimensionless wind profiles at Høvsøre are classified according to these stability classes (table 5.1). Figure 5.5 shows the profiles with neutral stability at 20 m at Høvsøre and for different stabilities at Horns Rev. It can be observed that the wind profile above 40 – 80 m is mostly dependent on the offshore stability.

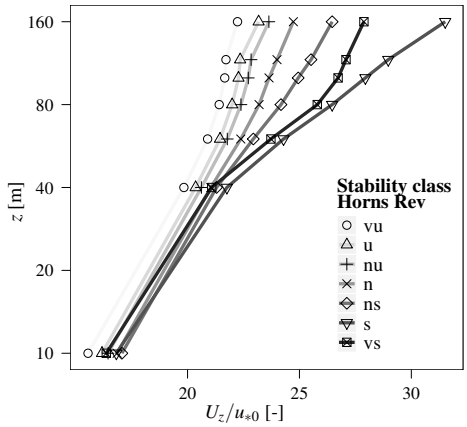

Figure 5.5: Observed downstream neutral dimensionless wind profiles at Høvsøre grouped by the upstream stability at Horns Rev.

5.5.3 Heat and momentum flux profiles

The presence of kinks in the wind profile is only one of many ways to estimate the height of the IBL. The diffusion analogy, based on u_*, and the slab models, driven by $\overline{w'\theta'_v}$, can also be used to derive h. Profiles of these two variables observed at Høvsøre are studied for neutral upwind conditions. By looking at the fluxes for different downstream stability classes, one can determine the height where they cannot any longer be distinguished from the neutral upstream fluxes.

In figure 5.6 (top), the $\overline{w'\Theta'_v}$ profile for different stability classes at Høvsøre is plotted for neutral upwind conditions. Near the surface, large positive heat flux values in unstable conditions and negative values in stable conditions are seen. In the upper layer near the top of the IBL where the stability is neutral, the lines approach the neutral upstream values of $\overline{w'\Theta'_v}$ as expected. For the stable profiles, $\overline{w'\Theta'_v}$ strongly changes in the lowest 40 m only. The heat flux for very stable conditions is not the lowest, because the classification is based on L and not on $\overline{w'\Theta'_v}$ and for these conditions u_* is the lowest, since turbulence is rather supressed (Mahrt, 1999). In unstable conditions, convective eddies penetrate much higher in the IBL, up to at least 160 m.

Figure 5.6 (bottom) shows the normalized friction velocity profile, u_*/u_{*0}. It can be seen that close to the surface, u_* decreases faster with height for stable conditions compared to unstable conditions. In unstable conditions, the eddies cause vertical transport of horizontal momentum to be mixed over a thicker layer. Therefore, the wind experiences more stress at higher heights which in turn leads to lower wind shears. This also means that the EL is higher in unstable conditions compared to stable conditions.

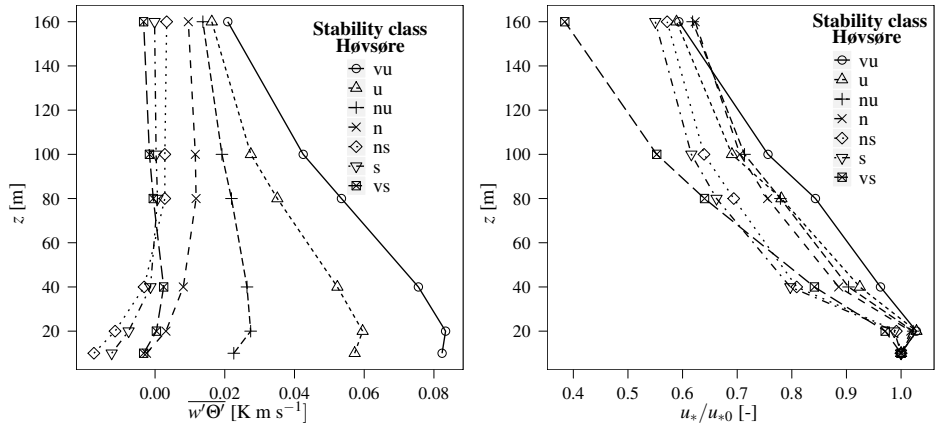

Figure 5.6: Observed $\overline{w'\Theta'}$ (left) and u_* (right) profiles at Høvsøre grouped by the downstream stability for neutral upstream conditions.

5.5.4 Modelling the wind profile in the IBL

Stress profiles

Troen and Petersen (1989) assumed that the long term averaged wind profile is close to neutral for the IBL. This justified the use of the logarithmic profile matching method (fig. 5.1), where both downstream and upstream wind profiles are described by only u_{*0} and z_0. To test the approach of Troen and Petersen (1989), neutral conditions at Høvsøre and Horns Rev are selected. Their IBL height (h_{TP}) is estimated from equation 5.4. At Høvsøre $x \approx 2200$ m, which is an average distance from the coast for $225^\circ \leq \theta \leq 315^\circ$ and z_0 is calculated from equation 5.5 by using U_z and u_* observations at 10 m.

h_{TP} (see table 5.3) is higher than the estimates from other IBL models, as summarized in Savelyev and Taylor (2005). Our observations of u_* from Høvsøre and results from numerical studies confirm that Troen and Petersen (1989) overestimated h and their approach is merely used for profile matching (figure 5.1) and the derivation of u_{*U} from equation 5.7.

To show this, the u_* profile at Høvsøre is plotted in figure 5.7a. It has the curved shape shown in Peterson (1969) and Rao et al. (1974), which is a consequence of the transition from the downstream to the upstream stress values with height. In the same figure, the observations of u_{*0} from 15 m at Horns Rev are plotted together with an expression for the momentum flux based on an empirical fit to data from large eddy

simulations adapted from Zilitinkevich and Esau (2007),

$$u_*(z) = u_{*0}\sqrt{\exp\left(-3\left(\frac{z}{z_i}\right)^2\right)}, \tag{5.15}$$

where the boundary layer height z_i is estimated as

$$z_i = 0.1\frac{u_{*0}}{f}, \tag{5.16}$$

where f is the Coriolis parameter. The observations at Horns Rev agree reasonably well with the empirical expression. As expected, at 160 m in the IBL u_{*D} is close to u_{*U}. The upstream and downstream stress profiles can be normalized as in Peterson (1969) with

$$(u_{*U} - u_{*D})/(u_{*0U} - u_{*0D}) \tag{5.17}$$

and compared with his numerical model (figure 5.7b). The model is run with the average values found for Horns Rev and Høvsøre, $z_{0U} \approx 0.0002$ m, $z_{0D} \approx 0.012$ m for neutral conditions and $z_{0U} \approx 0.0001$ m, $z_{0D} \approx 0.016$ m for all stability conditions. For U_U, we use the value of 116.5 m at Høvsøre, assuming this is above h_2. The observed U_U is not taken from Horns Rev since the measurements are only up to 45 m.

A very shallow layer near the ground up to a normalized height of about 0.07 is in equilibrium. This is close to $c_2 = 0.09$ from Troen and Petersen (1989). From a dimensionless height of 0.6 up to 1, u_* hardly decreases, so it makes more sense to adopt h around $0.6h_{\mathrm{TP}}$, which corresponds better to Panofsky's model. When we compare the results of Peterson (1969) (table 5.3), it seems that h_{TP} corresponds to the height where the term 5.17 equals 0.01, whereas the IBL height defined by Panofsky (1973) (h_{PA}) corresponds better with the height where it is 0.05.

Wind profiles

h has not much practical importance, because it is based on u_* and not on U_z. It is more useful for wind energy to compare the kink in the wind profile (h_1). These differences are often not explicitly mentioned in studies. Here, it is assumed that the wind profile always behaves as that in figure 5.1, so $h_1 \approx 0.5h$ and $h_2 \approx 0.1h$, which are the estimates most commonly used in literature (Shir, 1972; Rao et al., 1974; Savelyev and Taylor, 2005). In Troen and Petersen (1989), $h_1 = 0.3h_{\mathrm{TP}}$ and $h_2 = 0.09h_{\mathrm{TP}}$. To be able to use the profile matching we maintain h_{TP}, but use h_1 and h_2 from Panofsky's model (table 5.3). This gives the new constants for Troen and Petersen (1989), $c_1 \approx 0.35$ and $c_2 \approx 0.07$. With these new constants, the predicted values of h_1 and h_2 are close to those in Bergström et al. (1988) and Savelyev and Taylor (2001) and the wind profile at Høvsøre shows the best comparison with the observations for all stability classes (figure 5.8, bottom). The advantage of using this revised model is that equation 5.10 is still

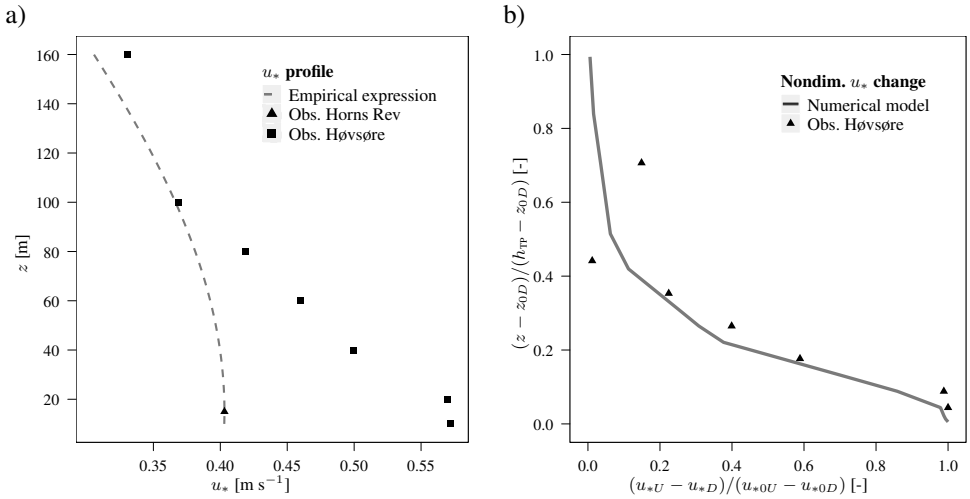

Figure 5.7: The observed u_* profile at Høvsøre with neutral upstream and downstream conditions, the dashed line is an empirical fit of u_* at Horns Rev (eq. 5.15) (left). On the right the nondimensionalized version of the left figure, where the solid line is the result of the numerical model of Peterson (1969) .

Table 5.3: Summary of estimates of h, h_1 and h_2 (in meters) from different models for neutral conditions

	h (IBL)	h_1	h_2 (EL)
Troen and Petersen (1989)			
old (C_{TP}=2.25,c_1=0.3, c_2=0.09)	227	68	20
new (C_{TP}=2.25, c_1=0.35, c_2=0.07)	227	79	16
Panofsky (1973)	157	79	16
$C_{PA} = 1.5$, c_1=0.5, c_2=0.1			
Savelyev and Taylor (2001)	127	64	13
$C_{ST} \approx 1.25$, c_1=0.5, c_2=0.1			
Bergström et al. (1988)	-	82	16
Peterson (1969)			
h: term 5.17= 0.01			
$h_2 : u_{*D}/u_{*0D} = 0.9$	209	-	21
h: term 5.17= 0.05			
$h_2 : u_{*D}/u_{*0D} = 0.9$	127	-	21

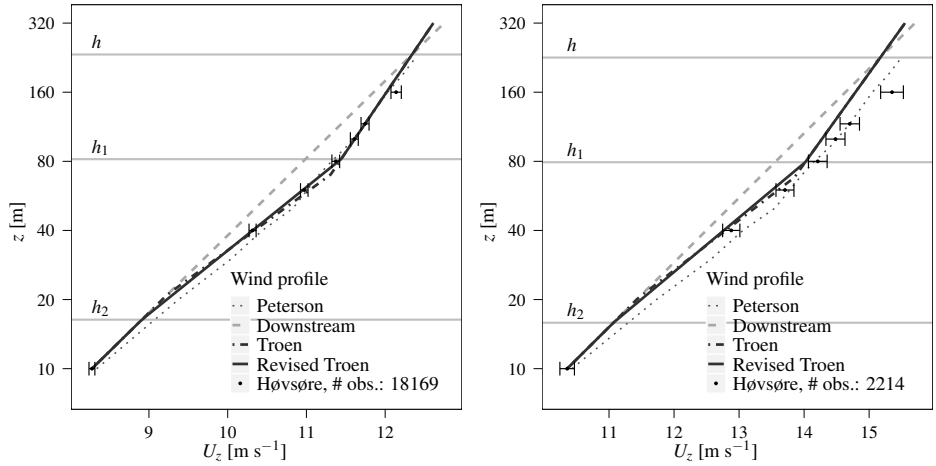

Figure 5.8: Wind profile with the original (dashed black line) and the revised (solid black line) Troen and Petersen (1989) model, the model of Peterson (1969) (thin solid line), an extrapolation of the surface values (grey dashed line) and the observations at Høvsøre (black points). The left figure is for neutral upstream and downstream conditions and the right for all stabilities.

valid and the common definition of $h_1 \approx 0.5h$ and $h_2 \approx 0.1h$ still holds. It can be seen that Peterson's model represents the wind speed well, but the kink in the wind profile is lower than observations.

When data from all stability classes are plotted together (right figure 5.8), the agreement is better than that for neutral cases only (left figure 5.8). Given that the model only needs u_{*D}, z_{0U} and z_{0D}, it is interesting to note that there is almost no difference on most heights. At 160 m the difference is larger, but it is possible that a capping inversion and a low level jet are present, while there is still neutral stratification at the surface (Lange et al., 2004). It could also be related to flow distortion around the light mast (see section 5.4.2).

It is hard to verify at Høvsøre if the height h_2 is well described, because of lack of observations below 40 m. When the original constants from Troen and Petersen (1989) are used, the model predicts values that are just outside the 95% confidence interval (error bars in figure 9) for 60 and 80 m, whereas with the new constants they are within. The RMSE is 0.12 and 0.15 for the new and old model, respectively, so it improves the agreement for all stability classes. This is more important than the prediction for the neutral conditions, because for wind energy prediction all measurement conditions are used for long term means. The better agreement with the model found for all stability conditions in figure 5.8 (bottom) might be due to the predominant unstable upstream conditions

(figure 5.3), which deviate the mean observations to a less sheared wind profile.

5.6 Discussion

Because IBLs develop at every inhomogeneity in the landscape, it is a valuable effort to develop an analytical model to predict the response of both velocity, stress and heat flux profiles. The structure of the IBL is fundamentally different from that of the surface layer, because both heat and momentum fluxes are not constant with height. Even in neutral conditions it is not straightforward to derive the logarithmic wind profile, because u_* varies with height.

There have been efforts in modelling diabatic wind profiles in the IBL (Beljaars et al., 1990), using up- and downstream surface layer values of L and ignoring its vertical distribution. From this study it is clear that the change of L does not necessarily coincide with the change of U_z.

For further research, a meteorological mast in sea straight in front of Høvsøre is advisable, since the meteorological mast to characterize the marine flow was located more than 170 km south of Høvsøre. When matching the two data sets, the atmospheric conditions might have changed when the flow is going from Horns Rev to Høvsøre, which takes about one hour in moderate westerly winds of 7 m/s. With a new sea mast, it will be possible to compare the wind profiles on a specific time, instead of using climatological means only. When a profile of u_{*U} is available it is possible to validate equation 5.15 and the comparsion with Peterson's model will be more robust.

5.7 Conclusion

The structure of the IBL after a smooth-to-rough roughness change was investigated from profiles of friction velocity, heat flux and wind speed at Høvsøre. Near the surface in the EL the flow is nearly in equilibrium with the new surface values. Above it, there is a layer that is a transition between the downstream and upstream flow. Above the IBL, the flow is controlled by upstream conditions.

In the transition layer, the influence of upstream stability increases with height. The diurnal variability is an important forcing for the downstream stability on land, whereas yearly variability is more important over sea. Information on both upstream and downstream stabilities is therefore needed in the IBL. The stability also has an influence on h. In unstable conditions convection increases the growth rate of h, while in stable conditions it is lower. The u_* and $\overline{w'\theta'_v}$ profiles show large differences for each stability class. For diabatic flow, surface layer scaling should not be used for the prediction of the wind profile in the IBL, but it gives good results for homogeneous conditions.

For adiabatic flow, where up- and downstream neutral conditions are selected, the wind profile is well predicted by the model from Troen and Petersen (1989), which uses

z_{0U}, z_{0D} and u_{*D} only. For h, different models give values that are in the range 120–180 m, which agree well with the observed u_* profile. The numerical model from Peterson (1969) was compared to the observations and showed that u_* changes very little above the height where u_{*D} is within 5% of u_{*U}. However, Troen and Petersen (1989) estimated a h that is much higher. The change in wind profile is observed to be about halfway of h. The agreement of the different models and observations shows that for a fetch up to several kilometers the diffusion analogy is an adequate model and support the findings of Källstrand and Smedman (1997) and Józsa et al. (2006).

Slightly different constants are derived for the model of Troen and Petersen (1989), improving the description of the wind profile at Høvsøre for long term means. Although this model is theoretically only valid for stationary, neutral conditions, it also describes the yearly average wind profile very well.

Acknowledgments

The authors would like to thank Ameya Sathe, Jordi Vilà, Niels Otto Jensen and Anna Maria Sempreviva for their input on this work. The data from Horns Rev were kindly provided by Vattenfall A/S and DONG energy A/S as part of the 'Tall Wind' project, which is funded by the Danish Research Agency, the Strategic Research Council, Program for Energy and Environment (Sagsnr. 2104-08-0025). Funding from the EU project contract TREN-FP7EN-219048 NORSEWInD and the EU FP7 Marie Curie Fellowship PIEF-GA-2009-237471-VSABLA is also acknowledged. The study is also related to COST action ES1002. Finally, the Test & Measurement program of the Wind Energy Division at Risø DTU is acknowledged for providing access to the Høvsøre database.

6

THE WIND PROFILE IN THE COASTAL BOUNDARY LAYER: WIND LIDAR MEASUREMENTS AND NUMERICAL MODELLING

Abstract

Traditionally it has been difficult to verify meso-scale model wind predictions against observations in the whole planetary boundary layer (PBL). Here we used measurements from a wind lidar to study the PBL up to 800 m above the surface at a flat coastal site in Denmark during a one month period in autumn. We ran the Weather Research and Forecasting model (WRF) with two different roughness descriptions over land, two different synoptic forcings and two different PBL schemes at two vertical resolutions and evaluated the wind profile against observations from the wind lidar.

The simulated wind profile did not have enough vertical shear in the lower part of the PBL and also had a negative bias higher up in the boundary layer. Near the surface the internal boundary layer and the surface roughness influenced the wind speed, while higher up it was only influenced by the PBL scheme and the synoptic forcing. By replacing the roughness value for the land-use category in the model with a more representative mesoscale roughness, the observed bias in friction velocity was reduced. A higher-order PBL scheme simulated the wind profile from the west with a lower wind-speed bias at the top of the PBL. For easterly winds low-level jets contributed to a negative wind-speed bias around 300 m and were better simulated by the first-order scheme. In all simulations, the wind-profile shape, wind speed and turbulent fluxes were not improved when a higher vertical resolution or different synoptic forcing were used.

6.1 Introduction

The change of wind speed with height in the lower planetary boundary layer (PBL) and its development in time are key issues for the wind energy industry. As wind turbines

This chapter has been published as Floors, R., Vincent, C. L., Gryning, S.-E., Peña, A., and Batchvarova, E. (2013b). The Wind Profile in the Coastal Boundary Layer: Wind Lidar Measurements and Numerical Modelling. *Boundary-Layer Meteorol.*, 147(3):469–491

become taller, our knowledge of the wind speed above the surface layer has to be improved. The Monin-Obukhov similarity theory (MOST) provides a solid framework for predicting wind profiles in the surface layer (Businger et al., 1971). However, many questions remain unsolved about the wind profile throughout the PBL, due to the interaction of synoptic, mesoscale and microscale processes. A variety of tools is used to study these interactions, for example the resistance law (Zilitinkevich and Esau, 2005), mixing length theory (Gryning et al., 2007a) or numerical models such as the Weather Research and Forecasting model (WRF) (Skamarock et al., 2005).

Recent studies have shown that even the state-of-the-art mesoscale WRF model often poorly represents turbulent parameters such as the friction velocity u_* and sensible heat flux H (Floors et al., 2011a; Gibbs et al., 2011; Peña and Hahmann, 2011; Shin and Hong, 2011; Steeneveld et al., 2011). For the description, modelling and forecasting of wind and turbulence it is essential to have a realistic estimate of the magnitude of the surface-layer fluxes. However, many model verification studies focus on readily available parameters such as wind speed and temperature (Zhang and Zheng, 2004). Therefore it is not clear whether the WRF model predicts these parameters well due to a realistic representation of the physics or because of 'tuning' of the model constants.

It is common to study the model physics by using a single column model (SCM) (Cuxart et al., 2005). This has the advantage that different physical parametrizations can be studied at low computational cost, but the disadvantage that synoptic effects (e.g. advection, short-term temporal changes of the geostrophic wind and baroclinicity), negligible near the surface but important higher up in the boundary layer, are poorly represented in SCMs (Baas et al., 2010). Such effects can be simulated with the three-dimensional WRF model when the model domain is large enough to resolve the synoptic scales. In such a set-up the outer boundary is forced with synoptic information from re-analysis data of large-scale numerical weather models. Studies that compared PBL parametrizations in the WRF model revealed that the non-local schemes predicted near-surface variables and profiles more realistically in unstable conditions and that the higher-order schemes performed better in stable conditions (Hu et al., 2010; Shin and Hong, 2011).

However, verification of the vertical structure of the PBL often proves difficult, because of lack of data of sufficient resolution in time and space. Few meteorological masts are higher than 100 m and radiosoundings are often too infrequent for detailed studies. Here, we therefore used a wind lidar to observe the wind profile. This technology has been commercially available for more than six years and has improved in terms of reliability, accuracy and range (Peña et al., 2009b).

In this paper, wind-speed measurements from the wind lidar up to 800 m are combined with observations from a meteorological mast at a coastal site in Denmark to provide information about both upper air and near-surface winds and turbulence. The surface variables are carefully examined for their representativeness when compared to the simulated values at the comparable grid cell. In this way, we can study the behaviour

of a full column in the WRF model and still simulate the large-scale fluctuations that are usually absent in SCMs. We then study the sensitivity of the wind profile, simulated by the WRF model with two PBL parametrizations and two vertical model resolutions, to both lower boundary conditions and synoptic scale forcing. The surface-layer momentum flux is studied by redefining the land-use properties and the synoptic forcing using the National Center for Environmental Prediction (NCEP) final analysis (FNL) and ERA-Interim re-analysis data. By comparing the high quality measurements with the mesoscale model, we can determine whether mesoscale modelling in the coastal zone is hampered by resolution and boundary conditions or by the physics of the parametrizations. The three nested domains resemble typical use of the WRF model for operational weather and wind forecasting, thus enabling us to identify important uncertainties in wind-speed forecasts in coastal areas.

In Section 7.2 we discuss how the WRF model predicts the atmospheric flow and up to which height unresolved features of the terrain contribute to differences between the model and the observations. The measurements and the model set-up are presented in section 6.3. Section 6.4.1 gives an overview of the analysed period and in Section 6.4.2, the wind profiles and surface-layer fluxes are presented. Section 6.4.3 discusses the influence of the internal boundary layer, Section 6.4.4 describes the influence of atmospheric stability on the profiles and Section 6.4.5 treats the influence of using two different types of (re)analysis data for the forcing of the model. Finally, in Section 6.5 and 6.6 we discuss the results and present concluding remarks.

6.2 Theory

6.2.1 Parametrizations in the WRF model

The WRF model solves the Euler equations for momentum, heat and moisture (Skamarock et al., 2005). The most important parametrizations for the shape of the wind profile are the surface-layer and PBL schemes. The PBL schemes model the turbulent flux divergence and there are two main families: first-order and higher-order closures. To represent both families, the first order Yonsei University (YSU) PBL scheme and the 1.5-order Mellor-Yamada-Nakanishi-Niino (MYNN) scheme are applied in this study. A detailed description of the PBL parametrization for YSU and MYNN can be found in Hong et al. (2006) and Nakanishi and Niino (2009), respectively.

YSU boundary-layer scheme

For atmospheric flow, the velocity components (u, v, w) on a regular x, y, z grid are commonly decomposed into a mean (U, V, W) and turbulent part (u', v', w'), where the horizontal bar denotes a time average. The YSU scheme describes the turbulent fluxes

of momentum using a modified K-theory,

$$\overline{u'w'} = -K_m\left(\frac{\partial U}{\partial z} - \gamma_c\right) - \overline{u'w'}_h\left(\frac{z}{h}\right)^3, \tag{6.1}$$

$$\overline{v'w'} = -K_m\left(\frac{\partial V}{\partial z} - \gamma_c\right) - \overline{v'w'}_h\left(\frac{z}{h}\right)^3, \tag{6.2}$$

where z is the height above the ground, γ_c represents a correction to the local gradient to include non-local mixing, and $\overline{u'w'}_h$ and $\overline{v'w'}_h$ represent the entrainment fluxes at the top of the boundary layer (height h). The YSU scheme prescribes the values of the eddy diffusivity K_m directly,

$$K_m = u_* \kappa z \phi_m^{-1}\left(1 - \frac{z}{h}\right)^2, \tag{6.3}$$

where u_* is the friction velocity, κ is the von Kármán constant and ϕ_m is the dimensionless wind shear,

$$\phi_m = \left(\frac{\kappa z}{u_*}\right)\frac{\partial U_z}{\partial z}, \tag{6.4}$$

where U_z is the magnitude of the wind vector. The dimensionless shear is a function of z/L (Businger et al., 1971), where the Obukhov length is given by,

$$L = -\frac{{u_{*0}}^3}{\kappa(g/\theta_0)(\overline{w'\theta'_v})_0}. \tag{6.5}$$

where g is the gravitational acceleration, θ is the potential temperature and $\overline{w'\theta'}$ is the kinematic heat flux. Throughout this paper the subscripts 0 and v denote a surface-layer value and a virtual heat flux or temperature, respectively. For unstable conditions the velocity scale in Eq. 6.3 is,

$$w_s = \left(u_{*0}^3 + 8\kappa w_{*b}^3 \frac{z}{h}\right)^{1/3}, \tag{6.6}$$

where w_{*b} is the convective velocity scale, $[(g/\theta_0)(\overline{w'\theta'_v})_0 h]^{1/3}$.

Hong (2010) made several changes to the YSU scheme in stable conditions that are also applied in this study. The most important ones are those related to the surface Rossby number dependence of the critical Richardson number for the determination of the PBL height and the determination of the K_m profile.

MYNN boundary-layer scheme

The MYNN scheme, which is based on the Mellor-Yamada prognostic turbulent kinetic energy (TKE) scheme (Mellor et al., 1982), also uses K-theory,

$$\overline{u'w'} = -K_m\frac{\partial U}{\partial z}, \tag{6.7}$$

$$\overline{v'w'} = -K_m \frac{\partial V}{\partial z}, \tag{6.8}$$

but here K_m is given by,

$$K_m = lqS, \tag{6.9}$$

where l is a length scale, $q = \sqrt{2e}$ with e being the TKE and S is a stability function (Nakanishi and Niino, 2009). In the Mellor-Yamada type models, q is given by a prognostic equation,

$$\frac{d}{dt}\left(\frac{q^2}{2}\right) + A_v = P_s + P_b + \varepsilon, \tag{6.10}$$

where t represents time and the second term on the left-hand side represents the vertical advection of e,

$$A_v = \frac{\partial}{\partial z}\left[lqS\frac{\partial}{\partial z}\left(\frac{q}{2}\right)\right], \tag{6.11}$$

P_s is the shear production,

$$P_s = -\overline{u'w'}\frac{\partial U}{\partial z} - \overline{u'v'}\frac{\partial V}{\partial z}, \tag{6.12}$$

P_b is the buoyancy generation or destruction,

$$P_b = \frac{g}{\theta_0}\overline{w'\theta'_v} \tag{6.13}$$

and ε is the dissipation,

$$\varepsilon \propto \frac{q^3}{l}. \tag{6.14}$$

Horizontally, e is currently only advected as a passive tracer. This can be an important drawback in very inhomogeneous conditions, when near-surface diffusion does not represent well the diffusion higher up in the PBL. l is a function of atmospheric stability and calculated by inverse summation of a surface-layer length scale ($\sim \kappa z$), a bulk PBL buoyancy length scale and a PBL height length scale.

Surface-layer scheme

In the WRF model, exchange coefficients are calculated as part of the surface-layer scheme, based on a bulk method using MOST. In the surface layer the fluxes of momentum and heat are assumed to be constant with height. Therefore, the stress τ, sensible heat flux H and latent heat flux LE close to the ground are used to predict the conditions in the whole surface layer,

$$\tau = \rho {u_{*0}}^2, \tag{6.15}$$

$$H = -\rho c_p u_{*0} \theta_{*0}, \tag{6.16}$$

$$LE = L_v \rho u_{*0} q_{*0}, \tag{6.17}$$

where ρ is the air density, c_p is the specific heat of air, L_v is the latent heat of vaporization and θ_{*0} and q_{*0} are turbulent scales for temperature and humidity, respectively. Because the present study focusses on momentum we only present here the relationship for u_{*0},

$$u_{*0} = \frac{\kappa U_{z_1}}{\ln(z_1/z_0) - \psi_m(z_1/L)}. \tag{6.18}$$

Here z_1 is the height of the first model level, U_{z_1} is the horizontal wind speed magnitude at height z_1, z_0 is the aerodynamic roughness length and ψ_m represents the effect of atmospheric stability. The latter is derived by integrating ϕ_m (Eq. 6.4) with respect to height. More details on the numerical implementation of the scheme can be found in Jiménez et al. (2012), who show that by removing several unphysical limits a more realistic representation of the surface layer can be achieved when compared with a mesoscale network of observations.

6.2.2 Mesoscale modelling of the PBL

To reduce the influence of unresolved microscale features on observations it is preferable to compare a horizontal spatial average of observations with mesoscale model simulations (Zhang and Zheng, 2004; Hu et al., 2010). However, an extensive network of stations with measurements of turbulence and the vertical structure of the PBL is rarely available, so it is also common to directly compare results from a single grid point with in situ observations (Shin and Hong, 2011; Steeneveld et al., 2011). However, this results in sensitivity to measurement errors or measurements not being representative for the entire grid cell of the model. The effects of horizontal spatial averaging were studied by Gibbs et al. (2011) by comparing large-eddy simulations (LES) with WRF model fields for horizontal grid spacings from 1 to 4 km. They found that a bias in mean wind speed and friction velocity was not reduced when a finer horizontal resolution was used in the WRF model.

When comparing mesoscale model results from a single grid cell, the roughness length can be considered as a parameter that represents the average contribution of all roughness elements inside the model grid cell. The regional roughness length for momentum can be defined as the parameter that gives the correct surface stress for the area as a whole when used in connection with a flux-profile relationship (Eq. 6.18).

To minimize the difference between model results and observations when evaluating mesoscale models, the flow at the height where observations are taken has to be spatially homogeneous in a statistical sense at scales equal to or greater than the grid size of the

mesoscale model. Below this height one cannot attribute all deviations between observed and simulated profiles to the model physics only because of the unresolved features. The interface between the layers defines the blending height introduced by Wieringa (1986) and adopted by many others (Mahrt, 1996; Batchvarova et al., 2001).

Mahrt (1996) reviewed approaches to estimate bulk properties of the atmosphere based on the horizontal length scale of the surface heterogeneities l_c. The blending height l_b can be estimated as,

$$l_b = 2\left(\frac{\sigma_w}{U_z}\right)^2 l_c, \tag{6.19}$$

where σ_w is the standard deviation of the vertical wind-speed fluctuations. When l_b extends above the height at which the bulk approach is applied, it requires spatial averaging of the surface fluxes.

In stable conditions, turbulence is suppressed and at greater heights the flow becomes decoupled from the surface. The balance between the pressure gradient force and the Coriolis force is disturbed due to the disappearing friction and the flow accelerates; this creates a low-level jet (LLJ). An intercomparison of single-column models from eleven different operational and mesoscale models with 21 PBL parametrizations revealed that the height of the simulated wind-speed maximum of the LLJ was usually too large (Cuxart et al., 2005). First-order closure schemes represented LLJs particularly poorly, but higher-order closure schemes did not perform well either. The eddy diffusivity in very stable conditions in a mesoscale model is often higher in order to prevent unrealistic cooling near the surface (Derbyshire, 1999). McCabe and Brown (2006) argued that it is also higher compared to observations in order to account for unresolved heterogeneities at the surface.

6.3 Methodology

6.3.1 Measurements

The measurements were carried out at the National Test Station of Wind Turbines at Høvsøre, Denmark, which is located about 1.8 km east of the shoreline in western Jutland (Figs. 1 and 2) and the flow is therefore strongly influenced by the sea-land contrast. For westerly flow the internal boundary layer that develops at the smooth-to-rough roughness change influences the turbulent fluxes well beyond the surface layer (Floors et al., 2011b). For easterly flow the scattered trees and houses cause heterogeneity on a smaller scale and to the south there is a bay. The site is equipped with a dedicated meteorological mast of 116.5 m height with wind-speed measurements from Risø cup anemometers at 2, 10, 40, 60, 80 and 100 m. The wind direction was measured with a wind vane at 60 m.

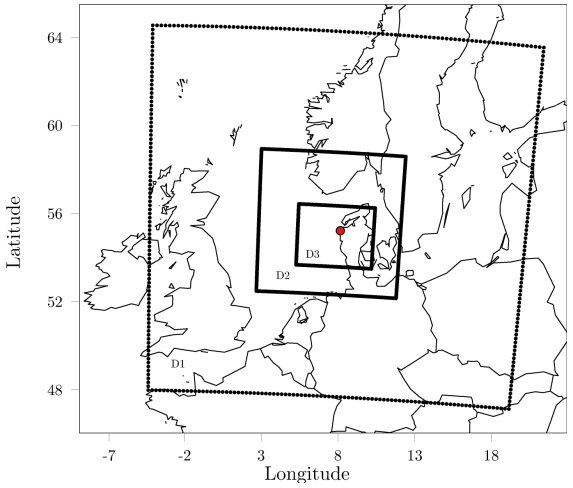

Figure 6.1: Map of the three nested WRF model domains D1, D2 and D3 with a horizontal resolution of 18, 6 and 2 km, respectively. The Høvsøre site is indicated with a red dot.

Turbulence measurements were performed with ultrasonic anemometers (METEK Scientific USA-1) at 10, 20, 40, 60, 80, and 100 m on the meteorological mast. The sampling frequency of the sonic measurements was 20 Hz. All measured turbulent variables were processed using EC-PACK version 2.5.23 and estimated in 10-min averages (Van Dijk et al., 2004). The turbulent fluxes were estimated using a planar-fit method (Wilczak et al., 2001) and rotated such that the mean transversal wind component was zero. Additionally, a cross-wind and frequency-response correction were applied. The time series of the turbulent velocities were linearly de-trended. Then, u_* was computed as the square root of the covariance of the vertical and along-wind speed components. It is assumed that u_* at 10 m was representative of the friction velocity u_{*0} in the surface layer. $(\overline{w'\theta'})_0$ was computed in a similar way, but using fluctuations in θ. The classification according to atmospheric stability used in this study is based on L, which can be estimated from direct measurements of the fluxes using Eq. 7.9.

A pulsed wind lidar (WindCube WLS70) operated at the site from April 2010 until April 2011. The wind lidar measured wind speed and direction every 50 m starting at 100 m above the ground and reaching up to 2 km height depending on the aerosol content of the atmosphere. The wind lidar was equipped with a rotating silicon prism providing four scans around the zenith, 90° from each other at an inclination angle (relative to the zenith) of 15°. Each scan takes approximately 10 s and u, v and w time series were recorded at that rate from the radial velocities estimated from the Doppler shift at each scanning position. The data were stored as 10-min averages.

Table 6.1: Atmospheric stability classification according to Obukhov length, L, used for the analysis. Data from the sonic anemometer at 10 m were used. N indicates the number of profiles in each stability class. The wind profiles are up to 650 m height for the easterly sector and up to 800 m height for the westerly sector.

Stability class name	L interval [m]	East N	West N
Unstable	$-1000 \leq L \leq -50$	41	134
Neutral	$\|L\| \geq 1000$	35	182
Stable	$1000 \geq L \geq 50$	173	750
Very stable	$50 \geq L \geq 10$	13	30
Total		**262**	**1096**

A wind lidar needs aerosols to measure the wind speed. Above the PBL there are fewer aerosols and therefore the wind lidar signal (with a wavelength of 1.55 μm) weakens and becomes noisy. The reported range of measurements depends on a threshold on the 10-min averaged carrier-to-noise ratio (CNR). This threshold (-22 dB) was chosen based on a good correlation between wind-speed observations from mast and wind lidar and was used as an estimate for the PBL height.

The measuring and modelling timespan consists of two periods, 15–30 September 2010 and 15–31 October 2010. These periods were chosen based on both high availability of wind lidar observations and observed meteorological conditions. A Pearson product-moment correlation coefficient R was computed to assess the relationship between the wind lidar and the cup anemometer at the height where they overlapped (≈ 100 m). Using linear regression fitted through the origin, a coefficient of determination R^2 and slope coefficient of 0.997 and 1.01 were found, respectively.

The data were classified into two categories to prevent influence from the bay and the wind turbines south and north of the site, respectively. Based on the wind direction at 60 m the westerly sector was chosen between 225° and 315° and the easterly sector between 030° and 150°. Both sectors are shown in Fig. 6.2 and the number of analyzed profiles in each stability class is summarized in Table 6.1.

The blending height for the easterly sector was estimated from Eq. 6.19 using $l_c \approx 500$ m based on the typical size of the homogeneous sub-areas in Fig. 6.2. The measurements from 10 m were usually above the blending height $l_b \approx 10$ m, so the easterly flow can be considered homogeneous and Eq. 6.18 is valid in the surface layer.

LLJs in this study were detected using the criteria of Baas et al. (2009), viz. there is a LLJ if there is a maximum in the observed or simulated wind profile that is more than 2 m s^{-1} and 25% larger than the next minimum in wind speed above it.

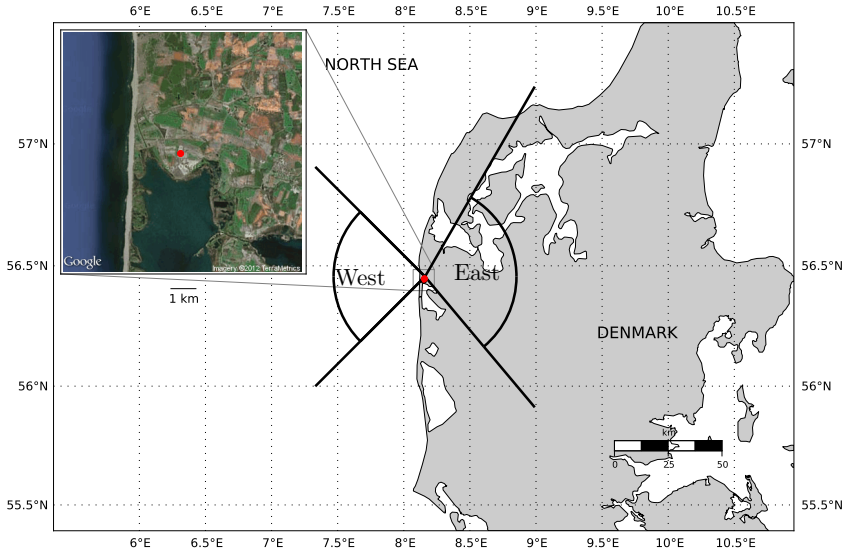

Figure 6.2: Map and satellite photograph with the westerly sector (225° < wind direction < 315°) and easterly sector (030° < wind direction < 150°) at Høvsøre. The location of the meteorological mast is indicated with a red dot.

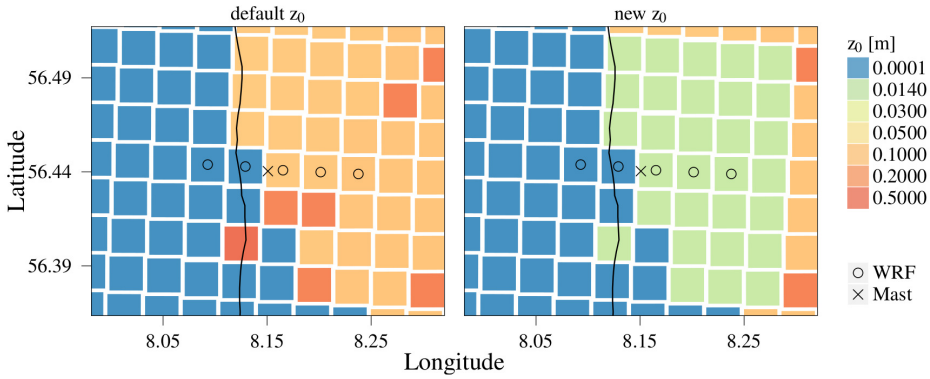

Figure 6.3: Assigned roughness length (z_0) for the model grid with a default (left) and realistic roughness (right). The location of the meteorological mast and the grid points from the WRF model that are used in the analysis are indicated with markers.

6.3.2 Model simulations

In this study, wind profiles were predicted using the Advanced Research WRF model version 3.4 (Skamarock et al., 2005), developed by the National Centre for Atmospheric Research (NCAR). A set-up of three domains covering northern Europe was used, with a horizontal grid size of 18, 6 and 2 km. The grid point from the 2-km resolution innermost grid at Høvsøre was located 1000 m east and 100 m north of the measuring point (mast and Windcube70, see Fig. 6.3).

The model was run in prognostic mode starting every day at 1800 UTC. Data for initial and boundary conditions came from two sources: the final (FNL) operational global analysis data from the NCEP and the ERA-Interim re-analysis data (Dee et al., 2011) from the European Centre for Medium-Range Weather Forecasts (ECMWF). These data were available every six hours on a 1° x 1° grid. The real-time global sea-surface temperature analysis from NCEP was used. Allowing a 6-hour spin-up period, the model fields from 7 to 30 hours were used to generate a continuous time series with a temporal resolution of 10 minutes. The timestep in the model was 120 s for the outermost domain and decreased with factors 3 and 9 for model domains 2 and 3, respectively.

Fig. 6.3 shows that z_0 in the WRF model is between 0.1–0.5 m at the Høvsøre area. This range is much higher than the observed roughness at Høvsøre. When Eq. 6.18 was used to derive z_0, using u_*, L and U determined from the sonic and cup-anemometer measurements in neutral conditions at 10 and 40 m, long-term mean roughness lengths of 0.017 ± 0.0005 m and 0.016 ± 0.0007 m, respectively, were found. Based on these findings the roughness map, i.e. the land-use properties, in the WRF model was adjusted for the 30 land grid points closest to the site (Fig. 6.3).

For westerly winds, the surface-layer fluxes are expected to vary with horizontal position in the first grid cell after the roughness change at the height of the first model level (≈ 13 m). This is because the equilibrium layer reaches approximately 16 m at the site (Floors et al., 2011b). For this grid cell, spatial averaging of the surface-layer fluxes has to be considered (Sect. 6.2.2).

A summary of the model physics is given in Table 6.2. Standard options were used, except for the two alternative PBL schemes (YSU and MYNN) and the surface layer scheme of Jiménez et al. (2012). To quantify the effect of vertical resolution, simulations with 41 and 63 levels are used, although the height of the first model level is not changed since this would introduce a sensitivity to the surface-layer scheme.

Because there were no humidity or radiation measurements at the site, the sensible heat flux could not be obtained from the sonic-based heat flux (Schotanus et al., 1983). Instead, the sensible heat flux inferred from the WRF model (Eq. 6.16) was corrected to represent a similar heat flux that is measured by the sonic,

$$H_{corr} = H + 0.51 T c_p \frac{L_v E}{L_v}, \tag{6.20}$$

where T is the temperature. In the YSU scheme the PBL height is determined based

Table 6.2: Summary of the simulations and observations for the two periods 15–30 Sep. and 15–31 Oct. In the names of the simulations the first letter represents the MYNN (M) or YSU (Y) PBL schemes, the second letter represents the simulations with the corrected (C) roughness or with the ERA (E) interim boundary conditions and the subscript denotes the number of vertical levels used.

Simulations

Name	PBL scheme	No. vertical levels (within range of lidar)	Boundary conditions	Roughness length z_0 [m]
M_{41}	MYNN	41 (8)	FNL	0.080
Y_{41}	YSU	41 (8)	FNL	0.080
M_{63}	MYNN	63 (22)	FNL	0.080
Y_{63}	YSU	63 (22)	FNL	0.080
MC_{41}	MYNN	41 (8)	FNL	0.015
YC_{41}	YSU	41 (8)	FNL	0.015
ME_{41}	MYNN	41 (8)	ERA	0.080
YE_{41}	YSU	41 (8)	ERA	0.080

Physical options used for all simulations: Noah land surface scheme Skamarock et al. (2005), Thompson microphysics scheme Thompson et al. (2004), RRTM longwave radiation Mlawer et al. (1997), Dudhia shortwave radiation Dudhia (1989)

Observations

Data source	Heights [m]
Cup	10, 40, 60, 80, 100
Sonic	10
Lidar	100–2000 (50 m interval)

on the Richardson number (Hong, 2010). In the MYNN scheme it is estimated based on an increase of θ_v and the maximum of TKE, which should give a good estimation in both unstable and stable conditions. It should be kept in mind that the WRF PBL height is determined with meteorological variables, while the wind-lidar PBL height is based on the aerosol content of the atmosphere (i.e. the mixing-layer height). This can give large differences in stable conditions when there is a residual layer with aerosols and a shallow stable PBL or cloud conditions not well simulated in the model.

6.4 Results

6.4.1 Synoptic overview

Time series of simulated and measured data at 100 m height for September and October are shown in Fig. 6.4. Only the low vertical resolution runs are shown. The overlapping

cup and wind lidar measurements agreed very well during the whole period. The gaps in the time series of the wind-lidar data are caused by filtering based on CNR. All model simulations predicted the trend and the variability of the wind speed well. In September the synoptic-scale conditions were characterized by a shift from a strong westerly circulation to a situation with an anticyclone over Scandinavia with easterly winds in Denmark. October was characterized by strong winds and large fluctuations in wind speed.

For both sectors stable conditions prevailed over unstable conditions near the surface (Table 6.1). In September the stable PBLs and associated LLJs were observed in the episodes with easterly winds. The occurrence of the LLJs is indicated with a vertical line in Fig. 6.4, indicating that the number of LLJs in the observations was larger than in the simulations. For westerly winds in both September and October, advection of air from the relatively warm North Sea caused a slightly negative heat flux close to the surface and a prevalence of stable conditions.

6.4.2 Wind profiles and surface-layer fluxes

Easterly sector

Fig. 6.5 shows the mean simulated wind profile for the easterly sector compared with the observations. For each level, error bars of $\pm\sigma/\sqrt{n}$ are denoted. Here σ is the standard deviation of the observed wind speeds for a given height and n is the number of observations. The agreement between wind speeds from the wind lidar and from the mast is excellent at 100 m. The wind lidar observations show a slightly lower wind speed at 250 m than expected from interpolation from the neighbouring height, because the signal output at that height was influenced by interference from an internal oscillator on the laser signal. Only profiles with CNR> -22 dB at all heights up to 650 m are analyzed. Both the MYNN and YSU PBL schemes showed a large underestimation for the wind speed above 40 m. The YSU scheme simulated the height of the wind-speed maximum correctly at ≈ 400 m, while the MYNN scheme did not show a distinct wind-speed maximum. Despite the differences in determination, the simulated and observed PBL height (horizontal lines in Fig. 6.5) agreed rather well. The influence of LLJs and stability is further discussed in Sect. 6.4.4.

Because the roughness and surface-layer fluxes are important for the shape of the wind profile, Table 6.3 shows the results of linear regression between the simulated and observed variables to identify both the slope coefficient and R^2. The model runs M_{41} and Y_{41} overestimated u_{*0} (Table 6.3). Simulations using a lower roughness (MC_{41} and YC_{41}) reduced u_{*0} to more realistic values. H_{corr} was underestimated by the MYNN scheme, while the YSU scheme simulated H_{corr} well.

The simulated 10 m winds were interpolated by the surface-layer scheme using Eq. 6.18. For the other heights the model levels were within 5 m of the observations. Because the gradient in wind speed at larger heights was small, we neglect the effect of the height

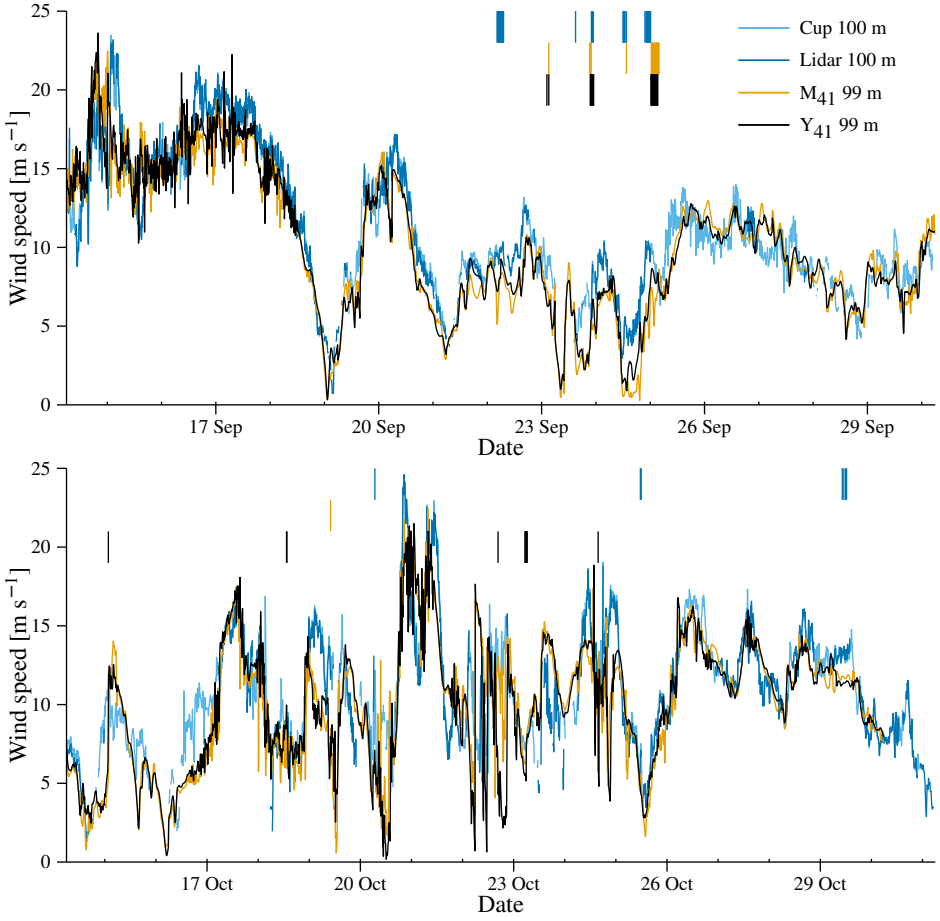

Figure 6.4: Time series of measured and simulated wind speed for 15–30 September (upper panel) and 15–31 October 2010 (lower panel). A vertical line indicates the presence of a LLJ in the wind profile, where the colour indicates in which type of data it occurs (legend). The ticks on the x-axis mark the initialization of the simulations every 24 hours at 1800 UTC. The abbreviations for the simulations are shown in Table 6.2

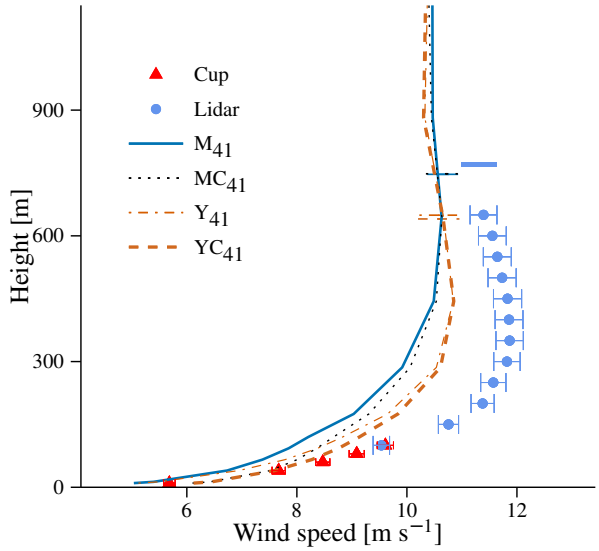

Figure 6.5: Measured and simulated mean wind-speed profiles for easterly winds. The horizontal lines indicate the PBL height. The error bars indicate the standard error of the mean for each height. Simulations are with the MYNN and YSU PBL schemes using 41 vertical levels and two different land surface roughnesses. The abbreviations in the legend are described in Table 6.2

difference between the simulated and observed wind speeds. The simulations with the default roughness (M_{41} and Y_{41}) underestimated the wind speed at 10 m, while those with the realistic roughness slightly overestimated it. At 100 m there was a large negative bias in wind speed, whereas at 650 m the difference between simulated and observed winds speeds reduced and became less dependent on roughness and the PBL scheme.

Westerly sector

Because the flow from the westerly sector was characterized by the transition from sea to land, a cross section of five grid points from the simulations perpendicular to the coastline near Høvsøre was investigated. The locations of the grid points are indicated in Fig. 6.3 where negative distances correspond to grid points over sea. The boundary-layer height is higher for westerly than for easterly flow due to the high wind speed and slightly unstable upstream conditions. Therefore, the wind profile up to 800 m is shown in Fig. 6.6.

Upstream at sea (-4 km) the simulated profiles show a high near-surface wind speed which decreases once the flow crosses the shoreline. The realistic surface-roughness

Table 6.3: Slope coefficient and R^2 of linear regression through the origin between the simulated and measured momentum flux, heat flux and wind speeds at 10, 100 and 650 m for easterly winds. The WRF model output is the instantaneous value taken every ten minutes and the mast and wind lidar observations are 10-minute means. The abbreviations are explained in Table 6.2.

	slope				R^2			
Var.	M_{41}	MC_{41}	Y_{41}	YC_{41}	M_{41}	MC_{41}	Y_{41}	YC_{41}
u_{*0}	1.09	0.99	1.09	0.98	0.45	0.40	0.50	0.43
H_{corr}	0.79	0.81	0.98	0.96	0.37	0.40	0.50	0.49
U_{10}	0.88	1.07	0.90	1.07	0.41	0.40	0.57	0.50
U_{100}	0.84	0.90	0.89	0.93	0.78	0.79	0.79	0.78
U_{650}	0.96	0.96	0.96	0.96	0.85	0.85	0.85	0.85

simulations (right) show a lower wind-speed bias at 10 m when an equilibrium with the surface-layer fluxes formed after several kilometres (Sect. 6.4.3).

At the grid cell closest to Høvsøre, none of the PBL schemes simulated well the high observed shear in the layer between 0–200 m. Increasing the vertical resolution from 8 to 22 levels within the range of the wind lidar did not have any noticeable effect on the shear in this layer (not shown). When the simulated wind profile from 200 m up to the PBL height was compared with the observations, the MYNN scheme approached the free-flow wind speed rather well. The YSU scheme still had a significant negative wind speed bias at the PBL height. The PBL height at sea was around 900 m for both the MYNN and the YSU scheme, whereas it was approximately 200 m higher at the model grid point near Høvsøre. In reality it is approximately constant up to several kilometres inland, because the vertical growth of the internal boundary layer versus horizontal distance is approximately 1:20 (Shir, 1972). Table 6.4 summarizes the results of a linear regression analysis between the simulated and the measured u_{*0}, H_{corr} and U values for the simulations with the default and the realistic roughness for westerly winds. The slope coefficient of u_{*0} is higher than one (i.e. an overestimation) for the default roughness

Table 6.4: Same as in Table 6.3, but for westerly winds.

	slope				R^2			
Var.	M_{41}	MC_{41}	Y_{41}	YC_{41}	M_{41}	MC_{41}	Y_{41}	YC_{41}
u_{*0}	1.35	1.08	1.32	1.05	0.69	0.70	0.67	0.65
H_{corr}	0.86	0.76	0.88	0.77	0.53	0.54	0.64	0.61
U_{10}	0.97	1.06	0.95	1.03	0.68	0.70	0.66	0.66
U_{100}	0.93	0.95	0.94	0.96	0.72	0.73	0.72	0.72
U_{650}	0.98	0.98	0.95	0.96	0.72	0.74	0.75	0.75

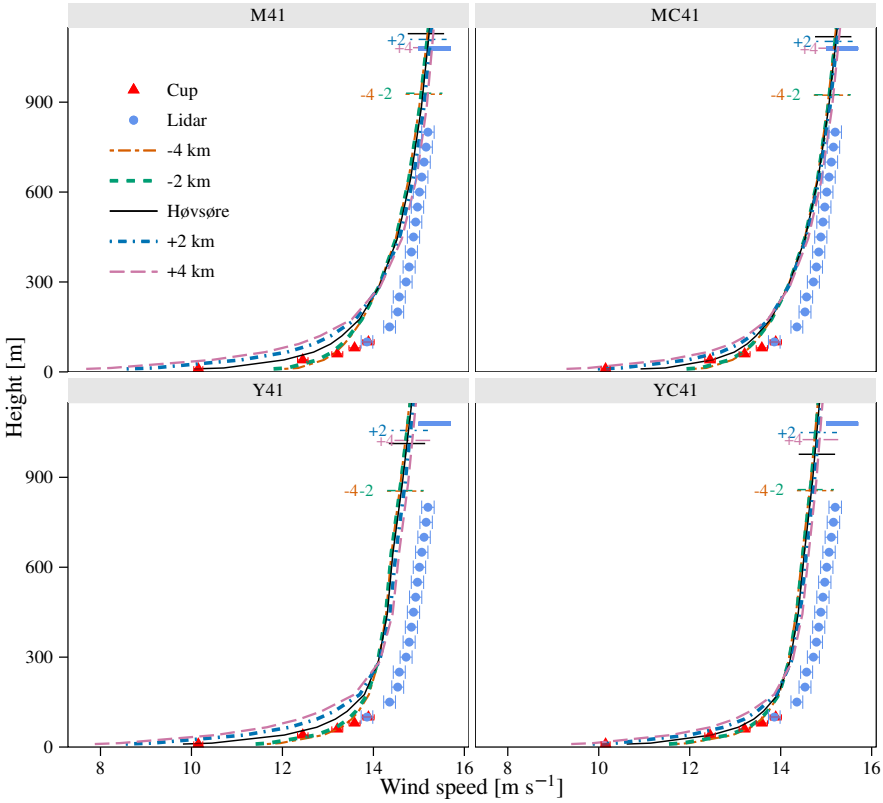

Figure 6.6: As Fig. 6.5, but for westerly winds for different grid points in the WRF model (Fig. 6.3). Simulations with the MYNN (top) and YSU (bottom) PBL schemes using 41 vertical levels and the default (left) and realistic (right) surface roughness are shown .

simulations and even larger than for easterly flow. The simulations with a more realistic roughness largely decreased the overestimation in u_{*0}, but it resulted in a small positive bias in 10-metre wind speeds. H_{corr} had a negative bias for all simulations.

6.4.3 Internal boundary layer

To determine the cause for the large negative bias of the wind speed for westerly winds, an investigation of the variables that govern the shape of the wind profile is needed. Fig. 6.7 (left) shows the mean value of the roughness length from observations and for the model grid points on the cross section. The observed roughness length is derived from the measurements at 10 m using the logarithmic wind profile (Eq. 6.18). In the simulations over land it is a parameter from the land-surface scheme and at sea it is calculated with Charnock's relation (Charnock, 1955).

There was a large jump from the roughness over the sea to the roughness on land (Fig. 6.7, left). The roughness of the adjusted run, $z_0 = 0.015$ m, corresponded better with the roughness derived from the observed wind profiles, whereas $z_0 \approx 0.08$ m was too high for the default set-up. The observed roughness length was slightly lower than the roughness length of the MC_{41} simulation because only data of the relatively smooth westerly sector were used.

Fig. 6.7 (right) illustrates the friction velocity for the five grid points. The smooth-to-rough roughness change resulted in a high simulated friction velocity at Høvsøre, which then decreased further inland. This is in agreement with experimental and numerical studies of the flow in the internal boundary layer, but the effect is found very close to the coastline only (Shir, 1972). The equilibrium layer of the internal boundary layer, where the fluxes are in equilibrium with the new surface roughness, extends to approximately 16 m at the meteorological mast (Floors et al., 2011b). One may think that it is unrealistic that for both the WRF model simulations, the surface-layer fluxes have not reached their equilibrium values more than 2 km at downwind distances from the coastline. However, this is not surprising because the WRF model needs more than one grid point to adjust to the new conditions. This also implies that near-surface wind forecasts near the shoreline are inherently uncertain and illustrates the problem with simulating meteorological conditions in a coastal area.

It is also possible that the surface-layer scheme calculated a too high u_{*0}, because the observed dimensionless shear in the coastal area can be different from the simulated one (Vickers and Mahrt, 1999). Above the equilibrium layer the observed dimensionless wind shear in neutral conditions can be up to 50% larger than one, because U decreases faster with height than u_* (Shir, 1972). Because the height of the equilibrium layer is a function of z/L as well, it is possible that the traditional ψ_m functions do not fit well the observations at Høvsøre.

An underestimation of the ϕ_m function leads to an overestimation of u_{0*} (equation 6.4). Therefore we estimated ϕ_m from Eq. (6.4) for both the easterly and westerly

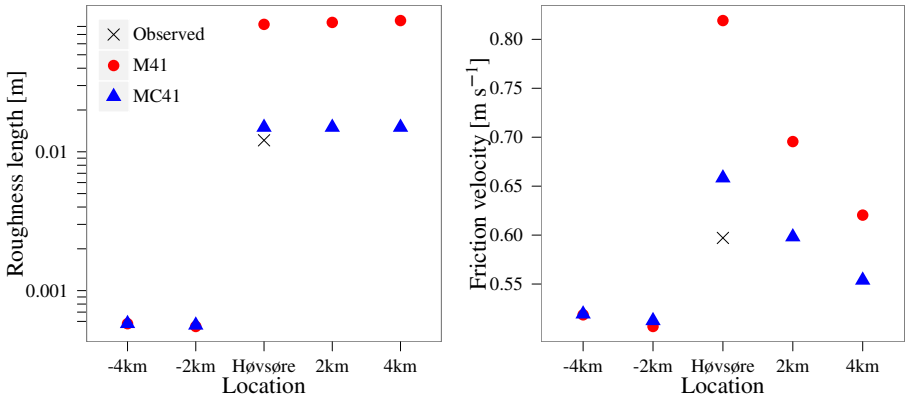

Figure 6.7: Simulated and observed mean roughness length (left) and friction velocity (right) for different locations from Fig. 6.3 in the WRF model. Only winds from the westerly sector simulated by the MYNN scheme are shown, but the results were similar for the YSU scheme.

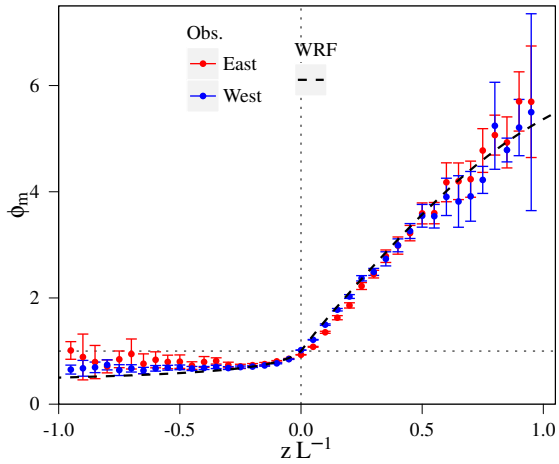

Figure 6.8: Binned observed dimensionless shear versus dimensionless stability parameter z/L with error bars indicating the standard error of the mean in a bin. The dashed line represents the stability function that is used in the surface-layer scheme in the WRF model. The horizontal dotted line has a value of unity.

sector for the period 2004–2011, to investigate whether ϕ_m is wrongly diagnosed in WRF causing an overestimation in u_{*0}. The ϕ_m function (Businger et al., 1971; Cheng et al., 2005) approximated numerically in the surface-layer scheme in the WRF model is shown together with the observations in Fig. 6.8. The observed ϕ_m is determined from the wind-speed difference between the cup anemometers at 10 and 2 m and u_* at 10 m.

In figure 6.8 the observed ϕ_m was very close to ϕ_m from the WRF model for westerly winds (blue points). There was more scatter for easterly winds, because there were fewer observations (red points). The observed and simulated ϕ_m were very close to 1 for both easterly and westerly winds in neutral conditions. For easterly winds with $z/L < -0.5$ the model predicted a lower value than the measurements. However, there was no systematic difference between easterly and westerly ϕ_m observations for neutral and stable conditions that were most frequently observed in the simulation period.

Although the coastline clearly plays a role for the surface-layer fluxes and near-surface wind speed, the large wind-speed underestimation at larger heights cannot be explained. In Fig. 6.5 and 6.6 the simulated wind speed is also much lower than observed above 200 m. Likely candidates to partly explain such biases are differences between the simulated and observed PBL height or a negative bias in wind speed in the re-analysis data.

6.4.4 Stability

To study the influence of stability on the shape of the wind profile, mean normalized wind profiles were classified according to atmospheric stability classes (Table 6.1). A classification based on near-surface stability is not useful for the westerly sector, because the shape of the profile is also influenced by the upstream stability at sea which was not available for this study. Therefore, Fig. 6.9 shows the simulated and measured mean dimensionless wind profiles for the easterly sector only.

In neutral and unstable conditions the shape of the profiles was simulated well, but there was an underestimation in simulated dimensionless wind speed. For unstable conditions the dimensionless wind speed was already underestimated near the surface, related to a wrongly diagnosed u_{*0}. In particular in stable and very stable conditions there was a large underestimation in simulated dimensionless wind speeds. Because the classification is based on the observed L value, the dimensionless wind-speed profile consists of profiles that have different simulated L values. In other words, the surface-layer scheme also plays a major role in this comparison. Unfortunately there were not enough data available to compare observed and simulated profiles that were in the same stability class.

Still, in very stable conditions the observed profile shows a distinct LLJ around 250 m. Both PBL schemes at both vertical resolutions reproduce this feature, but it is simulated at a higher height and with a smaller wind-speed maximum than observed. Both schemes simulate fewer occurrences of LLJs than observed (Fig. 6.4). Furthermore, it

was found that the number of simulated LLJs was highly dependent on the frequency of the initialization: when the WRF model was run in continuous mode for 10 days in a row, not a single LLJ was simulated. The starting time of the WRF simulations at 1800 UTC can be favourable for the representation of LLJs, because at that time the stable boundary layer is already formed and reflected in the initial conditions. Based on the more frequently observed LLJs and the distinct shape of the profiles with a LLJ nose, a wrongly diagnosed stability is a candidate for partly explaining the negative bias for the easterly sector.

6.4.5 Forcing

As shown in Figs. 6.5 and 6.6, the observed and simulated wind profiles did not approach the same geostrophic wind speed near the top of the boundary layer. In a comparison between the ERA-Interim re-analysis and NCEP FNL analysis data it was observed that wind speeds at 900 hPa around the outer model domain (D3 in Fig. 6.1) were on average higher in the ERA-Interim re-analysis than in the NCEP FNL analysis data for this period. Because the (re)analysis data were available every 6 hours, only 28 profiles were available for a comparison with the observations (Fig. 6.10, left). Due to the lower resolution a grid point at sea, $\approx$ 10 km west of Høvsøre, was used for both the ERA-Interim and NCEP FNL data. The (re)analysis wind speeds are interpolated on pressure levels leading to erroneous model heights below 200 m and those heights are therefore not shown. In Fig. 6.10 (left), the NCEP FNL analysis showed nearly the same wind speed above 800 m as the WRF simulation with the MYNN PBL scheme, but the ERA-Interim showed a wind speed that was $\approx$ 1 m s^{-1} higher than the NCEP FNL data. A negative bias in the WRF model simulations at larger heights can be introduced when forcing the model with wind speeds that are too low.

To investigate this effect the simulations were repeated but using the ERA-Interim data (Fig. 6.10 right). The profiles were available every 10 minutes in the WRF simulations, resulting in a lower standard error of mean. The difference between observations and the WRF simulations initialized with the NCEP FNL analysis data (M_{41} and Y_{41}) versus those initialized with ERA-Interim data (ME_{41} and YE_{41}) was generally small near the surface, but became more pronounced higher up in the PBL. The ME_{41} and YE_{41} simulations for both sectors had slightly lower wind speeds above the PBL than the M_{41} and Y_{41} simulations, despite the fact that in Fig. 6.10 (left) the ERA-Interim re-analysis had a higher wind speed than the NCEP FNL analysis. The fact that a bias in the direct comparison between the wind lidar and the re-analysis data did not lead to a corresponding bias in the WRF simulations suggests that the bias is also related to the choice of the PBL scheme but dependent on the choice of forcing. The shape of the wind profiles did not appear to be sensitive to the choice of forcing.

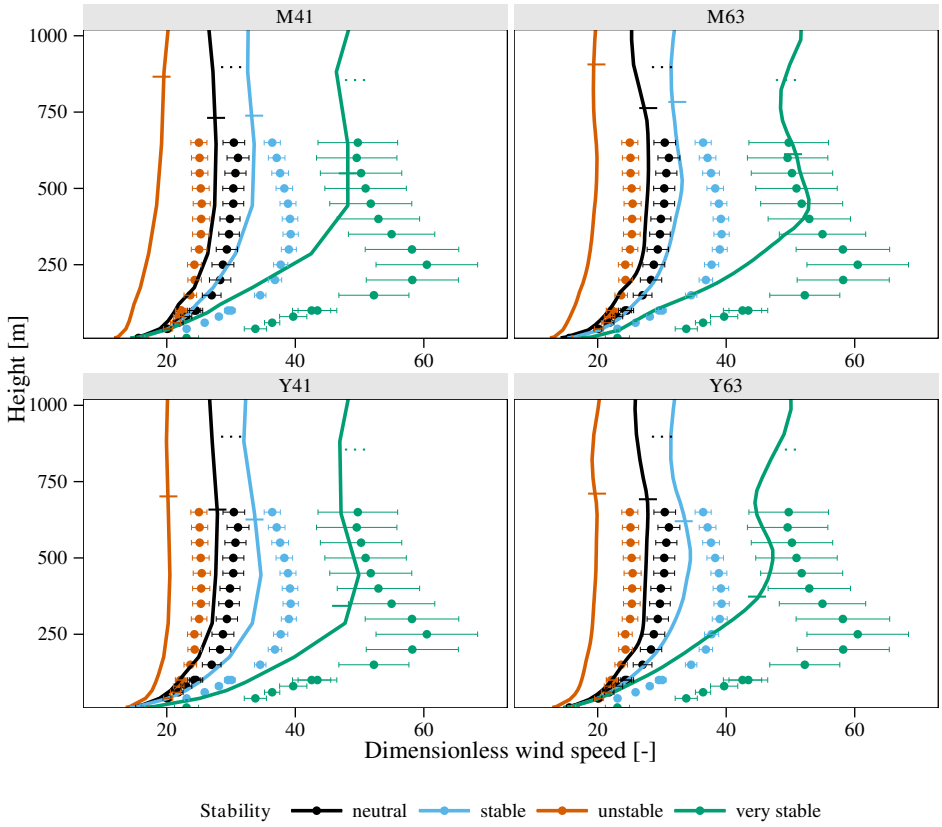

Figure 6.9: Normalized wind profiles from the easterly sector for different atmospheric stability classes, where both WRF profiles (lines) and cup and lidar observations (dots with error bars) are normalized with the observed friction velocity at 10 m. Simulations are shown with the MYNN (top) and YSU (bottom) PBL schemes using 41 vertical levels (left) and 63 vertical levels (right). The default roughness length is used in all schemes and the PBL height is indicated with a solid and dashed horizontal line for the model and the observations, respectively. The mean observed PBL height is > 1000 m in the stable and unstable class and they are therefore not shown.

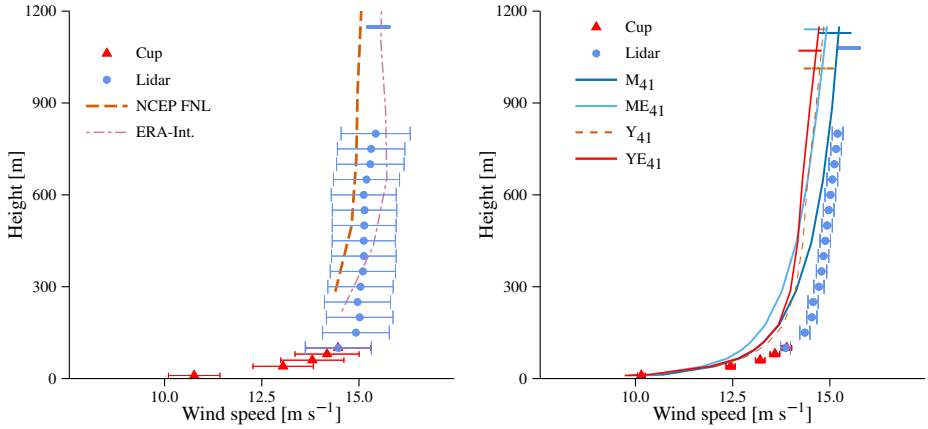

Figure 6.10: The mean wind speed profiles for the westerly sector from the NCEP FNL analysis and ERA-Interim re-analysis (left) and from the WRF simulations using the NCEP FNL analysis and ERA-Interim re-analysis data as boundary conditions (right) compared with the observations. The abbreviations in the legend are described in Table 6.2. The PBL height is indicated with a horizontal line and the error bars indicate the standard error of mean for each level.

6.5 Discussion

Taking all simulations into consideration, none of the variables presented here can entirely explain the wind-speed bias above 200 m, but there are many other variables and setup options in a mesoscale model that could be implicated in causing such bias. Firstly, adjusting the model surface roughness in the surroundings of the measurement site might be insufficient to reduce the overall bias of the model. The WRF model currently uses a look-up table to estimate the roughness length for different land-use categories. However, the land-use categories are defined rather coarsely and a large range of roughness lengths can be grouped under one land-use class. To investigate the effect of a large-scale roughness underestimation in the WRF model, an additional model simulation was performed with a 75% reduction in roughness throughout all the domains, but this only reduced the negative bias by $\approx 1\%$ at 650 m.

For westerly flow the roughness description of the sea can be misdiagnosed by using Charnock's relation, for example when swell is not taken into account. Because the shape of profile above 160 m for westerly winds is largely determined by the marine boundary layer, improvements to the representation of winds at sea could also be beneficial for the model performance (Sušelj and Sood, 2010). The sea-surface temperatures can also be wrongly diagnosed, leading to erroneous heat fluxes that influence the shape

of the upstream wind profile.

In addition the effect of horizontal resolution can be a significant factor in simulating the large roughness changes in the coastal zone. The apparent lag in the response of the wind profiles (Fig. 6.6) and surface-layer fluxes (Fig. 6.7) suggests that increasing the number of grid points between the shoreline and the observations might improve modelling results. However, this brings the grid size close to the size of the largest eddies in the PBL that are parametrized in a mesoscale model and thus requires changes to the parametrization schemes (Wyngaard, 2004).

Finally, the horizontal diffusion can be too high to represent the large changes in wind speed occurring near the coast and lowering the diffusivity might improve these results (Belušić and Güttler, 2010). However, the diffusivity is used in mesoscale models to give reasonable results in all circumstances, so it is not clear whether introducing more variability in the model would lead to better results on a synoptic scale.

6.6 Summary and Conclusions

The vertical momentum transfer in the coastal boundary layer and the shape of the wind profile was simulated with version 3.4 of the WRF-ARW model for two periods with flow from the east over land and flow from the west with the presence of the sea and an internal boundary layer. Simulations were performed with first-order and 1.5-order closure schemes and two vertical resolutions. The default roughness length in the WRF model was too high compared to that derived from measurements. Therefore, simulations with the default and a more realistic surface roughness were performed. Two different (re)analysis datasets were used to force the mesoscale simulations.

The flow was mostly from the west and characterized by an internal boundary layer that develops after the smooth-to-rough change in surface conditions at the coast line. At the first grid point after the roughness change the surface-layer fluxes were very sensitive to the assigned roughness on land, which resulted in an overestimation of $\approx 40\%$ when compared to the observed momentum and heat fluxes. Reducing the roughness length in the model gave a more realistic behaviour of the adjustment of the surface-layer fluxes. However, the adjustment to the new equilibrium values of the surface-layer fluxes took place over several grid points corresponding to 2–6 km. This was also reflected in the wind profiles, which showed large changes in wind speed between 10–200 m when moving land inward. In all cases the simulated wind profiles were less sheared than those observed and especially at lower levels the shear was underpredicted.

For easterly flow, simulations with both the first-order and 1.5-order PBL schemes largely underpredicted the wind speed. None of the schemes simulated as many LLJs as observed. Using simulations that were initialized every 10 days instead of every day resulted in even fewer simulated LLJs, which suggests that the frequency of initialization is also important for correctly modelling LLJs. For both schemes the poor representation

of stable conditions contributed to a negative bias around 100–200 m in the wind profile and a misrepresentation of the shape of the wind profile.

Both the NCEP FNL and ERA-Interim data were used as initial conditions. They influenced the wind speed higher up in the PBL, but they did not help to better represent the shape of the profile. For all simulations the effect of vertical resolution on the wind profile was minor, even near large wind-speed gradients such as in the internal boundary layer or within a LLJ. Thus, in the set-up used here the PBL scheme was mostly responsible for the shape of the profile, the re-analysis data mostly influenced the magnitude of wind speed at greater levels and the roughness and the internal boundary layer largely affected the surface-layer fluxes and the wind speed near the surface.

The observed behaviour of the surface-layer fluxes and wind profiles suggests that mesoscale model fields should be treated with care near the coastline. The negative wind-speed bias in both sectors results in a large underestimation of mean wind speed, which is important for wind turbines that are often located near the shoreline and are becoming larger in size. The new wind lidar measurements proved to be highly useful for evaluating the performance of the PBL schemes. The wind lidar availability was high and the wind speed showed no bias compared to observations from cup anemometers. Also the possibility of using the wind lidar to estimate the boundary-layer height is promising and needs further attention. Future work will combine the continuous measurements of turbulence fluxes and wind profiles for longer periods and for different locations, hereby providing a better understanding of the behaviour of numerical weather prediction models.

Acknowledgements

We would like to thank Andrea Hahmann and Joakim Nielsen for their input in the discussions about the WRF model and three reviewers for their constructive comments. The study is supported by the Danish Research Agency Strategic Research Council (Sagsnr. 2104-08-0025) “Tall wind” project, the Nordic Centre of Excellence programme CRAICC and the EU FP7-People-IEF VSABLA (PIEF-GA-2009-237471). The contribution of C.L. Vincent was supported by the Danish Council for Independent Research - Technology and Production Sciences individual post-doc project (case number 10-093196). TEM section at DTU Wind Energy is acknowledged for maintenance of the data base for all measurements at the Høvsøre site.

7

THE EFFECT OF BAROCLINICITY ON THE WIND IN THE PLANETARY BOUNDARY LAYER

Abstract

The role of baroclinity on the wind in the planetary boundary layer is investigated using two years of wind lidar measurements up to 950 m height from a suburban site in northern Germany (Hamburg) and a rural-coastal site in western Denmark (Høvsøre). The surface geostrophic wind, the gradient wind and the geostrophic wind are estimated using the pressure and geopotential fields from a mesoscale model. The atmospheric flow at both sites was typically baroclinic with the geostrophic wind shear near Gaussianly distributed with a mean close to zero and a standard deviation of ≈ 3 m s^{-1} km^{-1}. The thermal wind had a strong seasonal dependence because of temperature differences between land and sea. For easterly winds at Høvsøre the geostrophic wind was strongly decreasing with height, resulting in a mean low-level jet. Also in Hamburg the mean wind profile observed during an intensive radiosounding campaign and that from the wind lidar were influenced by baroclinity. The empirical constants in the geostrophic drag law for neutral conditions were strongly dependent on baroclinicity.

7.1 Introduction

The wind speed in the planetary boundary layer (PBL) is required for a wide range of applications such as numerical weather prediction (NWP), air pollution modelling and the wind energy industry. With the emergence of tall wind turbines operating above the surface layer, there has been an increased interest in the processes that determine the wind higher up in the PBL. Above the PBL the pressure gradient and Coriolis force are in equilibrium and the flow is geostrophic, but in the vicinity of horizontal temperature gradients caused by mesoscale weather systems, fronts or differential heating, the geostrophic wind is changing with height (baroclinity).

This chapter has been submitted as: Floors, R., Peña, A., and Gryning, S.-E. (2013a). The effect of baroclinicity on the wind in the planetary boundary layer. *Q. J. R. Meteorol. Soc.*, (submitted)

In many boundary-layer experiments and modelling studies the geostrophic wind is an important boundary condition. Because the geostrophic wind varies relatively little with horizontal distance (it can be constant within tens of kilometers) and is independent of microscale features of the flow, it can be used to relate wind observations that are made in a region with similar synoptic conditions by using the geostrophic drag law (Blackadar and Tennekes, 1968) as performed in the Wind Atlas Analysis and Application Program (WAsP). Zilitinkevich and Esau (2005) showed that part of the scatter in the empirical coefficients in the geostrophic drag law is caused by baroclinity. Also in single-column models in NWP models a wrong prediction of the change of the geostrophic wind with height can have a large impact on the representation of the wind profile. Baas et al. (2010) varied the geostrophic wind speed and geostrophic vertical wind shear that were used to force a single-column model and found that an ensemble of these forcings gave more realistic results when compared to observations.

The effect of baroclinity on the wind profile in the boundary layer was recognized a long time ago and the studies were often based on large-eddy simulation (LES) model outputs. For example, Brown (1996) compared the results from two first-order closure schemes with the model outputs from LES in neutral and unstable conditions and found that the performance of these schemes was not degraded by the presence of geostrophic shear. Sorbjan (2004) did more realistic simulations of the convective baroclinic boundary layer by taking into account the effect of temperature advection and the effect of baroclinity on the inversion layer. Both studies found that the first and second-order moments of wind and temperature in the PBL were influenced by baroclinity.

However, there are few experimental studies on the effect of baroclinity on the flow in the PBL, because measurements of horizontal temperature gradients are rarely available. One of the few studies that measured horizontal temperature gradients was done by Lenschow et al. (1980), who investigated the turbulent quantities of the baroclinic convective PBL. Another reason for the lack of experimental results of the baroclinic PBL is that there are many simultaneously varying parameters that influence the wind in the upper part of the boundary layer and so it is difficult to isolate the effect baroclinity. Still, Hoxit (1974) and Joffre (1982) averaged the results of many radiosondes to study basic features of the baroclinic PBL and found that there was a strong effect on the change of wind direction with height. Arya and Wyngaard (1975) studied the effect of baroclinity on the geostrophic drag law, but experimental verification of their model was difficult.

There are two new developments that are employed in this study to advance the understanding of the effects of baroclinity on the winds in the PBL. Firstly, wind lidars have recently improved in accuracy and range and can continuously provide measured wind speed profiles up to heights of ≈ 1000 m (Floors et al., 2013b). Secondly, more detailed knowledge about horizontal temperature gradients can nowadays be obtained from mesoscale model output.

In this study, we use data from a wind lidar that was measuring for 1 year at a

coastal site in Denmark and for 1 year at a suburban site in Hamburg. At both sites a meteorological mast is available to provide mean wind speeds and turbulence statistics. In addition, radiosondes that were launched during an intensive campaign are used. The Weather Research and Forecasting (WRF) mesoscale model can accurately describe wind and temperature fields up to a scale of a few kilometres (Hu et al., 2010; Xie et al., 2012; Gryning et al., 2013b). Combining the novel wind lidar measurements with the large-scale parameters estimated from mesoscale model output can give a comprehensive overview of the role of baroclinity on winds in the PBL.

First an overview of the flow in the baroclinic PBL is given in Section 7.2. The description of the sites and the data processing are presented in Section 7.3.1. In Section 7.3.2 we present a method to estimate the gestrophic wind and wind shear based on mesoscale model output. The impact of baroclinity on the wind speed climatologies of both sites is investigated in Section 7.4.1. Then, we study the influence of baroclinity on the wind profile in the PBL using the wind profile measurements from the wind lidar and the radiosondes. The effect of baroclinity on the wind veer in the PBL and on the constants in the geostrophic drag law is discussed in Section 7.4.3. Finally we present concluding remarks in Section 7.5.

7.2 Theory

Using Reynolds decomposition, in a cartesian coordinate system the wind can be decomposed in the mean U, V and W and their correspondent turbulent part u', v' and w'. In the geographic coordinate system x corresponds to the east-west direction, y to the north-south direction and z to the height above the surface. Assuming a horizontally homogeneous, stationary flow where the mean vertical velocity is zero, the equations of motion in the PBL are given by a balance between the friction force, the pressure gradient force and the Coriolis force,

$$\frac{\partial}{\partial z}\overline{u'w'} = f(V - V_g), \tag{7.1}$$

$$\frac{\partial}{\partial z}\overline{v'w'} = f(U_g - U), \tag{7.2}$$

where f is the Coriolis parameter and U_g and V_g are the geostrophic wind speed components,

$$U_g = -1/(f\rho_0)\partial P/\partial y, \tag{7.3}$$

$$V_g = 1/(f\rho_0)\partial P/\partial x, \tag{7.4}$$

where ρ_0 is the background air density and P is the atmospheric pressure. It is convenient to analyze the wind profile in a coordinate system that is aligned with the wind direction

at the surface. From now on we use the capital letters U and V to denote a wind speed in a geographic coordinate system and the letters u and v for the components that are aligned and perpendicular with respect to the surface wind.

The geostrophic flow is parallel to the isobars with the low pressure to the left on the Northern hemisphere because there is no friction above the PBL height and therefore an equilibrium exists between the pressure gradient and the Coriolis force. If the pressure gradient is measured at the surface or if it is reduced to the pressure at mean sea level, it is denoted as the surface geostrophic wind with components U_{g0} and V_{g0}. In barotropic conditions, the geostrophic wind at any height is equal to the surface geostrophic wind, i.e. $\mathbf{U}_g = \mathbf{U}_{g0}$. When horizontal temperature gradients are present, the atmosphere becomes baroclinic and $\mathbf{U}_g$ changes with height. The vector difference between the geostrophic wind at two heights is referred to as the thermal wind, which can be expressed in terms of a horizontal gradient of the geopotential difference between two layers (Holton and Hakim, 2004),

$$U_T = -\frac{1}{f}\frac{\partial(\Phi_z - \Phi_0)}{\partial y}, \tag{7.5}$$

$$V_T = \frac{1}{f}\frac{\partial(\Phi_z - \Phi_0)}{\partial x}, \tag{7.6}$$

where Φ_z and Φ_0 are the geopotentials at the top and at the bottom of the layer, respectively. The thermal wind vector is parallel to the isotherms with the cold air to the left. To introduce the terminology that is used in previous work on baroclinic effects in the PBL (Hoxit, 1974) and adopted in this paper, Figures 7.1a and 7.1b show a vector plot and the wind speed profile for a situation with positive geostrophic wind shear and veer. β is defined as the angle measured clockwise between $\mathbf{U}_{g0}$ and $\mathbf{U}_T$ at the PBL height h. When $0^\circ < \beta < 180^\circ$ there is warm air advection and when $180^\circ < \beta < 360^\circ$ there is cold air advection. The angle α measured clockwise between the surface wind vector $\mathbf{U}_0$ and $\mathbf{U}_{g0}$ is $\approx 20^\circ$ in a neutral PBL at mid-latitudes due to the effect of friction near the surface (Hess and Garratt, 2002a). ϕ is the angle between $\mathbf{U}_0$ and $\mathbf{U}_g$ at a certain height.

Eqs. (7.1) and (7.2) are the starting point for the derivation of the geostrophic drag law. Blackadar and Tennekes (1968) showed that in barotropic conditions u_g/u_* is given by a logarithmic function and v_g/u_* is equal to a constant, where u_* is the friction velocity. Combining the two components u_g and v_g results in a relation between the magnitude of the geostrophic wind $G = \sqrt{u_g^2 + v_g^2}$, $\alpha = \arctan(v_g/u_g)$, the roughness length z_0, u_* and the two integration constants A and B which can be written as,

$$A = \ln\left(\frac{u_*}{f z_0}\right) - (\kappa G/u_*)\cos\alpha, \tag{7.7}$$

$$B = \pm\kappa G/u_* \sin\alpha, \tag{7.8}$$

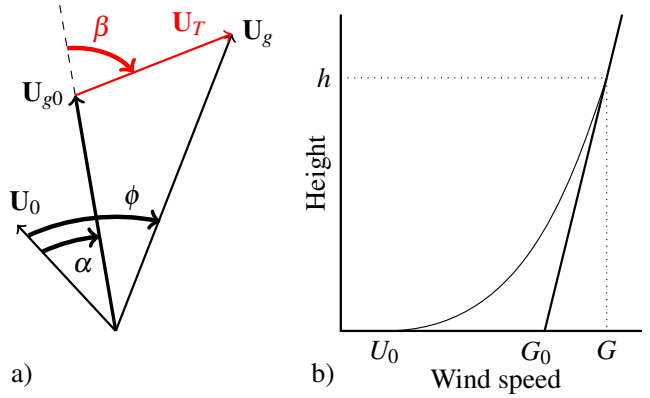

Figure 7.1: Behaviour of the wind vector looking downwards on the PBL in baroclinic conditions (left panel) and the wind profile in a situation with positive geostrophic shear (right panel). $\mathbf{U_0}$, $\mathbf{U_{g0}}$ and $\mathbf{U_g}$ denote the vectors of the surface layer wind, the surface geostropic wind and the geostrophic wind at the PBL height (h), respectively. U_0, G_0 and G denote the magnitude of these vectors. α and ϕ denote the angle between $\mathbf{U_0}$ and $\mathbf{U_{g0}}$ and between $\mathbf{U_0}$ and $\mathbf{U_g}$, respectively.

where $\kappa \approx 0.4$ and on the right hand side of Eq. (7.8) a minus is applied for the Northern Hemisphere and plus is applied for the Southern Hemisphere. Even in neutral and barotropic conditions the scatter in the constants A and B is very large when determined from experimental data, which is attributed to violations of the assumptions in Eqs. (7.1) and (7.2). An extensive overview of the numerous field experiments aimed at determining A and B for the neutral, barotropic case is given in Hess and Garratt (2002a,b). Zilitinkevich (1975) and Zilitinkevich and Esau (2005) showed that in non-neutral, non-barotropic conditions the internal stability parameter, baroclinicity and the free-flow stability are factors that influence the functional shape of A and B. When these factors were taken into account in a new formulation of A and B, LES simulations agreed better with the geostrophic drag law.

7.3 Methodology

7.3.1 Measurements

For this study a new long-range wind lidar (WLS70) from the company Leosphere was used, which was operating from 23 April 2010 to 29 March 2011 at a site in Denmark (Høvsøre). Then the wind lidar was moved to a site in Hamburg, where it was operating from 4 April 2011 to 24 March 2012. In Hamburg, the wind lidar had problems with the

cooling after the 13th of June and was then replaced by a similar device. At the 25th of November the lidar was repaired and the original device was reinstalled and measured until the 23rd of March 2012.

The wind lidar measured the wind speed and the wind direction every 50 m from 100 m up to a maximum of 2 km height depending on the aerosol content of the atmosphere. The radial wind speed was retrieved at four positions that are scanned with a laser. These four positions are separated 90° in a horizontal plane and the inclination angle of the beam relative to the zenith is 15°. From the four radial wind speeds the three dimensional wind vector can be constructed assuming horizontal homogeneity of the wind field. One 360° full scan (rotation) is performed every 30 s. The next sections describe the two sites where the wind lidar was operating and how the data were processed.

Høvsøre

The first experimental site is the National Test Station of Wind Turbines at Høvsøre in the west of Denmark (56° 26' 00" N 8° 09' 00" E, figure 7.2). The wind lidar was placed 10 m west of a 116.5 m high meteorological mast. The terrain around the site consists of grasslands and the North Sea located ≈ 1.7 km to the west. With westerly winds the flow at the site is influenced by the internal boundary layer that forms after the smooth-to-rough surface change at the shoreline of Denmark (Floors et al., 2011b). The wind speed is measured with Risø cup anemometers on booms mounted on the southern side of the mast at heights of 10, 40, 60, 80 and 100 m. The wind direction was measured at the same booms at 10, 60 and 100 m. The turbulent fluxes are measured with METEK Scientific USA-1 sonic anemometers at 10 m on booms directed to the north. The 20 Hz signal was retrieved and processed with the ECPACK software (Van Dijk et al., 2004). Spikes in the raw data signal were removed with a despiking algorithm (Højstrup, 1993). When using the eddy-covariance method it is common to perform a coordinate rotation to align the mean wind vector with the mean stress vector. Here, the planar-fit method was used (Wilczak et al., 2001), where a global rotation matrix is calculated based on the mean wind vectors of all 10-minute runs in one month. The resulting tilt angles were then used to rotate all 10-minute runs in the direction of the mean streamlines and an additional rotation was performed such that the mean transverse wind component was zero. After linearly detrending the timeseries, the along-wind ($\overline{u'w'}$) and transversal ($\overline{v'w'}$) kinematic stress can be obtained. Similarly, the kinematic heat flux $\overline{w'\theta'}$ can be obtained using fluctuations in the potential temperature θ. A cross-wind correction was applied for the kinematic heat flux (Schotanus et al., 1983). The friction velocity u_* was then calculated as $u_* = (\overline{u'w'}^2 + \overline{v'w'}^2)^{1/4}$. It is assumed that u_* and $\overline{w'\theta'}$ at 10 m are representative for their surface-layer values u_{*0} and $\overline{w'\theta'}_0$, respectively. The Obukhov length L was then calculated as,

$$L = -\frac{{u_{*0}}^3}{\kappa(g/T_0)(\overline{w'\theta'_v})_0}. \tag{7.9}$$

where g/T_0 is the buoyancy parameter that was obtained using the temperature at 2 m.

For the westerly flow there is no horizontal homogeneity and for northerly flow there is influence of the wakes from the mast and the wind turbines and therefore only data from the easterly sector were used. The wind direction for the easterly sector ranged between 30°–140°. The roughness length for this sector was determined by assuming a logarithmic wind profile for the data where $|L| > 1000$ m and inserting the measured u_* and wind speed at 10 m gave $z_0 = 0.03$ m. Wind profiles up to 950 m height were selected where the sonic anemometer at 10 m was available concurrently with wind speeds from the cup anemometers from 10–100 m and from the wind lidar from 100–950 m. The wind profiles from the lidar were rotated such that the wind direction at 100 m was the same as measured by the wind vane. In addition, the composite wind profiles were rotated such that they were aligned with the surface-layer wind direction to obtain the components u and v. Furthermore, all individual lidar scans in a 10-minute period had to have a carrier-to-noise ratio CNR> -35 dB and a mean CNR> -22 dB. The threshold of -22 dB was chosen based on agreement checks between the lidar and the cup anemometer at 100 m. Lastly, to exclude unsteady, weak-wind or sea-breeze conditions, the data where $G < 5$ m s^{-1} at 966 m (the tenth model level, see section 7.3.2) were excluded. In conditions with a geostrophic wind higher than 5 m s^{-1} it is unlikely that a sea-breeze circulation develops (Tijm et al., 1999).

The number of 10-min averaged profiles available for further analysis is given in Table 7.1. The agreement between the wind speed measured by the cup U_c and the wind speed measured by the wind lidar U_l at 100 m was very high with a squared Pearson correlation coefficient $r^2 = (\mathrm{cov}(U_c, U_l)/\sigma_{U_c}\sigma_{U_l})^2 = 0.99$ and a mean bias $b = 1/N\sum_{i=1}^{n}(U_{li} - U_{ci}) = -0.34$ m s^{-1} (-3.6%). Further information about the agreement between wind speed and wind direction of the mast and the wind lidar can be found in Peña et al. (2013). A CL31 ceilometer from the company Väisälä was operating at the site and used to estimate the PBL height h. An exponent idealized profile method was used to obtain the PBL height (Steyn et al., 1999; Hannesdóttir, 2013).

Hamburg

The wind lidar in Hamburg was installed 10 m west of a 12 m high meteorological mast, 170 m to the north-east of a television tower of 300 m height and 8 km south-east of downtown Hamburg (53° 31' 11,7" N, 10° 06' 18,5" E, Figure 7.2). The television tower has booms mounted on the southern side, where the wind speed, wind direction and turbulent quantities were measured with METEK Scientific USA-1 sonic anemometers at 50, 110, 175 and 250 m. To prevent any effects from the wake of mast, data from the northerly sector ranging from 320°–40° were filtered.

The momentum and heat flux were obtained in the same way as at Høvsøre. Because the area around the meteorological mast has several obstacles, only observations from the radio tower were used. The turbulent quantities derived from the sonic anemometer

at 50 m from the radio tower were assumed to be in the surface layer. For wind directions between 130°–320° the upstream area is the heavily build-up area of the city center of Hamburg and for wind directions between 40°– 130° the upstream area is a residential area with a combination of fields, trees and buildings. The roughness length for each sector was computed from the measured wind speed and the friction velocity at 50 m with the logarithmic wind profile using the mast data where $|L| > 1000$ m. This gave $z_0 \approx 0.52$ m for the built-up sector and $z_0 \approx 0.39$ m for the rural sector.

The wind lidar profiles were rotated such that the wind direction at 250 m agreed with the wind direction measured by the sonic anemometer at 250 m. Apart from this the wind lidar data were filtered in the same way as at the Høvsøre site, resulting in the number of profiles given in Table 7.1. A lidar ceilometer CL51 from Vaisala measured atmospheric backscatter profiles, of which h was derived using the algorithm described in Münkel et al. (2011).

The mean wind speed was measured with sonic anemometers and because the television tower is rather bulky it distorts the flow around the instrumentation. In addition, the radio tower and the wind lidar were located 170 m away from each other, which increases the scatter between the measured wind speeds of both instruments due to spatial differences. Still, the combined timeseries of the two different wind lidars and the sonic anemometer at the radio tower showed good agreement for the wind speeds at a height of 250 m, with $r^2 = 0.96$ and $b = -0.19$ m s^{-1} (-1.9 %).

In addition to the mast and lidar measurements, two intensive measurement campaigns were performed in Hamburg during two five-day periods in 2011. The first campaign was started at 0800 UTC, 15 June 2011 at and ended at 0800 UTC, 20 June 2011. During this period 60 radiosondes were released, i.e. approximately one sounding in every two hours. Two radiosondes did not reach up to five km height and were therefore not used. A second intensive campaign was performed from 0800 UTC, 4 October 2011 until 0700 UTC, 9 October 2011. Also during this period radiosondes were released every two hours, except for the last day when a sounding was released every hour. A total of 74 radiosondes was released, all of which reached up to 5 km height.

The measurements from the radiosondes were cut into 50 m intervals to compare them with the lidar and mast data. For example, the mean wind speed at 250 m was computed by averaging all samples taken between 225 and 275 m. Despite the fact that radiosondes do not measure in 10-min means as the sonic anemometer, the wind speeds obtained from the 112 radiosondes agreed fairly well with the mast data at 250 m, $r^2 = 0.84$ and $b = -0.18$ m s^{-1} (-1.8 %). To evaluate the accuracy of the wind lidar at high heights it was compared to the wind speed from the radiosondes at 950 m, but due to the filtering criteria the number of profiles that could be compared was limited to 20. Also at this height the agreement was good, $r^2 = 0.79$ and $b = -0.21$ m s^{-1} (-1.3 %).

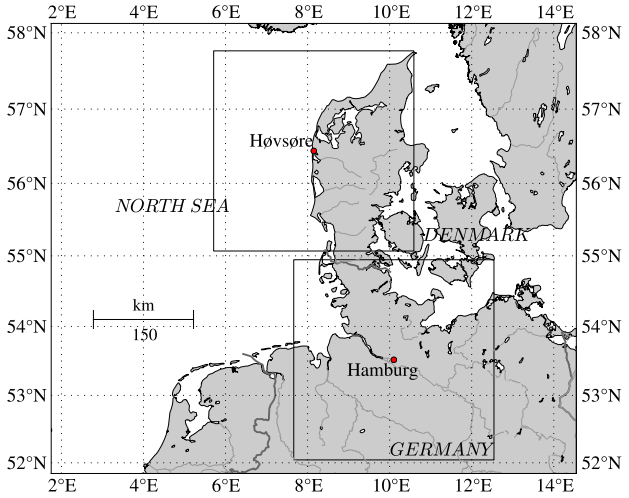

Figure 7.2: Map of the North Sea area. The black squares indicate the areas in which the pressure and geopotential gradients were derived.

Table 7.1: Number of profiles N and the percentage of all the 10-min intervals that is available after applying the filtering (see correspondent text).

	Høvsøre		Hamburg	
Data set	N	Perc.	N	Perc.
WRF	50256	100	51840	100
WRF, mast	12853	26	46474	90
WRF, mast, lidar	528	1.1	2641	5.1
WRF, mast, soundings	-	-	112	0.22

7.3.2 Estimation of the atmospheric forcing

In previous works on baroclinity, the variation of geostrophic wind with height was often estimated from the gradient of the geostrophic wind speed at or near the top of the PBL (Joffre, 1982; Garratt, 1985). However, in unstable conditions the strongest wind shear is largely displaced to the entrainment zone by turbulent mixing, resulting in uncertain estimations of geostrophic shear. Furthermore, the PBL height itself is inherently uncertain (Seibert et al., 2000).

Here, we therefore used a mesoscale model to estimate the geostrophic wind, the thermal wind and the PBL height. The Advanced Research WRF (ARW) model version 3.4 (hereafter the WRF model) was used, which is a mesoscale model developed by the National Center of Atmospheric Research (NCAR) that uses state-of-the-art numerical schemes (Skamarock et al., 2005). The following physical parametrization schemes are used:

- Yonsei University PBL scheme (Hong et al., 2006)
- NOAH land-surface scheme (Chen and Dudhia, 2001)
- Thompson microphysics scheme (Thompson et al., 2004).
- RRTM longwave radiation (Mlawer et al., 1997)
- Dudhia shortwave radiation (Dudhia, 1989)

A coding error that gave too much mixing for stable conditions in the YSU scheme in previous versions of WRF was removed. The model was run from April 2010 until April 2011 for Høvsøre and for April 2011 until April 2012 for Hamburg in analysis mode, viz. it was started every 10 days at 00 UTC for a period of 264 hours. There were two model domains that used two-way nesting and had a horizontal resolution of 18 and 6 km. After removing the first 24 hours of spin-up time, 10-minute instantaneous model output from the innermost domain was used. The outer and inner model domains had a timestep of 120 and 40 s, respectively. The boundary and initial conditions came from the NCEP FNL analysis and from the NCEP real-time global sea-surface temperature analysis. Nudging towards the atmospheric analysis data of the specific humidity, the potential temperature and U and V, was applied in the outermost domain above the 10th model level (which corresponds to a height of $\sim$ 1400 m). The set-up of the WRF model described above was successfully used to estimate the profiles of the wind speed Weibull-distribution parameters at Høvsøre (Gryning et al., 2013a,b).

The described set-up was chosen based on several sensitivity studies: a one month period in autumn 2010 was modelled using two vertical resolutions, two roughness descriptions, two analysis forcings and two PBL schemes. Varying these parameters had an impact on the representation of the wind profile, but none of the set-ups simulated wind speeds significantly better than any of the others (Floors et al., 2013b). Because

of the rather long simulation period, it was finally chosen to use the relatively fast first-order YSU PBL scheme and the lower resolution. The FNL were chosen based on its real-time availability which allowed to start the analysis when the data were available. Nudging of simulations was shown to improve the representation of the wind speed Weibull-distribution parameters at Høvsøre (Gryning et al., 2013a).

The gradients of geopotential and pressure were estimated from model output in a square around the sites (see figure 7.2). The size of this square was chosen such that it was sufficiently large to determine the radius of curvature of typical mid-latitude atmospheric systems ($\sim$ 1000 km), but also that it was so small that the derived gradients actually represent the geostrophic flow at the point of interest. Gradients were calculated for a number of square grids between 36–360 km and finally a value of 300 km was chosen based on good agreement between the estimated geostrophic wind and the measurements at 950 m.

The geostrophic wind was estimated by using linear regression between the north-south and east-west grid distance and mean sea-level pressure field obtained from the model output. A similar procedure was performed to obtain the gradient in the geopotential difference (Eqs. (7.5) and (7.6)). The geopotential difference between a certain model level and the first model level was calculated for each level using linear regression.

When the pressure gradient is estimated over some finite area, one has to assume that the pressure field varies linearly with x and y. However, when there is a cyclonic or anti-cyclonic flow, the second derivatives of the pressure field will not be zero, i.e. the isobars cannot be considered to be straight. The radius of curvature R of the isobars is positive around a low pressure system and negative around a high pressure system. When the isobars are curved, the centrifugal acceleration becomes important and the magnitude of the wind speed aloft is equal to the magnitude of the gradient wind G_{gr}. The flow is then described by a balance between the centrifugal force, the Coriolis force and the pressure force (Kristensen and Jensen, 1999). When we assume $G = G_0$,

$$\frac{G_0}{fR}\left(\frac{G_{gr}}{G_0}\right)^2 + \frac{G_{gr}}{G_0} - 1 = 0. \tag{7.10}$$

Eq. (7.10) is a quadratic equation and can be solved for G_{gr}/G_0, when the radius of curvature is known. Kristensen and Jensen (1999) assumed that the pressure field in a certain area can be described by the surface,

$$p(x,y) = p_0 + p_x + p_y + 0.5(p_{xx}^2 + 2p_{xy} + p_{yy}^2), \tag{7.11}$$

where p_0 is a reference pressure and a subscript denotes first (one letter) and second derivatives (two letters) with respect to the differentiated dimension. From this field the curvature can be estimated by,

$$R = \frac{(p_x^2 + p_y^2)^{3/2}}{p_{yy}p_x^2 - 2p_{xy}p_xp_y + p_{xx}p_y^2}. \tag{7.12}$$

The algorithm described in Shary (1995) was used to estimate all derivatives for a set of 3 by 3 grid points. A curvature was then computed for all grid points and spatially averaged over the 300 km squares surrounding the site. Assuming that the direction of the surface geostrophic wind and the gradient wind were the same, the components of the gradient wind, U_{gr} and V_{gr}, were estimated. Furthermore, it was assumed that the curvature of the pressure field was constant with height and that the contribution of the thermal wind to the estimation of the gradient wind was negligible. The geostrophic wind vector at a given height z was then expressed as the vector sum of the gradient wind and the thermal wind, i.e. $U_g = U_{gr} + U_T$ and $V_g = V_{gr} + V_T$.

7.4 Results

7.4.1 A climatology of baroclinicity

Because quantitative descriptions of the geostrophic wind shear are rare, the distributions of the thermal wind at a certain height from the WRF simulations are interesting to illustrate the effect of the thermal wind. A histogram of the derived thermal wind speed components in the west-east (U_T) and north-south (V_T) directions is shown for the tenth model level, corresponding to a height of 966 m for Høvsøre and 976 m for Hamburg (Figure 7.3). Because filtering of the wind lidar profiles produces a data set which is different from that showing the climatological mean, both histograms from all simulated thermal winds from the WRF model and those that occurred simultaneously with the filtered mast and lidar profiles are shown. The frequency of occurrence in each bin is normalized by the total amount of available 10-minute profiles (table 7.1).

The U_T component of the thermal wind depends on the north-south temperature gradient: from Eq. (7.5) it follows that a positive U_T is caused by a geopotential difference that is decreasing towards the north. This situation corresponds to the mean climatological state of the atmosphere at mid-latitudes, because it is usually colder in the north. V_T is related the east-west temperature gradient and is positive for a temperature that is increasing towards the east. In figure 7.3, V_T at Høvsøre is on average negative, which corresponds to a situation where it is colder in the East. In the filtered data V_T becomes significantly more negative: this is because the filtered data are from the easterly sector which contained many profiles from the period between February and March, when the temperature was very low over the snow-covered land but higher over sea. In Hamburg the sector that is used for filtering the profiles is larger than at Høvsøre, and therefore the distribution of the filtered data is similar to the yearly distribution.

In Figure 7.3 the large spread in thermal winds is evident, which sometimes has the same order of magnitude as the mean gradient wind at both locations, $G_{gr} \approx 11.7$ m s^{-1} at Høvsøre and $Ggr \approx 11.2$ m s^{-1} in Hamburg. At Høvsøre the distribution of land and sea in the square that was used to derive the pressure and temperature gradients is oriented north-south (Fig. 7.2), so one expects V_T to be largely affected by tempera-

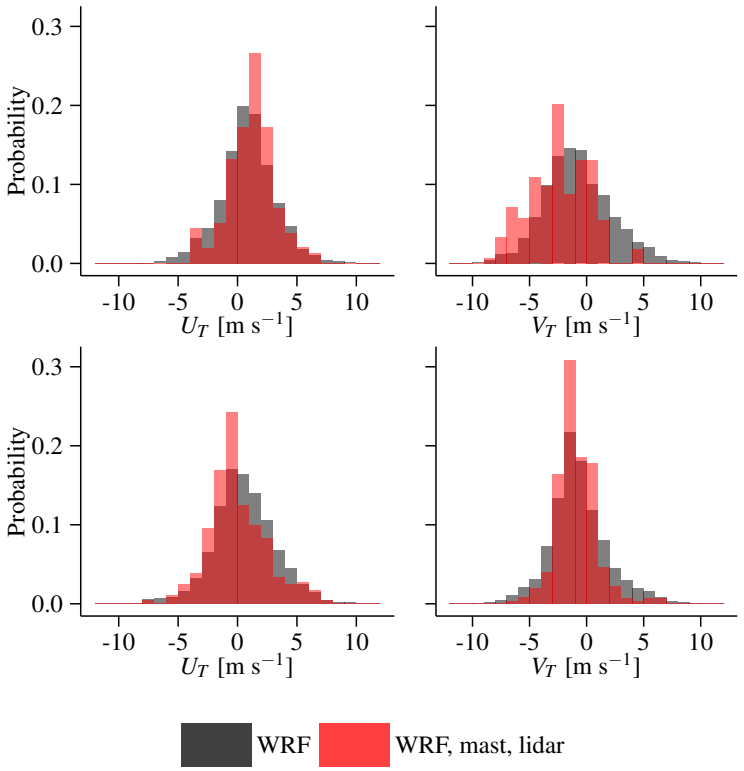

Figure 7.3: Probability histrogram of U_T and V_T from the surface up to ≈970 m for April 2010 until April 2011 at Høvsøre (top) and for April 2011 until April 2012 in Hamburg (bottom). The black histograms represent all 10-minute values derived from the model simulations and the red histograms represent the model-derived values where concurrent measurements from the wind lidar and the mast were available. The number of corresponding profiles for the WRF simulations and for the filtered dataset are given in Table 7.1.

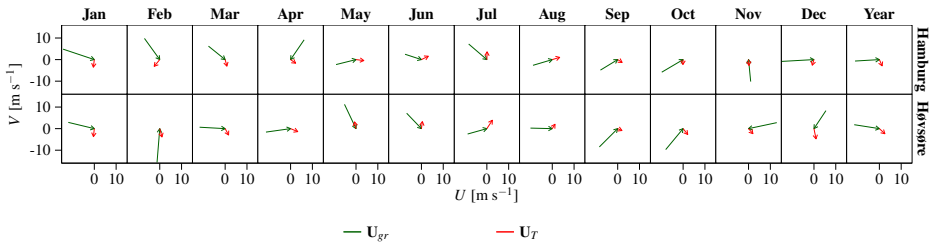

Figure 7.4: The monthly and yearly means of the gradient and thermal wind vectors up to 976 m at Hamburg (top) and up to 966 m at Høvsøre (bottom).

ture contrasts between sea and land. Indeed, the distribution of V_T is slightly wider at Høvsøre than in Hamburg in Figure 7.3. In Hamburg the distribution of land and sea in the square is oriented more east-west and therefore the distribution of U_T is slightly wider than at Høvsøre. This can be more easily seen by calculating the standard deviation of the thermal wind components, which gives $\sigma_{U_T} = 2.4$ m s^{-1} and $\sigma_{V_T} = 3$ m s^{-1} at Høvsøre and $\sigma_{U_T} = 2.6$ m s^{-1} and $\sigma_{V_T} = 2.6$ m s^{-1} in Hamburg. The thermal wind values are generally consistent with the values of geostrophic wind shear ($U_T/\Delta z$ and $V_T/\Delta z$) that were found in previous experiments. Garratt (1985) used observations in northern Australia to estimate the geostrophic shear and found that the thermal wind components ranged from 0–6 m s^{-1} km^{-1}. Joffre (1982) used pilot-balloon observations that were launched on an island in the Baltic on a latitude similar to our study and found values of 0–4 m s^{-1} km^{-1}.

To investigate whether the sea-land distribution is in fact responsible for the large variation in geostrophic wind shear, we study the yearly cycle of the thermal and gradient winds. In winter the land is generally colder than the sea, because the days are short and there is little shortwave radiation from the sun to heat up the surface, while in the summer the situation is the opposite. The sea generally has a much slower response to the input of radiation due to its high specific heat capacity. In Figure 7.4 the mean vectors $\mathbf{U}_{gr}$ and $\mathbf{U}_T$ are shown for each month and for the whole year.

At both sites in most months the surface gradient wind is from westerly directions and approximately 10–15 m s^{-1}. The yearly mean wind direction is westerly for Hamburg and slightly more northwesterly for Høvsøre. This in accordance with the multi-year mean wind rose found for similar latitudes in Denmark and the Netherlands by Sathe et al. (2011). There is a strong yearly cycle in the direction of the thermal wind vector. At both sites the thermal wind is directed towards the south from December to March, corresponding to a situation when the continent is cold and the North Sea relatively mild. During June to August the thermal wind vector is usually pointing to the northeast, which corresponds to a situation where the warmest air is to the southeast.

7.4.2 Estimations of the geostrophic wind

In this section, we present profiles of the u, v and U components and vector plots to see the effect of geostrophic shear on the observations from the radiosondes and the lidar. Furthermore, the method to estimate $\mathbf{U}_{gr}$ is validated, which can be achieved by comparing the geostrophic wind estimations with wind measurements above the PBL. The estimation of the geostrophic wind does not include the effect of local accelerations, decelerations or advection and therefore Eqs. (7.1) and (7.2) are applicable, but in the observation these effects will be present. If we use a sufficiently large amount of observations, we assume that most of these effects will cancel out because the long-term mean acceleration or advection is ≈ 0.

The measuring height of the wind lidar is limited by the aerosol content of the atmosphere and the strength of the lidar signal, while the radiosondes can measure the wind speed much higher than the PBL height. Therefore, the estimated geostrophic wind is first compared with the wind speeds from the radio sondes for the two intensive campaigns. In Figure 7.5 all 10-minute mean observed wind profiles and simulated geostrophic wind profiles were rotated such that u and v are the wind speed components aligned and perpendicular to the surface-layer wind.

The mean wind vector plot (Fig. 7.5, panel 1a) shows that the wind veers $\approx 25^{\circ}$ with height due to the effect of friction near the surface. At 950 m it approaches the geostrophic wind and the gradient winds. The maximum PBL height is indicated in panels 1b–1d and was derived from the WRF simulations. It indicates the height at which frictional effects are not expected and where the geostrophic and observed wind speeds should be approximately the same. The estimated PBL height from the ceilometer was not used here because the number of available profiles was then significantly reduced. It can be seen in panel 1a that both the mean $\mathbf{U}_g$ and $\mathbf{U}_{gr}$ are in fair agreement with the mean observed wind vector around 950 m.

In panel 1c the v component of the geostrophic wind increases with height up to ≈ 1100 m and then decreases with height, which shows a better agreement compared to the observations than the surface geostrophic wind or the gradient wind. The magnitude of the geostrophic wind increases strongly with height (panel 1d), particularly above the mean PBL height and it is nearly 3 m s^{-1} higher than G_{gr} at 4000 m. Because the wind was on average from the west in the intensive campaigns, this corresponds to a situation where the temperature is decreasing towards the north. The gradient wind speed is slightly lower than the surface geostrophic wind, because there was on average a positive curvature corresponding to a cyclonic pressure field during the intensive campaigns.

In row 2 of Figure 7.5 the mean vectors and wind profiles from the wind lidar in Hamburg that were available up to 950 m height are shown. When the observed PBL height is higher than 950 m it is possible that there is still significant friction at 950 m and therefore the wind speed from the wind lidar is lower than the geostrophic wind. To ensure that the wind speed at the top of the panel approximately corresponds to a geostrophic wind speed, we include only the profiles where the simulated PBL height

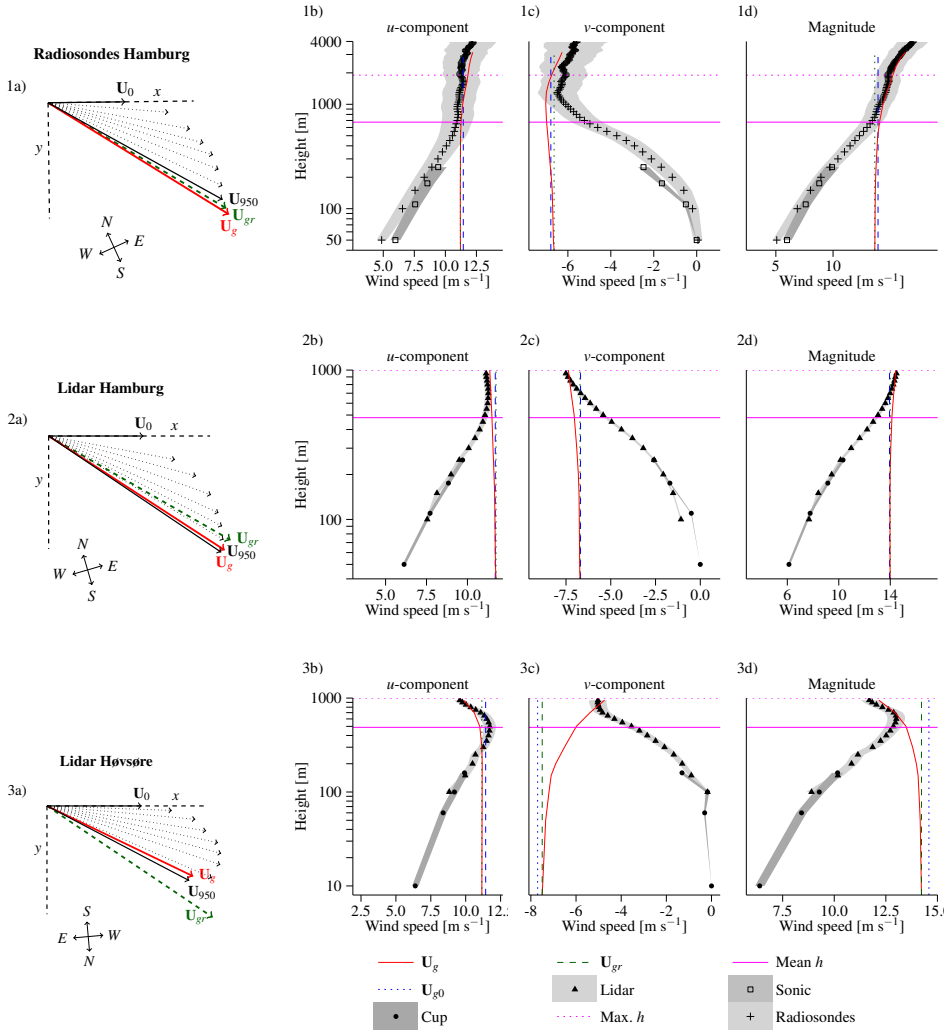

Figure 7.5: Panel a) shows the mean observed wind vectors from surface-layer up to 950 m in a coordinate system aligned with the surface wind $\mathbf{U}_0$ (i.e. the u-component is on the x-axis). The gradient wind (green dotted line) and the geostrophic wind (red line) are shown and a compass rose is indicated. The panels b)–d) show the profiles of the u and v components and the magnitude of the wind speed. The shaded areas denote the standard error of mean from the observations, $\pm\sigma/\sqrt{N}$. The mean and maximum height of the modelled PBL height from the WRF simulations are indicated with a pink solid line and a pink dotted line, respectively, and the surface geostrophic wind is denoted with a blue dotted line. The observations from the radiosondes launched during the intensive campaign (top panels), from the wind lidar in Hamburg (middle panels) and from the wind lidar for the easterly sector at Høvsøre (bottom panels) are shown.

from the WRF model is lower than 1000 m. Also the CNR limit that was used for filtering of the profiles is a good proxy for the mean PBL height (Floors et al., 2013b).

The gradient wind and the surface geostrophic wind both overpredict the u-component of the wind at 950 m, whereas by including the baroclinic components the estimated geostrophic wind becomes closer to the observations. The opposite is true for the v-component of the wind. The net effect on the magnitude of the wind speed is that G_g is closer to the observations, while G_0 and G_{gr} have lower values than observed at 950 m.

Finally in figure 7.5, panels 3a–3d the mean wind vectors and profiles for the easterly sector at Høvsøre are shown. The flow from the east is highly baroclinic with a strong decrease in both the u and v components and consequently also in the magnitude of the geostrophic wind with height. Because the mean wind direction is from the east, the temperature decrease from south to north decreases the geostrophic wind with height. Consequently, the wind speed is overestimated by the surface geostrophic and gradient winds, while the geostrophic wind is closer to the observations.

It is interesting to note that the mean u-component and the magnitude of the wind speed show a wind maximum at the mean PBL height around 500 m. This mean low-level jet was also observed in Floors et al. (2013b) for the easterly sector at the same site. By studying the distributions of baroclinic shear at Høvsøre and Hamburg, Fig. 7.3, it was observed that conditions with negative baroclinic shear occur more frequently when the wind direction is between south and east. In a study on the frequency of occurrence of low-level jets, Baas et al. (2009) found that low-level jets in the Netherlands most frequently occurred for the same sector. This indicates that the abundance of low-level jets for south-easterly winds are partly a consequence of baroclinity.

It is also important to determine the root mean-square error (RMSE) between the observations at a certain height near the top of the PBL and the estimations of $\mathbf{U}_{g0}$, $\mathbf{U}_{gr}$ or $\mathbf{U}_g$. Many authors used the surface pressure to estimate the geostrophic wind, but seldomly the effects of the thermal wind were taken into account (Kristensen and Jensen, 1999; Baas et al., 2009; Larsén and Mann, 2009). The root mean-square error (RMSE) between the the observed magnitude of the wind speed at 1000 m from the radiosondes and G_0, G_{gr} and G was calculated. This gave values of 3.39, 3.47 and 3.13 m s^{-1}, respectively. Calculating the RMSE of U_z at a height of 950 m from the wind lidar in Hamburg and G_0, G_{gr} and G gave values of 2.81, 2.77 and 2.39 m s^{-1}, respectively. The RMSE between U_z at 950 m at Høvsøre and G_0, G_{gr} and G was 4.94, 4.65 and 2.44 m s^{-1}, respectively. This shows that taking account the curvature of the isobars and the effect of thermal winds improves the estimation the geostrophic wind.

7.4.3 Integral PBL measures

Many studies have tried to experimentally determine the constants A and B of the geostrophic drag law, Eqs 7.7 and 7.8 in neutral and barotropic conditions as this is a simple way to estimate the geostrophic wind based on variables that can be observed near the sur-

face (Hess and Garratt, 2002a). However, it is not clear whether the atmosphere was barotropic in these experiments. We aim to determine A and B from the observations and show the dependency on the baroclinity parameter β. However, the coefficients A and B are dependent on other variables and it is therefore difficult to isolate these dependencies in experimental data. The effect of atmospheric stability is known to cause large scatter in the determination of the coefficients (Zilitinkevich, 1975) as well as the Brunt-Väisälä frequency (Zilitinkevich and Esau, 2002). Unfortunately measurements of the Brunt-Väisälä frequency were not available, but stability was observed by means of L and so we make use of neutrally stratified data only. It was assumed that the PBL was neutral when $|L| > 1000$ m and only those profiles were selected at both Hamburg and Høvsøre to estimate the contribution of baroclinity to the scatter in A and B.

To clearly discriminate the effect of baroclinity, ideally A and B should be determined from measured variables only. From Eqs. (7.7) and (7.8), u_* and z_0 are measured but G and α can only be obtained from the model output and are therefore inherently less accurate due to modelling errors. Therefore G and α were also estimated from the measured wind lidar profiles. It was assumed that the wind measured by the wind lidar at the PBL height was equal to the geostrophic wind, i.e. $\mathbf{U}_h = \mathbf{U}_g$. In the previous section the wind at larger heights is observed to be influenced by baroclinity, so assuming $\mathbf{U}_h = \mathbf{U}_g$ the angle ϕ is used instead of α and $G \neq G_0$ (Figure 7.1). Such an assumption is needed, since the contribution of baroclinity to the veering angle was usually not known. So α was computed as the angle between $\mathbf{U}_0$ and $\mathbf{U}_{gr}$ and ϕ was computed as the angle between $\mathbf{U}_0$ and $\mathbf{U}_h$. The PBL height was obtained from the ceilometer, which is rather uncertain apart from the fact that several definitions of the PBL height exist (Seibert et al., 2000). Therefore another method was also used to determine A and B which assumed that $\mathbf{U}_{950} = \mathbf{U}_{gr}$. The angle between $\mathbf{U}_0$ and $\mathbf{U}_{950}$ is defined as ϕ_{950}.

In Figure 7.6 the behaviour of the angles α and ϕ in Hamburg is shown. At Høvsøre there were few data available and these results are therefore not shown. For $0^\circ < \beta < 180^\circ$ the geostrophic wind is veering with height, i.e. away from the surface geostrophic wind, whereas for $180^\circ < \beta < 360^\circ$ the geostrophic wind is backing with height, i.e. towards the surface geostrophic wind. It can be seen that in the range between 45°–225° ϕ is usually the largest whereas for 225°–45° it is the lowest. The cross-isobaric angle shows the opposite behaviour, since the surface geostrophic wind has a larger angle with the surface wind when $180^\circ < \beta < 360^\circ$ (cf. panel 3a in Figure 7.5 where $\beta \approx 225^\circ$). This behaviour is similar to a study based on a long-term climatological data of the baroclinic boundary layer (e.g. Hoxit, 1974), although in their study α is slightly phase shifted to the left and the amplitude of the dependency on β is much larger. This can be due to the neutral conditions that where selected for this study; in Hoxit (1974) all stability conditions were included.

When $\mathbf{U}_{950} = \mathbf{U}_g$ was assumed, ϕ_{950} showed a similar dependency on β with slightly larger amplitude, but this might be due to wind veer that occurred above the PBL height; in Figure 7.5 it was seen that the mean PBL height was smaller than 950 m. In addition

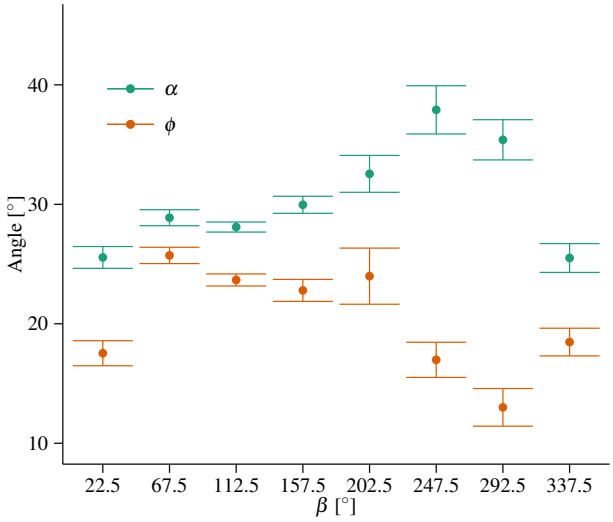

Figure 7.6: The mean of the observations of ϕ and α in Hamburg in neutral conditions separated according to 45° bins of β (Figure 7.1). The error bars denote the standard error of mean, $\pm\sigma/\sqrt{N}$.

Table 7.2: Mean of the parameters of the geostrophic drag law for all neutral profiles at Hamburg and Høvsøre using $\mathbf{U}_0$ and $\mathbf{U}_h$ to determine ϕ and the geostrophic wind, where the subscript h denotes the observed PBL height from the ceilometer.

Location	N	A	σ_A	B	σ_B	ϕ	h	u_{*0}	$\lvert\mathbf{U}_T\rvert$	$\lvert\mathbf{U}_h\rvert$
Hamburg	848	-0.05	2.47	3.89	2.45	21.74	690.48	0.72	1.78	18.04
Høvsøre	79	1.73	2.47	3.85	2.72	20.76	680.69	0.58	2.91	16.47

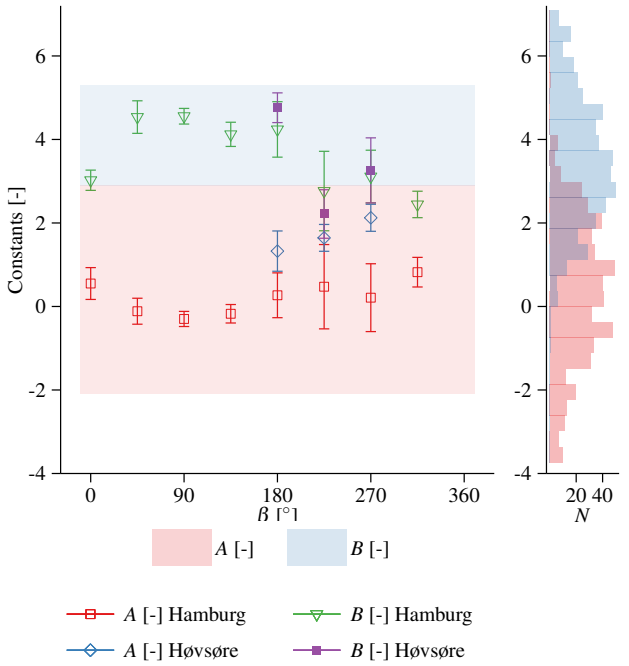

Figure 7.7: In the left panel the mean A and B versus 45° bins of the angle β for neutral profiles from Hamburg and Høvsore are shown. The error bars denote the standard error of the mean in each bin. The blue and red shaded areas correspond to the range of values that was summarized in (Hess and Garratt, 2002a). The right panel shows the binned distributions of the observed A and B in Hamburg.

the mean value of ϕ_{950} was slightly larger than ϕ, which can indicate that the PBL height from the ceilometer was underestimated or that the wind was still relaxing to its geostrophic value when $z > h$. This feature can also be observed in the mean wind profiles (Figure 7.5), where the u-component was nearly constant with height above the mean PBL height, whereas the v-component was still decreasing with height. Regardless of the used method, the geostrophic shear makes difficult the estimation of α as one measures ϕ or ϕ_{950} under baroclinic conditions.

In Figure 7.7 the integrations constant are shown as function of the geostrophic wind veer in the neutral PBL at Hamburg and Høvsøre. The mean values of B at Hamburg show a similar trend as ϕ in Figure 7.6, with a maximum around $\beta = 90°$ and minimum around $\beta = 270°$. The behaviour of A and B for the three bins where data were available at Høvsøre was similar to the values obtained in Hamburg, with a minimum around $\beta = 270°$. Note that at Høvsøre the available data lie in the range 180°–270°, corresponding well with $\beta \approx 225°$ in Figure 7.5, panel 3a, which shows that for the easterly sector negative geostrophic shears are common. The variation of A as a function of β is the opposite with a minimum around 90°.

Baroclinity is from our analysis a source of the variability observed in A and B in the overview of experiments given in Hess and Garratt (2002a). Also most of the related references state that during the experiments there were no accurate measurements of the thermal winds, (e.g. Clarke and Hess, 1974). The shaded area in Figure 7.7 shows the values of A and B that were found from many experiments at mid-latitudes from the seventies until the nineties (Hess and Garratt, 2002a). Generally they fall very well within the distribution of observed values of A and B in Hamburg (right panel). The systematic behaviour of the A and B coefficients with β shows that some of the variability in their estimates is caused by baroclinity.

In Table 7.2 several mean variables of the observed neutral and baroclinic boundary layer are summarized. Hess and Garratt (2002a) concluded that a best estimate for the neutral, barotropic PBL was $A \approx 1.3$ and $B \approx 4.4$. These values are well within the range of values found here including all baroclinity conditions. Kristensen and Jensen (1999) did a similar study as the present work using atmospheric pressure observations to derive the geostrophic wind without accounting for baroclinity and found $A \approx 0.8$ and $B \approx 4.1$. They also reported the standard deviations σ_A and σ_B, which were 2.9 and 2.9, respectively. These values are slightly higher than those found here (Table 7.2). This indicates that even using very accurately measured wind speeds from a wind lidar the spread in A and B is still considerable.

7.5 Conclusions

The long-term influence of baroclinity on the structure of the PBL was investigated for a coastal site in Denmark and a urban site in Germany using two years of lidar measurements and radiosondes of a two week intensive campaign. A method for deriving the

surface geostrophic wind, the gradient wind and the variation of geostrophic wind with height was developed by using outputs from the mesoscale model WRF. The gradients of the pressure and temperature field were obtained from a 300 km square of the innermost model domain.

At both sites the atmosphere was often baroclinic. The north-south and east-west component of the geostrophic shear had approximately Gaussian distributions with a standard deviation of $\approx$3 m s^{-1} km^{-1} at both sites. The variation of the north-south component of geostrophic shear was slightly larger at Høvsøre, which was related to the distribution of land and sea in the grid box that was used to estimate the thermal wind. The thermal wind vector showed a strong seasonal dependence in both locations and was pointing southeastward during the winter months. This agrees with the climatological mean temperature gradient during winter with the coldest air to the northeast. During summer the thermal wind was on average directed towards the north corresponding with the highest temperatures towards the east.

The mean wind profiles measured by the wind lidar agreed well with the estimated surface geostrophic wind above the PBL height, but there was a lower bias and a lower RMSE between the measurements and the estimated geostrophic wind when the thermal wind was taken into account. During an intensive campaign the geostrophic wind was increasing with height, which was also observed for the yearly mean of the wind profiles in Hamburg. At Høvsøre, the wind aligned and perpendicular to the surface wind were decreasing and increasing with height, respectively. This led to a wind profile strongly decreasing in magnitude with height and therefore a jet formed with a wind speed maximum around 500 m. A baroclinic atmosphere with a suitable alignment of the gradient wind and the thermal wind can therefore generate frequent low-level jets.

The cross-isobaric angle, the observed wind veer up to 950 m and up to the PBL height were shown to be a function of the angle between the gradient and the thermal wind. The integration constants A and B from the geostrophic drag law where derived from the observations using the surface-layer observations and the wind at the PBL height. The mean values of A and B for the neutral PBL agreed well with earlier field experiments of the neutral barotropic boundary layer, regardless of the method that was used for their derivation. However, the values of the constants were strongly dependent on the angle between the gradient wind and the thermal wind.

Parametrizing the effects of the thermal wind can be useful for a more robust application of the geostrophic drag law. This work shows that combining large-scale parameters derived from mesoscale models with the wind lidar wind profiles provides a good basis for analysis of boundary-layer profiles. For future research other relevant parameters, such as the Brunt-Väisälä frequency, could be estimated from mesoscale model output. The method presented here is used in Peña et al. (2013) to provide modellers with wind and turbulence observations where the effects of stability and baroclinity are accurately estimated, which enables future modelling studies to better explain discrepancies between measurements and models.

Acknowledgements

The study is supported by the Danish Research Agency Strategic Research Council (Sagsnr. 2104-08-0025) “Tall wind” project and the Nordic Centre of Excellence programme CRAICC. The TEM section at DTU Wind Energy is acknowledged for maintenance of the data base for all measurements from the Høvsøre site.

8

SUMMARY AND OUTLOOK

8.1 Summary

This thesis aimed to enhance the understanding of behaviour of the flow at the scale of modern wind turbines. This was achieved by combining meteorological mast and wind lidar measurements reaching to the top of the PBL. The wind lidar measurements showed good agreement on the heights where the wind speeds were compared with the cup- and sonic anemometer data from the meteorological mast at Høvsøre and Hamburg.

At the coastal site Høvsøre, the flow changes abruptly after the smooth-to-rough surface roughness change associated with the shoreline. Using data from a mast upstream at sea, it was seen that atmospheric stability over sea has a large impact on the wind profile at Høvsøre, despite its distance of about 2 km inland. Over land the stability was mainly determined by the diurnal cycle; the logarithmic wind profile, corrected for stability using near-surface turbulence measurements, was able to predict the wind speed at hub-height well. Over sea, the stability was mainly determined by the difference between the air and the sea. For flow from the sea, extrapolation of the wind speeds to hub height with the stability-corrected logarithmic wind profile yielded poor results, because the stability and roughness over sea should to be taken into account.

In neutral conditions, the effect of the changing roughness on the wind profile can be modelled with a interpolation of the upstream and downstream logarithmic wind profile. The IBL height was calculated based on a diffusion analogy. Using observations of the friction velocity and the results of a numerical model, it was shown that the IBL height was lower than predicted by the old model. However, this too high IBL height is needed to use the relation between up and downstream friction velocity and roughness length. Slightly adjusting the constants in the interpolation scheme yielded good results when the model was compared with observations in neutral conditions and also when it was compared to the observed climatological mean wind profile that included non-neutral cases.

Data from the same meteorological mast were used to evaluate the WRF mesoscale model during a four week period in autumn 2010. In this period, the mast data were supplemented with data from a new wind lidar up to 800 m. The default roughness in the model was too high compared to the observed roughness at 10 and 40 m and therefore the model simulated a too high friction velocity. Adjusting this roughness reduced the positive bias in the friction velocity and the wind profiles several grid points inland were better represented.

However, a high negative bias of the model compared to the measurements was observed from 40–800 m for westerly winds and around 400 m for easterly winds. For easterly winds the negative bias mostly occurred during stable conditions when there was an underestimation of the amount of low-level jets, which where generally modelled with a too low wind-speed maximum and a position of the wind maximum that was too high. For westerly winds the observed bias could not be explained by local roughness or stability conditions and therefore a set of sensitivity experiments was done. Two boundary-layer schemes were used, the 1.5-order MYNN scheme and the first-order YSU scheme, which had a significant impact on the shape of the wind profile. The impact of increasing the vertical resolution was negligible, whereas changing the synoptic boundary conditions from the NCEP FNL analysis to the ERA interim data changed the magnitude of the wind speed higher up in the PBL. However, none of the sensitivity test could explain the negative bias at larger heights and further research is required to find the cause of this bias.

The output of the WRF model was used to estimate large-scale parameters of the flow and investigate the impact of baroclinity at Høvsøre and in Hamburg. A method was presented to estimate the surface geostrophic and gradient wind from the simulated pressure gradients and the geostrophic wind shear from simulated horizontal gradients of the geopotential difference between two heights. The resulting estimations of the geostrophic wind showed good agreement compared to the observations of the wind speed above the PBL height. The thermal wind was variable and the geostrophic shear over the height of the PBL was often 0–5 m s^{-1} at both locations. Furthermore the thermal wind was strongly dependent on the land-sea temperature contrast, which varied seasonally. Both in Hamburg and at Høvsøre the monthly mean thermal wind vector was pointing south during winter and northeast during summer.

The effects of the thermal wind components explained a significant amount of the variation of the wind speed at larger heights and the effects were also seen on the long-term mean wind profile in both Hamburg and Høvsøre. The angle between the geostrophic wind and the thermal wind had a large influence on the angle between the surface wind and the wind above the PBL determined from the wind lidar. The geostrophic drag law is often used in wind energy assessments and was found to be sensitive to the thermal wind as well. In neutral conditions the constants A and B varied with the angle between the thermal wind and the geostrophic wind. The variations was nearly identical to the spread in experiments in the past that were assumed to be barotropic, suggesting that also in these experiments baroclinic effects were present.

8.2 Outlook and future perspectives

A large part of this thesis concerns the modelling of the wind in the coastal area, where both microscale and mesoscale modelling are required. It is therefore a suitable area to enhance the understanding of these atmospheric scales. For example, the very simple in-

terpolation of the logarithmic profiles that only uses near-surface parameters can provide a good estimation of the mean wind profile up to about 100 m. This was not only true for Høvsøre, but this model also compared well with a more sophisticated k-ε model for a coastal site in the Netherlands (M.P. van der Laan, personal communication). Above 100 m, mesoscale models capture the large-scale parameters like the geostrophic wind, the thermal wind and the advection. LES simulations can be a suitable tool to bridge the gap between the mesoscale and microscale, because parameters such as baroclinity, stability and the Brunt-Väisälä frequency can be described (Pedersen et al., 2012).

During the analysis of the data from Chapter 7 and in (Gryning et al., 2013b) it was observed that there were large underestimations of the angle between the geostrophic wind and the surface-layer wind from the WRF model output and the observations. It can be interesting to compare the cross-isobaric angle from different models with the wind lidar observations, because the cross-isobaric flow is an important parameter in NWP (Svensson and Holtslag, 2009). It appears that the lidar is a suitable instrument to measure angles in the PBL (Berg et al., 2013), because they are not disturbed by flow distortion from a meteorological mast.

Another topic that requires further study, is the structure of the internal boundary layer. At Høvsøre the growth of a well-mixed internal boundary layer in unstable conditions leads to very high wind shear near the top of the IBL. To illustrate this, Fig. 8.1 shows the development of a growing convective internal boundary layer on the 3rd of June 2010. The heat flux is rapidly increasing between 0700–1100 UTC, generating a well-mixed layer capped by an inversion. In and above the inversion, all meteorological parameters show very large variability. During the morning, the wind direction turns about 20° and the wind speed increases ~ 2 m s^{-1} over a vertical distance of 100 m.

The layer at the top of the IBL is similar to the entrainment zone in the the atmospheric PBL. Because the mast is $\approx$160 m high at Høvsøre, this gives an opportunity to measure the turbulent structure of an entrainment zone. More measurements of the IBL have been gathered during a campaign in spring 2013 at Høvsøre which involved a novel three-dimensional windscanner. This campaign synchronizes three long-range wind lidars to measure the wind speed over an area over the sea to an area over land. It will therefore provide a complete picture of the wind field. In addition, the turbulence is measured by several small masts located between the sea and the tall Høvsøre meteorological mast.

The objective of this thesis was not only to model, but also to supply future modelling studies with accurate measurements of the whole PBL. Both the wind speed measurements and the boundary layer height measurements were very accurate and should in the future be publicly available. Hopefully the presentation of cases such as those presented in Peña et al. (2013) should challenge the meteorology and wind-energy community to confront their models with this database.

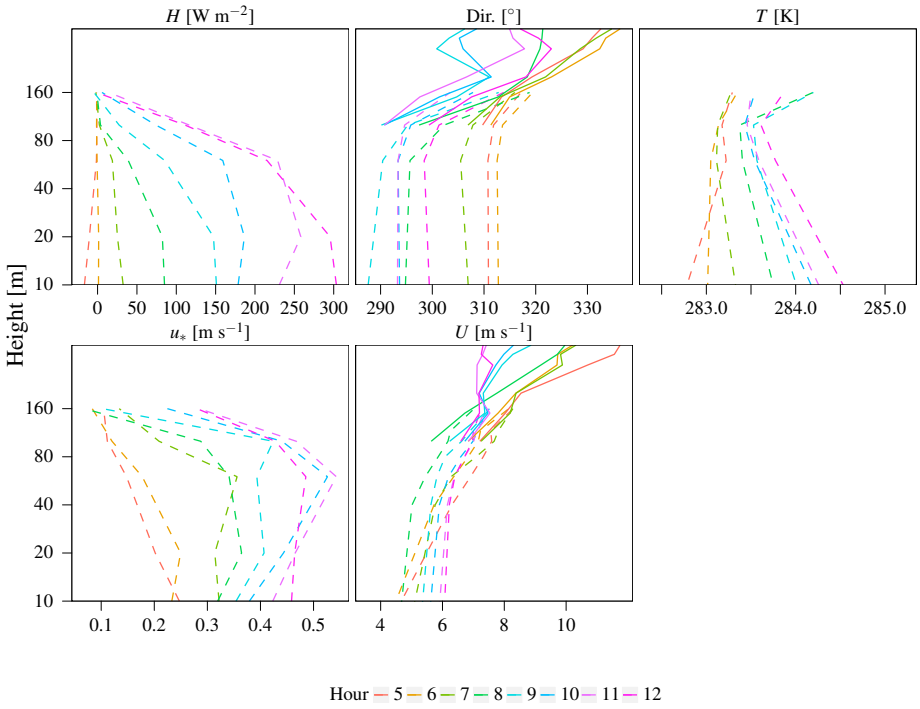

Figure 8.1: Hourly observations of the kinematic heat flux, wind direction, temperature, momentum flux and wind speed in a growing convective internal boundary layer on the 3rd of June 2010 at Høvsøre.

8.3 Implications for wind energy

The results of this thesis provide knowledge for the assessment of wind resources. First of all the results from Chapter 5 show that care should be taken when wind turbines are placed near the coastline. The internal boundary layer that develops after the roughness change can lead to situations with high vertical wind shear and large differences of turbulence intensity over a small vertical distance. These conditions cause high structural loads on wind turbines and can therefore result in fatigue failures of wind turbines (Kelley et al., 2004). For example, the wind turbines at Høvsøre have a hub height of about 80 m which is the same height where the kink in the wind profile occurs using the 3-layer interpolation scheme. Therefore it is possible that the lower part of the turbine is operating in the well-mixed region influenced by the land, while the upper part can experience conditions with very low turbulence intensity from the sea (e.g. Fig. 8.1).

The internal boundary layer is also influential when mesoscale models are employed in the coastal area. In Chapter 6 the wind profile showed large changes near the shoreline and it is important that these changes are taken into account when mesoscale models winds are used as an input for microscale models. For example, it will take several grid points to reach a new equilibrium wind profile after a coastal roughness change and therefore exact knowledge of the response of the mesoscale model wind profile is required to be able to use microscale modelling (Vincent et al., 2013).

The effect of baroclinity also resulted in wind shear and in particular to a change of wind direction with height. Estimating the long-term effects of baroclinity on the applied resistance law coefficients might improve wind resource estimations using the WAsP methodology. Future work could parametrize the effects observed in Chapter 7 so that the geostrophic drag law can be corrected for baroclinity.

DISSEMINATION

Peer-reviewed articles

Floors, R., Gryning, S.-E., Peña, A., and Batchvarova, E. (2011b). Analysis of diabatic flow modification in the internal boundary layer. *Meteorol. Zeitschrift*, 20(6):649–659

Floors, R., Vincent, C. L., Gryning, S.-E., Peña, A., and Batchvarova, E. (2013b). The Wind Profile in the Coastal Boundary Layer: Wind Lidar Measurements and Numerical Modelling. *Boundary-Layer Meteorol.*, 147(3):469–491

Floors, R., Peña, A., and Gryning, S.-E. (2013a). The effect of baroclinicity on the wind in the planetary boundary layer. *Q. J. R. Meteorol. Soc.*, (submitted)

Gryning, S.-E., Batchvarova, E., and Floors, R. (2013a). A study on the effect of nudging on long-term boundary-layer profiles of wind and Weibull distribution parameters in a rural coastal area. *J. Appl. Meteorol. Climatol.*, 52(5):1201–1207

Gryning, S.-E., Batchvarova, E., Floors, R., Peña, A., Brümmer, B., Hahmann, A. N., and Mikkelsen, T. (2013b). Long-Term Profiles of Wind and Weibull Distribution Parameters up to 600 m in a Rural Coastal and an Inland Suburban Area. *Boundary-Layer Meteorol.*, (in press)

Peña, A., Floors, R., and Gryning, S.-E. (2013). The Høvsøre Tall Wind-Profile Experiment: A Description of Wind Profile Observations in the Atmospheric Boundary Layer. *Boundary-Layer Meteorol.*, 150(1):69–89

Peer-reviewed conference proceedings

Floors, R., Batchvarova, E., Gryning, S.-E., Hahmann, A. N., Peña, A., and Mikkelsen, T. (2011a). Atmospheric boundary layer wind profile at a flat coastal site - wind speed lidar measurements and mesoscale modeling results. *Adv. Sci. Res.*, 6:155–159

Pedersen, J. G., Kelly, M., Gryning, S.-E., Floors, R., Batchvarova, E., and Peña, A. (2012). Comparison of Large Eddy Simulations of a convective boundary layer with wind LIDAR measurements. *Adv. Sci. Res.*, 8:83–86

Conference proceedings

Floors, R., Peña, A., Vincent, C. L., Gryning, S.-E., and Batchvarova, E. (2010). Wind lidar profile measurements in the coastal boundary layer : comparison with WRF modelling. In *16th Int. Symp. Adv. Boundary-Layer Remote Sens.*, pages 293–296

Gryning, S.-E., Batchvarova, E., and Floors, R. (2012). Some challenges for wind modelling for modern wind turbines: the weibull distribution. In *16th Int. Symp. Adv. Boundary-Layer Remote Sens.*, pages 194–197

Batchvarova, E., Gryning, S-E, Floors, R., Vincent, C.L., Peña, A., Mikkelsen, T. (2012) Measurements and modeling of the wind profile up to 600 meters at a flat coastal site. In *Proceedings of the NATO/SPS International Technical Meeting on Air Pollution Modelling and its Application.*

Poster and oral presentations

Floors, R., Peña, A., Gryning, S-E. (2013) The effect of baroclinicity on the wind in the planetary boundary layer. Oral presentation presented at *EMS 2013* 9–13 Sep., Reading, United Kingdom

Floors, R., Gryning, S-E., Peña, A. (2013) On the relation between the wind above the planetary boundary layer and hub-height wind: the baroclinic case. Oral presentation presented at *ICEM 2013* 25–28 Jun., Toulouse, France

Gryning, S-E., Batchvarova, E., Floors, R., Peña, A., Mikkelsen, T. (2012). Profiles of Weibull Distribution Parameters of Long Term Wind Speed Measurements. Oral presentation presented at *ICEM 2013* 25–28 Jun., Toulouse, France

Floors, R., Vincent, C.L., Gryning, S-E., Peña, A., Batchvarova, E. (2012) The wind profile in the coastal boundary layer. Poster presented at *Bridging the gap between atmospheric scales*, Wageningen, Netherlands.

Gryning, S.-E., Batchvarova, E., Floors, R., and Peña, A. (2012) Some challenges of wind modelling for modern wind turbines. Oral presentation presented at *ISARS 2012*, Boulder, USA

Floors, R., Peña, A., Vincent, C.L, Gryning, S.-E, and Batchvarova, E. (2012) Wind lidar profile measurements in the coastal boundary layer: comparison with WRF modelling. Oral presentation presented at *ISARS 2012*, Boulder, USA

Gryning, S-E., Batchvarova, E., Floors, R., Peña, A., Mikkelsen, T. (2012). The wind profile up to 600 meters at a flat coastal site; Comparison between WRF

modeling and lidar measurements. Poster presented at *EWEA 2012 - European Wind Energy Conference & Exhibition*, Copenhagen, Denmark.

Floors, R., Vincent, C.L., Gryning, S-E., Peña, A., Batchvarova, E. (2012) The wind profile in the coastal boundary layer. Oral presentation presented at *EMS 2012* 10–14 Sep., Lodz, Poland

Peña, A., Gryning, S.-E., and Floors, R. (2012) The Høvsøre tall wind profile experiment - a description of the vertical wind speed profile up to 600 m. Oral presentation presented at *EMS 2012* 10–14 Sep., Lodz, Poland

Batchvarova, E., Gryning, S-E., Hahmann, A. N., Peña, A., Floors, R., Mikkelsen, T. (2011). Comparing modeled wind profile with long-range wind lidar measurements at a flat coastal site. Poster session presented at *EWEA Annual Event 2011*, Brussels, Belgium.

Pedersen, J.G., Floors, R., Gryning, S.-E., Batchvarova, E., Kelly, M., and Peña, A. (2011) Comparison of large-eddy simulations of the convective boundary layer to wind lidar measurements. Poster presented at *EMS 2011* 12–16 Sep., Berlin, Germany

Floors, R., Batchvarova, E., Vincent, C.L, Gryning, S-E., Peña, A., Hahmann, A. N. (2011). Comparing modelled wind profile with long-range wind lidar measurements at a flat coastal site. Poster presented at *EMS 2011* 12–16 Sep., Berlin, Germany

Floors, R., Batchvarova, E., Gryning, S-E., Peña, A. (2011). "Tall" wind profiles and the effect of offshore atmospheric stability. Poster presented at *EWEA Offshore 2011*, Amsterdam (NL), 29 Nov–1 Dec

Gryning, S-E., Batchvarova, E., Floors, R., Pedersen, J.G., Peña, A., Kelly, M. (2011). Challenges in wind modelling for modern wind turbines. *International Conference Energy & Meteorology 2011*, Gold Coast, Queensland, Australia, 8–11 Nov 2011

Floors, R., Gryning, S-E., Peña, A., Batchvarova, E. (2011). Analysis of diabatic flow modification in the internal boundary layer. Oral presentation presented at *EGU 2011*, Vienna, Austria

Appendix A

DESPIKING OF THE SONIC ANEMOMETER DATA

The sonic anemometer data were despiked using the algorithm of Højstrup (1993), who assumed that the high-frequency u, v, w components of the flow and T have a gaussian distribution and that spikes (i.e. unphysical values) in the time series of these variables can be detected when the value of one of those variables is in the tails of the distribution that was expected based on the previous samples in the timeseries. So, when we have a timeseries of a variable χ_i, with $i = 1, \ldots, N$ and N the number of samples, the algorithm makes a prediction for a new value χ_f, where the subscript f denotes a forecasted value. The prediction in this timeseries is based on running statistics with a memory size of a number of n samples. The running mean is given by,

$$m_i = \frac{1}{n}(n-1)m_{i-1} + \chi_i, \tag{A.1}$$

the running variance is given by,

$$v_i = \frac{1}{n}\big((n-1)v_{i-1} + (\chi_i - m_i)^2\big), \tag{A.2}$$

and the running autocorrelation is given by,

$$c_i = \frac{1}{n}\frac{(n-1)c_{i-1}\sqrt{v_{i-1}v_{i-2}} + (\chi_i m_i)(\chi_{i-1}m_{i-1})}{v_i v_{i-1}}. \tag{A.3}$$

The memory size n was adjusted for each time step according to,

$$n = \begin{cases} 100 & \text{if } |c_i| < 0.1 \\ \frac{-230}{\log|c_{i-1}|} & \text{otherwise.} \end{cases} \tag{A.4}$$

The forecasted value is then given by:

$$\chi_f = \chi_{i-1}c_i + (1 - c_i)m_i. \tag{A.5}$$

If the next observed value χ_i in the timeseries deviates more than some standard deviations away from the predicted value χ_f, it is flagged as a spike,

$$|\chi_i - \chi_f| > L\sqrt{v_i}. \tag{A.6}$$

When the algorithm detects more than four spikes in a row for a certain variable, it is assumed that these four values are not a spike but a physical feature of the flow

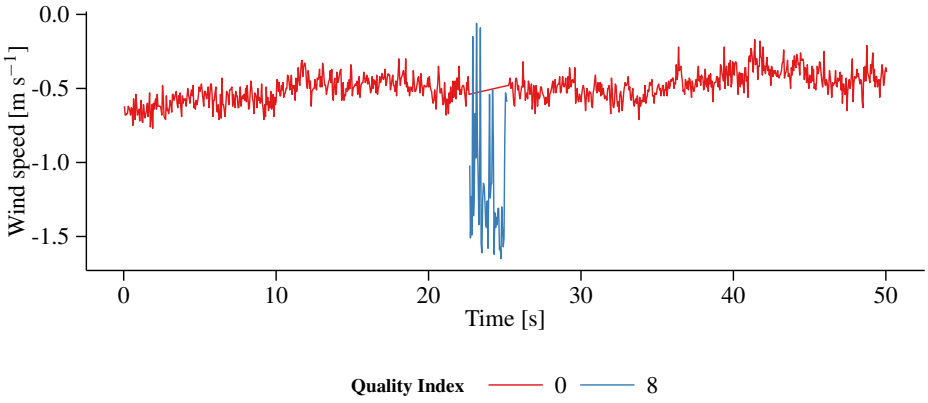

Figure A.1: Example of the *v*-component of a sonic time series at 50 m in Hamburg from the 20th of May 2011, 6:20 UTC. The blue line indicates samples that were marked as spikes.

and hence the values are set to be valid data. For the first loop through the timeseries $L = 3.5$ for the wind components and $L = 4.0$ for the temperature. After the first run the procedure is repeated but L is increased with 0.1. This procedure is repeated until all spikes are removed (Vickers and Mahrt, 1997). Visual inspection of the timeseries yielded good results in both Hovsore and Hamburg. Generally, most of the spikes were related to rainy episodes with water on the transducers and even then the percentage of spikes in a certain 10-minute interval usually did not exceed 0.5%

In figure A.1 an example of the timeseries from the *y*-component of the sonic anemometer is shown. During a few moments, the sonic reports very high and low values, which can be related to rain on the transducers. Note that there are more than 4 samples in a row that are marked as spikes, because the quality flag is a composite of the spikes in all sonic anemometer variables. All good quality data where marked with quality flag 0. In addition when χ_i was equal to χ_{i-1} for all wind components and temperature, it was assumed that the sonic anemometer was oversampling and that sample was marked with quality flag 4.

Appendix B

BUG IN YSU PBL SCHEME

There was a coding error in the implementation of the YSU scheme in versions of WRF earlier than 3.4.1 which was removed for all the simulations in Chapter 6 and 7. The YSU scheme prescribes the value of the eddy diffusivity K_m using Eq. 6.3. There was an error in the implementation of this equation which caused K_m to become high and therefore the PBL remained well-mixed with the wrong implementation. The error was introduced in the ϕ_m function used in Eq. 6.3. It was determined using the surface-layer stability parameter,

$$\frac{z}{L} = \frac{z}{L}\frac{h}{z_1}0.1, \tag{B.1}$$

where z_1 is the height of the first model level and the factor 0.1 corresponds to the surface-layer fraction of the PBL. However, h was estimated using a PBL height h_{us} based on a critical Richardson number $Ri_{cr} = 0.0$, whereas later in the code h_s was determined using $Ri_{cr} = 0.25$ (Hong et al., 2006). Therefore the following code was erroneously applied,

$$\phi_m = 1 + \left(\left(1 + 5\frac{z}{L}\frac{h_u}{z_1}0.1\right) - 1\right)\frac{z}{0.1h_s}, \tag{B.2}$$

which gives,

$$\phi_m = 1 + 5\frac{z}{L}\frac{h_u}{h_s}\frac{z}{z_1}. \tag{B.3}$$

The fraction $h_u/h_s < 1$, because turbulence is generated near the surface and $Ri \rightarrow 0.0$ at a lower height than $Ri \rightarrow 0.25$. In WRF 3.4.1 and in the corrected simulations it is correctly coded as,

$$\phi_m = 1 + 5\frac{z}{L}\frac{z}{z_1} \tag{B.4}$$

which is consistent with surface-layer similarity at the height of the first model level $z = z_1$ where MOST is assumed to be applicable and the eddy diffusivity should conform to,

$$K_m = u_* \phi_m^{-1} \kappa z, \tag{B.5}$$

where ϕ_m is determined experimentally (e.g. Businger et al., 1971) to be

$$\phi_m = 1 + 5\frac{z}{L}. \tag{B.6}$$

Appendix C

DERIVATION OF THE GEOSTROPHIC DRAG LAW

The geostrophic law was developed for the neutral, barotropic PBL with the assumption that there are two layers in the PBL, the surface layer and the outer layer. Below the height of the surface layer (h_s) where $z_0 \ll z < h_s \ll h$, the relevant dimensionless groups for describing the velocity shear of the flow are u/u_* and $\eta \equiv z/z_0$, where u is the along-wind component and the cross-wind component $v \equiv 0$ in the surface layer. In a coordinate system aligned with the surface layer wind this yields the logarithmic wind profile,

$$\frac{u}{u_*} = \frac{1}{\kappa} \ln\left(\frac{z}{z_0}\right) = F_{iu}(\eta), \tag{C.1}$$

$$\frac{v}{u_*} = 0 \tag{C.2}$$

where F_{iu} is a function of η and the subscripts i and u stand for the inner layer and the u-component, respectively. In the outer layer where $z_0 \ll z < h$ the function for the velocity are given by Eqs. 7.1 and 7.2 which can be written using the scaling height of the PBL $h \equiv u_*/f$ and $\xi \equiv z/h$ as,

$$\frac{u-u_g}{u_*} = -\frac{u_*}{f}\frac{\partial}{\partial z}\frac{\overline{v'w'}}{u_*} = -\frac{\partial}{\partial(z/h)}\frac{\overline{v'w'}}{u_*^2} = F_{ou}(\xi), \tag{C.3}$$

$$\frac{v-v_g}{u_*} = \frac{u_*}{f}\frac{\partial}{\partial z}\frac{\overline{u'w'}}{u_*} = \frac{\partial}{\partial(z/h)}\frac{\overline{u'w'}}{u_*^2} = F_{ov}(\xi), \tag{C.4}$$

where F_{ou} and F_{ov} are non-dimensional functions for both velocity components for the outer layer denoted with the subscript o. Then it assumed that there is a layer $z_0 \ll z \ll h$ where both functions F_{iu} and F_{ou} have the same normalized mean velocity gradient in the vertical where the velocity gradient in the inner layer is,

$$\frac{\partial u}{\partial z} = u_* \frac{\partial F_{iu}}{\partial \eta}\frac{\partial \eta}{\partial z} = \frac{u_*}{z_0}\frac{\partial F_{iu}}{\partial \eta}. \tag{C.5}$$

and for the velocity gradient in the outer layer,

$$\frac{\partial u}{\partial z} = u_* \frac{\partial F_{ou}}{\partial \xi}\frac{\partial \xi}{\partial z} = \frac{u_*}{h}\frac{\partial F_{ou}}{\partial \xi} \tag{C.6}$$

Multiplying Eqs. C.5 and C.6 with z/u_* gives in the layer where they are assumed both valid,

$$\frac{z}{u_*}\frac{\partial u}{\partial z} = \eta\frac{\partial F_{iu}}{\partial \eta} = \xi\frac{\partial F_{ou}}{\partial \xi}, \tag{C.7}$$

The two functions F_{iu} and F_{ou} can only be simultaneously valid when they are equal to a constant (which for convenience is chosen to be κ) and therefore they can, after integration with the respective dimensionless heights, be written as,

$$F_{iu} = \frac{1}{\kappa}\ln\eta + b \tag{C.8}$$

$$F_{ou} = \frac{1}{\kappa}\big(\ln\xi + A\big) \tag{C.9}$$

and in the surface layer the integration constant $b = 0$. Now we have descriptions for the functions F_{iu} and F_{iu} and then subtracting C.3 from C.1 and defining a friction Rossby number $Ro \equiv u_*/fz_0$ yields,

$$\frac{u_g}{u_*} = F_{iu} - F_{ou} = \frac{1}{\kappa}\big(\ln(Ro) - A\big). \tag{C.10}$$

Similarly we can obtain an expression for v by subtracting C.4 from C.2,

$$\frac{v_g}{u_*} = -F_{ov} = -\frac{B}{\kappa}. \tag{C.11}$$

Using the relation $G = \sqrt{u_g^2 + v_g^2}$ the geostrophic wind speed is given by,

$$G = \frac{u_*}{\kappa}\sqrt{\Big(\ln(Ro) - A\Big)^2 - B^2}, \tag{C.12}$$

and the cross-isobaric angle is given by,

$$\alpha = \arctan\frac{-B}{\ln(Ro) - A}. \tag{C.13}$$

The interesting result of these relations is that the cross-isobaric angle and the geostrophic drag u_*/G are functions of Ro only at mid-latitudes when the flow is in geostrophic balance. The constants A and B can easily be obtained from experimental data when Eqs. C.10 and C.11 are rewritten to their form in Eqs. 7.7 and 7.8. Near the equator the assumption of geostrophic balance is not valid because there $f \to 0$.

Bibliography

Arya, S. P. S. and Wyngaard, J. C. (1975). Effect of Baroclinicity on Wind Profiles and the Geostrophic Drag Law for the Convective Planetary Boundary Layer. *J. Atmos. Sci.*, 32(4):767–778.

Baas, P., Bosveld, F., Lenderink, G., van Meijgaard, E., and Holtslag, A. A. M. (2010). How to design single-column model experiments for comparison with observed nocturnal low-level jets. *Q. J. R. Meteorol. Soc.*, 138(648):671–684.

Baas, P., Bosveld, F. C., Klein Baltink, H., and Holtslag, A. A. M. (2009). A Climatology of Nocturnal Low-Level Jets at Cabauw. *J. Appl. Meteorol. Clim.*, 48(8):1627–1642.

Batchvarova, E., Gryning, S.-E., and Hasager, C. (2001). Regional fluxes of momentum and sensible heat over a sub-arctic landscape during late winter. *Boundary-Layer Meteorol.*, 99(3):489–507.

Beljaars, A. C. M. and Holtslag, A. A. M. (1991). Flux Parameterization over Land Surfaces for Atmospheric Models. *J. Appl. Meteorol.*, 30(3):327–341.

Beljaars, A. C. M., Holtslag, A. A. M., and Turkenburg, W. C. (1990). Diabatic wind speed profiles in coastal regions: Comparison of an internal boundary layer (IBL) model with observations. *Boundary-Layer Meteorol.*, 51(1-2):49–75.

Belušić, D. and Güttler, I. (2010). Can mesoscale models reproduce meandering motions? *Q. J. R. Meteorol. Soc.*, 136(648):553–565.

Berg, J., Mann, J., and Nielsen, M. (2013). Introduction to micro meteorology for wind energy. Technical Report February, DTU Wind Energy, Roskilde, Denmark.

Bergström, H., Johansson, P.-E., and Smedman, A.-S. (1988). A study of wind speed modification and internal boundary-layer heights in a coastal region. *Boundary-Layer Meteorol.*, 42(4):313–335.

Blackadar, A. K. (1957). Boundary layer wind maxima and their significance for the growth of nocturnal inversions. *Bull. Amer. Meteor. Soc*, 38(5):283–290.

Blackadar, A. K. and Tennekes, H. (1968). Asymptotic Similarity in Neutral Barotropic Planetary Boundary Layers. *J. Atmos. Sci.*, 25(6):1015–1020.

Bradley, E. F. (1968). A micrometeorological study of velocity profiles and surface drag in the region modified by a change in surface roughness. *Q. J. R. Meteorol. Soc.*, 94(401):361–379.

Brown, A. (1996). Large-eddy simulation and parametrization of the baroclinic boundary-layer. *Q. J. R. Meteorol. Soc.*, 122(536):1779–1798.

Businger, J. A., Wyngaard, J. C., Izumi, Y., and Bradley, E. F. (1971). Flux-Profile Relationships in the Atmospheric Surface Layer. *J. Atmos. Sci.*, 28(2):181–189.

Cariou, J.-P. and Boquet, M. (2013). Leosphere Pulsed Lidar Principles. Technical report, Leosphere, Orsay, France.

Charnock, H. (1955). Wind stress on a water surface. *Q. J. R. Meteorol. Soc.*, 81(350):639–640.

Chen, F. and Dudhia, J. (2001). Coupling an Advanced Land Surface–Hydrology Model with the Penn State–NCAR MM5 Modeling System. Part I: Model Implementation and Sensitivity. *Mon. Weather. Rev.*, 129(4):569–585.

Cheng, Y., Brutsaert, W., and Chenge, Y. (2005). Flux-profile Relationships for Wind Speed and Temperature in the Stable Atmospheric Boundary Layer. *Boundary-Layer Meteorol.*, 114(3):519–538.

Clarke, R. H. and Hess, G. D. (1974). Geostrophic departure and the functions A and B of Rossby-number similarity theory. *Boundary-Layer Meteorol.*, 7(3):267–287.

Coelingh, J. (1998). Analysis of wind speed observations on the North Sea coast. *J. Wind Eng. Ind. Aero.*, 73(2):125–144.

Cuxart, J., Holtslag, A. A. M., Beare, R. J., Bazile, E., Beljaars, A., Cheng, A., Conangla, L., Ek, M., Freedman, F., Hamdi, R., Kerstein, A., Kitagawa, H., Lenderink, G., Lewellen, D., Mailhot, J., Mauritsen, T., Perov, V., Schayes, G., Steeneveld, G.-J., Svensson, G., Taylor, P., Weng, W., Wunsch, S., and Xu, K.-M. (2005). Single-Column Model Intercomparison for a Stably Stratified Atmospheric Boundary Layer. *Boundary-Layer Meteorol.*, 118(2):273–303.

Dee, D. P., Uppala, S. M., Simmons, A. J., Berrisford, P., Poli, P., Kobayashi, S., Andrae, U., Balmaseda, M. a., Balsamo, G., Bauer, P., Bechtold, P., Beljaars, a. C. M., van de Berg, L., Bidlot, J., Bormann, N., Delsol, C., Dragani, R., Fuentes, M., Geer, a. J., Haimberger, L., Healy, S. B., Hersbach, H., Hólm, E. V., Isaksen, L., Kå llberg, P., Köhler, M., Matricardi, M., McNally, a. P., Monge-Sanz, B. M., Morcrette, J.-J., Park, B.-K., Peubey, C., de Rosnay, P., Tavolato, C., Thépaut, J.-N., and Vitart, F. (2011). The ERA-Interim reanalysis: configuration and performance of the data assimilation system. *Q. J. R. Meteorol. Soc.*, 137(656):553–597.

Derbyshire, S. H. (1999). Boundary-layer decoupling over cold surfaces as a physical boundary-instability. *Boundary-Layer Meteorol.*, 90(2):297–325.

Dudhia, J. (1989). Numerical Study of Convection Observed during the Winter Monsoon Experiment Using a Mesoscale Two-Dimensional Model. *J. Atmos. Sci.*, 46(20):3077–3107.

Dyer, A. J. (1974). A review of flux-profile relationships. *Boundary-Layer Meteorol.*, 7(3):363–372.

Fairall, C. W., Bradley, E. F., Hare, J. E., Grachev, A. A., and Edson, J. B. (2003). Bulk Parameterization of Air–Sea Fluxes: Updates and Verification for the COARE Algorithm. *J. Clim.*, 16(4):571–591.

Floors, R., Batchvarova, E., Gryning, S.-E., Hahmann, A. N., Peña, A., and Mikkelsen, T. (2011a). Atmospheric boundary layer wind profile at a flat coastal site - wind speed lidar measurements and mesoscale modeling results. *Adv. Sci. Res.*, 6:155–159.

Floors, R., Gryning, S.-E., Peña, A., and Batchvarova, E. (2011b). Analysis of diabatic flow modification in the internal boundary layer. *Meteorol. Zeitschrift*, 20(6):649–659.

Floors, R., Peña, A., and Gryning, S.-E. (2013a). The effect of baroclinicity on the wind in the planetary boundary layer. *Q. J. R. Meteorol. Soc.*, (submitted).

Floors, R., Peña, A., Vincent, C. L., Gryning, S.-E., and Batchvarova, E. (2010). Wind lidar profile measurements in the coastal boundary layer : comparison with WRF modelling. In *16th Int. Symp. Adv. Boundary-Layer Remote Sens.*, pages 293–296.

Floors, R., Vincent, C. L., Gryning, S.-E., Peña, A., and Batchvarova, E. (2013b). The Wind Profile in the Coastal Boundary Layer: Wind Lidar Measurements and Numerical Modelling. *Boundary-Layer Meteorol.*, 147(3):469–491.

Garratt, J. R. (1985). The inland boundary layer at low latitudes. *Boundary-Layer Meteorol.*, 32(4):307–327.

Garratt, J. R. (1990). The internal boundary layer - A review. *Boundary-Layer Meteorol.*, 50(1-4):171–203.

Gibbs, J. A., Fedorovich, E., and van Eijk, A. M. J. (2011). Evaluating Weather Research and Forecasting (WRF) Model Predictions of Turbulent Flow Parameters in a Dry Convective Boundary Layer. *J. Appl. Meteorol.*, 50(12):2429–2444.

Gryning, S.-E. and Batchvarova, E. (1990). Analytical model for the growth of the coastal internal boundary layer during onshore flow. *Q. J. R. Meteorol. Soc.*, 116(491):187–203.

Gryning, S.-E. and Batchvarova, E. (1996). A model for the height of the internal boundary layer over an area with an irregular coastline. *Boundary-Layer Meteorol.*, 78(3-4):405–413.

Gryning, S.-E., Batchvarova, E., Brümmer, B., Jørgensen, H., and Larsen, S. (2007a). On the extension of the wind profile over homogeneous terrain beyond the surface boundary layer. *Boundary-Layer Meteorol.*, 124(2):251–268.

Gryning, S.-E., Batchvarova, E., and Floors, R. (2012). Some challenges for wind modelling for modern wind turbines: the weibull distribution. In *16th Int. Symp. Adv. Boundary-Layer Remote Sens.*, pages 194–197.

Gryning, S.-E., Batchvarova, E., and Floors, R. (2013a). A study on the effect of nudging on long-term boundary-layer profiles of wind and Weibull distribution parameters in a rural coastal area. *J. Appl. Meteorol. Climatol.*, 52(5):1201–1207.

Gryning, S.-E., Batchvarova, E., Floors, R., Peña, A., Brümmer, B., Hahmann, A. N., and Mikkelsen, T. (2013b). Long-Term Profiles of Wind and Weibull Distribution Parameters up to 600 m in a Rural Coastal and an Inland Suburban Area. *Boundary-Layer Meteorol.*, (in press).

Gryning, S.-E., Jørgensen, H., Larsen, S., and Batchvarova, E. (2007b). The wind profile up to 300 meters over flat terrain. In *J. Phys. Conf. Ser.*, number 75 012066, pages 1–9.

Hannesdóttir, A. (2013). *Boundary-layer height detection with a ceilometer at a coastal site in western Denmark*. Master thesis m-0039, DTU Wind Energy, Roskilde, Denmark.

Hess, G. D. and Garratt, J. R. (2002a). Evaluating Models of The Neutral, Barotropic Planetary Boundary Layer using Integral Measures: Part I. Overview. *Boundary-Layer Meteorol.*, 104(3):333–358.

Hess, G. D. and Garratt, J. R. (2002b). Evaluating Models Of The Neutral, Barotropic Planetary Boundary Layer Using Integral Measures: Part II. Modelling Observed Conditions. *Boundary-Layer Meteorol.*, 104(3):333–358.

Högström, U. (1988). Non-dimensional wind and temperature profiles in the atmospheric surface layer: A re-evaluation. *Boundary-Layer Meteorol.*, 42(1-2):55–78.

Højstrup, J. (1993). A statistical data screening procedure. *Meas. Sci. Technol.*, 4(2):153–157.

Holton, J. R. and Hakim, G. J. (2004). *An introduction to dynamic meteorology*. Elsevier Academic press, 4th edition.

Holtslag, A. A. M. and De Bruin, H. A. R. (1988). Applied Modeling of the Nighttime Surface Energy Balance over Land. *J. Appl. Meteorol.*, 27(6):689–704.

Hong, S.-Y. (2010). A new stable boundary-layer mixing scheme and its impact on the simulated East Asian summer monsoon. *Q. J. R. Meteorol. Soc.*, 136(651):1481–1496.

Hong, S.-Y., Noh, Y., and Dudhia, J. (2006). A New Vertical Diffusion Package with an Explicit Treatment of Entrainment Processes. *Mon. Weather. Rev.*, 134(9):2318–2341.

Hoxit, L. R. (1974). Planetary Boundary Layer Winds in Baroclinic Conditions. *J. Atmos. Sci.*, 31(4):1003–1020.

Hu, X.-M., Nielsen-Gammon, J. W., and Zhang, F. (2010). Evaluation of Three Planetary Boundary Layer Schemes in the WRF Model. *J. Appl. Meteorol. Clim.*, 49(9):1831–1844.

Jiménez, P. A., Dudhia, J., González-Rouco, J. F., Navarro, J., Montávez, J. P., and García-Bustamante, E. (2012). A Revised Scheme for the WRF Surface Layer Formulation. *Mon. Weather. Rev.*, 140(3):898–918.

Joffre, S. M. (1982). Assessment of the separate effects of baroclinicity and thermal stability in the atmospheric boundary layer over the sea. *Tellus*, 34(6):567–578.

Józsa, J., Milici, B., and Napoli, E. (2006). Numerical simulation of internal boundary-layer development and comparison with atmospheric data. *Boundary-Layer Meteorol.*, 123(1):159–175.

Källstrand, B. and Smedman, A. (1997). A case study of the near-neutral coastal internal boundary-layer growth: Aircraft measurements compared with different model estimates. *Boundary-Layer Meteorol.*, 85(1):1–33.

Kelley, N., Shirazi, M., Jager, D., Wilde, S., Patton, E. G., and Sullivan, P. (2004). Lamar Low-Level Jet Project Interim Report. Technical Report January, NREL/TP-500-34593, National Renewable Energy Laboratory, Golden, Colorado, United States.

Kristensen, L. and Jensen, G. (1999). Geostrophic Winds in Denmark: a preliminary study. Technical Report November, Risø National Laboratory, Roskilde, Denmark.

Lange, B., Larsen, S., Højstrup, J., and Barthelmie, R. (2004). Importance of thermal effects and sea surface roughness for offshore wind resource assessment. *J. Wind Eng. Ind. Aero.*, 92(11):959–988.

Larsén, X. G. and Mann, J. (2009). Extreme winds from the NCEP/NCAR reanalysis data. *Wind Energy*, 12(6):556–573.

Lenschow, D. H., Wyngaard, J. C., and Pennell, W. T. (1980). Mean-Field and Second-Moment Budgets in a Baroclinic, Convective Boundary Layer. *J. Atmos. Sci.*, 37(6):1313–1326.

Mahrt, L. (1996). The bulk aerodynamic formulation over heterogeneous surfaces. *Boundary-Layer Meteorol.*, 78(1-2):87–119.

Mahrt, L. (1999). Stratified atmospheric boundary layers. *Boundary-Layer Meteorol.*, 90(3):375–396.

McCabe, A. and Brown, A. R. (2006). The role of surface heterogeneity in modelling the stable boundary layer. *Boundary-Layer Meteorol.*, 122(3):517–534.

Melas, D. and Kambezidis, H. D. (1992). The depth of the internal boundary layer over an urban area under sea-breeze conditions. *Boundary-Layer Meteorol.*, 61(3):247–264.

Mellor, G. L., Yamada, T., and Alarnos, L. (1982). Development of a turbulence closure model for geophysical fluid problems. *Rev. Geophys.*, 20(4):851.

Miyake, M. (1965). *Transformation of the atmospheric boundary layer over inhomogeneous surfaces*. Unpublished msc. thesis, Univ. of Washington.

Mlawer, E. J., Taubman, S. J., Brown, P. D., Iacono, M. J., and Clough, S. A. (1997). Radiative transfer for inhomogeneous atmospheres: RRTM, a validated correlated-k model for the longwave. *J. Geophys. Res.*, 102(D14):16663–16682.

Münkel, C., Schäfer, K., and Emeis, S. (2011). Adding confidence levels and error bars to mixing layer heights detected by ceilometer. In Kassianov, E. I., Comeron, A., Picard, R. H., and Schäfer, K., editors, *Rem. Sens. Cl. Atmos. XVI*, volume 8177, pages 1–9.

Nakanishi, M. and Niino, H. (2009). Development of an Improved Turbulence Closure Model for the Atmospheric Boundary Layer. *J. Meteorol. Soc. Japan*, 87(5):895–912.

Nieuwstadt, F. T. M. (1984). The Turbulent Structure of the Stable, Nocturnal Boundary Layer. *J. Atmos. Sci.*, 41(14):2202–2216.

Obukhov, A. M. (1971). Turbulence in an atmosphere with a non-uniform temperature. *Boundary-Layer Meteorol.*, 2(1):7–29.

Panofsky, H. (1973). Tower micrometeorology. In Haugen, D. A., editor, *Work. Micrometeorology*, pages 151–176. American Meteorological Society, Boston.

Paulson, C. A. (1970). The Mathematical Representation of Wind Speed and Temperature Profiles in the Unstable Atmospheric Surface Layer. *J. Appl. Meteorol.*, 9(6):857–861.

Peña, A. (2009). *Sensing the wind profile*. Phd thesis, Technical University of Denmark, Roskilde, Denmark.

Peña, A., Floors, R., and Gryning, S.-E. (2013). The Høvsøre Tall Wind-Profile Experiment: A Description of Wind Profile Observations in the Atmospheric Boundary Layer. *Boundary-Layer Meteorol.*, 150(1):69–89.

Peña, A., Gryning, S.-E., and Hasager, C. B. (2008). Measurements and Modelling of the Wind Speed Profile in the Marine Atmospheric Boundary Layer. *Boundary-Layer Meteorol.*, 129(3):479–495.

Peña, A., Gryning, S.-E., and Hasager, C. B. (2009a). Comparing mixing-length models of the diabatic wind profile over homogeneous terrain. *Theor. Appl. Clim.*, 100(3-4):325–335.

Peña, A. and Hahmann, A. (2011). Atmospheric stability and turbulence fluxes at Horns Rev—an intercomparison of sonic, bulk and WRF model data. *Wind Energy*.

Peña, A., Hasager, C. B., Gryning, S.-E., Courtney, M., Antoniou, I., and Mikkelsen, T. (2009b). Offshore wind profiling using light detection and ranging measurements. *Wind Energy*, 12(2):105–124.

Pedersen, J. G., Kelly, M., Gryning, S.-E., Floors, R., Batchvarova, E., and Peña, A. (2012). Comparison of Large Eddy Simulations of a convective boundary layer with wind LIDAR measurements. *Adv. Sci. Res.*, 8:83–86.

Peterson, E. W. (1969). Modification of mean flow and turbulent energy by a change in surface roughness under conditions of neutral stability. *Q. J. R. Meteorol. Soc.*, 95(405):561–575.

Prandtl, L. (1925). Report on investigation of developed turbulence. *Zeitschrift für Angew. Math. und Mech.*, 5(2):136–139.

Rao, K. S., Wyngaard, J. C., and Coté, O. R. (1974). The Structure of the Two-Dimensional Internal Boundary Layer over a Sudden Change of Surface Roughness. *J. Atmos. Sci.*, 31(3):738–746.

Sathe, A., Gryning, S.-E., and Peña, A. (2011). Comparison of the atmospheric stability and wind profiles at two wind farm sites over a long marine fetch in the North Sea. *Wind Energy*, 14(6):767–780.

Savelyev, S. and Taylor, P. A. (2001). Notes on an internal boundary layer height formula. *Boundary-Layer Meteorol.*, 101(3):293–301.

Savelyev, S. A. and Taylor, P. A. (2005). Internal Boundary Layers: I. Height Formulae for Neutral and Diabatic Flows. *Boundary-Layer Meteorol.*, 115(1):1–25.

Schotanus, P., Nieuwstadt, F., and Bruin, H. (1983). Temperature measurement with a sonic anemometer and its application to heat and moisture fluxes. *Boundary-Layer Meteorol.*, 26(1):81–93.

Seibert, P., Beyrich, F., Gryning, S.-E., Joffre, S., Rasmussen, A., and Tercier, P. (2000). Review and intercomparison of operational methods for the determination of the mixing height. *Atmos. Env.*, 34(7):1001–1027.

Sempreviva, A. M., Larsen, S. E., Mortensen, N. G., and Troen, I. (1990). Response of neutral boundary layers to changes of roughness. *Boundary-Layer Meteorol.*, 50(1-4):205–225.

Shary, P. A. (1995). Land surface in gravity points classification by a complete system of curvatures. *Mat. Geol.*, 27(3):373–390.

Shin, H. H. and Hong, S.-Y. (2011). Intercomparison of Planetary Boundary-Layer Parametrizations in the WRF Model for a Single Day from CASES-99. *Boundary-Layer Meteorol.*, 139(2):261–281.

Shir, C. C. (1972). A Numerical Computation of Air Flow over a Sudden Change of Surface Roughness. *J. Atmos. Sci.*, 29(2):304–310.

Sjöblom, A. and Smedman, A.-S. (2003). Vertical structure in the marine atmospheric boundary layer and its implication for the inertial dissipation method. *Boundary-Layer Meteorol.*, 109(1):1–25.

Skamarock, W. C., Klemp, J. B., Dudhia, J., Gill, D. O., Barker, D. M., Duda, M. G., Huang, X.-y. Y., Wang, W., and Powers, J. G. (2005). A description of the Advanced Research WRF version 3. Technical Report June, NCAR/TN-475+ STR.

Sorbjan, Z. (2004). Large-Eddy Simulations of the Baroclinic Mixed Layer. *Boundary-Layer Meteorol.*, 112(1):57–80.

Steeneveld, G. J., Tolk, L. F., Moene, A. F., Hartogensis, O. K., Peters, W., and Holtslag, A. A. M. (2011). Confronting the WRF and RAMS mesoscale models with innovative observations in the Netherlands: Evaluating the boundary layer heat budget. *J. Geophys. Res.*, 116(D23):D23114.

Steyn, D. G., Baldi, M., and Hoff, R. M. (1999). The Detection of Mixed Layer Depth and Entrainment Zone Thickness from Lidar Backscatter Profiles. *J. Atmos. Ocean. Tech.*, 16(7):953–959.

Storm, B., Dudhia, J., Basu, S., Swift, A., and Giammanco, I. (2009). Evaluation of the Weather Research and Forecasting model on forecasting low-level jets: implications for wind energy. *Wind Energy*, 12(1):81–90.

Sušelj, K. and Sood, A. (2010). Improving the Mellor–Yamada–Janjić Parameterization for wind conditions in the marine planetary boundary layer. *Boundary-Layer Meteorol.*, 136(2):301–324.

Svensson, G. and Holtslag, A. A. M. (2009). Analysis of Model Results for the Turning of the Wind and Related Momentum Fluxes in the Stable Boundary Layer. *Boundary-Layer Meteorol.*, 132(2):261–277.

Tammelin, B., Vihma, T., Atlaskin, E., Badger, J., Fortelius, C., Gregow, H., Horttanainen, M., Kilpinen, J., Latikka, J., Ljungberg, K., Mortensen, N. G., Ruosteenoja, K., Salonen, K., Suomi, I., Hyvönen, R., Niemelä, S., and Venäläinen, A. (2013). Production of the Finnish Wind Atlas. *Wind Energy*, 16(1):19–35.

Thompson, G., Rasmussen, R. M., and Manning, K. (2004). Explicit Forecasts of Winter Precipitation Using an Improved Bulk Microphysics Scheme. Part I: Description and Sensitivity Analysis. *Mon. Weather. Rev.*, 132(2):519–542.

Tijm, A. B. C., Van Delden, A. J., and Holtslag, A. A. M. (1999). The inland penetration of sea breezes. *Contr. Atmos. Phys.*, 72:317–328.

Troen, I. and Petersen, E. L. (1989). *European Wind Atlas*. Risø National Laboratory, Roskilde, Denmark.

Van Dijk, A., Moene, A. F., and De Bruin, H. A. R. (2004). The principles of surface flux physics: theory, practice and description of the ECPACK library. Technical report, Meteorology and Air Quality Group, Wageningen University, Wageningen, the Netherlands, 99 pp.

Vickers, D. and Mahrt, L. (1997). Quality Control and Flux Sampling Problems for Tower and Aircraft Data. *J. Atmos. Ocean. Tech.*, 14(3):512–526.

Vickers, D. and Mahrt, L. (1999). Observations of non-dimensional wind shear in the coastal zone. *Q. J. R. Meteorol. Soc.*, 125(559):2685–2702.

Vincent, C. L., Badger, J., Hahmann, A. N., and Kelly, M. C. (2013). The response of mesoscale models to changes in surface roughness. *Geophys. Res. Abs.*, 15(10).

Wieringa, J. (1986). Roughness-dependent geographical interpolation of surface wind speed averages. *Q. J. R. Meteorol. Soc.*, 112(473):867–889.

Wilczak, J. M., Oncley, S. P., and Stage, S. A. (2001). Sonic anemometer tilt correction algorithms. *Boundary-Layer Meteorol.*, 99(1):127–150.

Wyngaard, J. C. (2004). Toward Numerical Modeling in the "Terra Incognita". *J. Atmos. Sci.*, 61(14):1816–1826.

Xie, B., Fung, J. C.-H., Chan, A., and Lau, A. K.-H. (2012). Evaluation of nonlocal and local planetary boundary layer schemes in the WRF model. *J. Geophys. Res.*, 117(May):1–26.

Zhang, D.-L. and Zheng, W.-Z. (2004). Diurnal Cycles of Surface Winds and Temperatures as Simulated by Five Boundary Layer Parameterizations. *J. Appl. Meteorol.*, 43(1):157–169.

Zilitinkevich, S. S. (1975). Resistance Laws and Prediction Equations for the Depth of the Planetary Boundary Layer. *J. Atmos. Sci.*, 32(4):741–752.

Zilitinkevich, S. S. and Esau, I. N. (2002). On integral measures of the neutral barotropic planetary boundary layer. *Boundary-Layer Meteorol.*, 104(3):371–379.

Zilitinkevich, S. S. and Esau, I. N. (2005). Resistance and heat-transfer laws for stable and neutral planetary boundary layers: Old theory advanced and re-evaluated. *Q. J. R. Meteorol. Soc.*, 131(609):1863–1892.

Zilitinkevich, S. S. and Esau, I. N. (2007). Similarity theory and calculation of turbulent fluxes at the surface for the stably stratified atmospheric boundary layer. *Boundary-Layer Meteorol.*, 125(2):193–205.

This dissertation is submitted in partial fulfilment of the requirements for the degree of Doctor of Philosophy in Engineering at the Technical University of Denmark. The work was done at the Meteorology Section of the Department of Wind Energy and has been part of the Danish Research Council for Strategic Research Project 2104-08-0025 named "Tall wind".

Principal supervisor: Dr. Scient. Sven-Erik Gryning
Co supervisor: Dr. Alfredo Peña
Examiners: Professor Søren Larsen, DTU Wind Energy
Dr. James Wilczak, Earth Systems Research Laboratory, NOAA, Boulder, USA
Dr. Line Gulstad, Vestas Wind Systems, Denmark

DTU Wind Energy
Technical University of Denmark

Risø Campus, 118
Frederiksborgvej 399
DK-4000 Roskilde
http://www.vindenergi.dtu.dk/

ISBN 978-87-92896-76-6